Fermilab

FERMILAB-THESIS-2000-09

Precision measurements of the Λ_c^+ and D^0 lifetimes

by Alexander Yevgenievich Kushnirenko

A Dissertation

Submitted to the Department of Physics,
Mellon College of Science,
in partial fulfillment of the requirements for the degree of

Doctor of Philosophy

Carnegie Mellon University
December, 2000

Abstract

We report new precision measurements of the lifetimes of the Λ_c^+ and D^0 from SELEX, the charm hadro-production experiment at Fermilab. Based upon 1630 Λ_c^+ and 10210 D^0 decays we observe lifetimes of $\tau[\Lambda_c^+] = 198.1 \pm 7.0 \pm 5.7$ fs and $\tau[D^0] = 407.9 \pm 6.0 \pm 4.7$ fs.

To my Dad and Mom
who introduced me to the wonderful
world of Physics

Acknowledgements

I am grateful to my advisor Prof. James Russ for his guidance and support during my research in SELEX experiment. As a teacher he has a fine balance between giving me a lot o freedom to wander around in my research and correcting me when I was marching in the wrong direction. I'm thankful for his discussions on high-energy experiments, charm physics and my analysis. All these years he was always 100% behind me, supporting all my projects, even when they had very little chance for success. I always felt, that things I was doing were greatly appreciated and important, which certainly stimulated me a lot. I'm also very thankful that he would always help me and my family in many different situations.

My gratitude goes to Dr. Peter Cooper, who spent endless hours with me. With equal enthusiasm he would discuss with me latest physics topics, help me to solve subtle problem in my analysis, or just go with me through the lines of code chasing the bug. Loaded with ideas or lost in the jungles of analysis I could always walk into his office and find his attention and will to help. Always ready to share and discuss different ideas he taught me a lot of fine details about an art of experimental physics.

I had wonderful time working with offline group: Mark Mattson, Mike Procario, Jianming You, Slava Rud, Soon Jun, Viktor Kurshetsov, Nikolay Kuropatkin. It was an invaluable experience when we worked together on creating offline program, nurturing and baby-sitting it in its youth, watching it making its first steps, helping it grow and finally trying to control this monster from eating us alive and trying to put it to do some useful work.

I'm thankful to my SELEX colleagues for creating good environment for students in the experiment. It was really stimulating that senior physicist made sure that younger physicist would get enough exposure. Special thanks to Joe Lach for his discussions about hyperon physics, to Linda Stutte for explaining me details of RICH detector, to Jurgen Engelfried for sharing his ideas how to make DAQ, trigger and other things work right, to Maurizio Iori for his help in lifetime analysis and to Nikolay Terentiev for explaining details of PWC detectors.

I'm grateful to Dr. Leonid Landsberg, who stopped me from getting too specialized in detector hardware, convinced me to go to the graduate school and helped me to organize it.

I'm indeptful to my wife Galia and my kids for their infinite patience and

all the sacrifices they made to let me get the degree. I would like to thank my parents, brothers and relatives for their encouragement and support.

Working in SELEX experiment was wonderful experience. I was lucky to join the experiment year before it started to take data. which gave me a unique opportunity to go through most of the stages of experiment's life: preparation for the run, taking the data, calibration and alignment, processing the data and finally getting the physics results. I met new colleagues, got invaluable experience and learned a lot of new things. One of the most important outcomes of my graduate school experience is the great desire to continue high energy physics experimental research.

To all my SELEX colleagues - Thank you!

Contents

List of Figures

List of Tables

Chapter 1

Study of Charm Lifetimes

A particle's lifetime is one the fundamental quantities that describe its internal dynamics. Based on the lifetime, one can conclude if the particle decay is driven by the strong, weak, or electro-magnetic forces. Charm and beauty particle decays are driven by the weak force, but the strong interactions of the decay products significantly modify the decay dynamics. The correct quantitative description of the interplay of the weak and strong forces in heavy quark decays is crucial to test the Standard Model, to measure its parameters and to search for the new physics beyond Standard Model. A very common problem in these studies is the complexity of QCD effects that must be resolved before important parameters of Standard Model can be measured or signals for new physics can be claimed.

The lifetimes of charm and beauty particles are best described by the Heavy Quark Expansion (HQE) theory. It is very important to test HQE, because it is used not only to calculate lifetimes, but also to relate branching ratios to CKM parameters, to measure mixing parameters, to extract CP violating parameters from different observables, to calculate different decay rates and to compute many other important processes which involve heavy quarks. Recent precision lifetime measurements of the whole spectra of charm particles provide an important input for the tests of HQE. Improved precision of the lifetime measurements highlighted problems in HQE calculations and also motivated physicists to understand the heavy quark dynamics more deeply. Also the knowledge of lifetimes is used in experiments to separate signal from background and to translate branching ratios into absolute decay rates for different decay channels.

1.1 Early days of spectator model

One of the first models to describe charm particle decays was based on the assumption that the decay rate of charm particles is driven by the decay of the heavy c-quark (Figure 1.1). The light quarks act only as spectators and do not affect the decay rate at all [1]. In this picture all charm hadrons - mesons and baryons - would have essentially the same lifetime, up to phase space corrections.

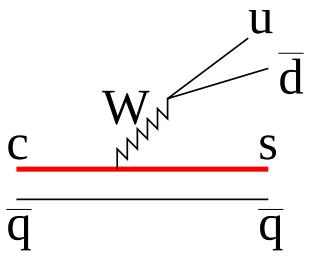

Figure 1.1: Spectator decay diagram

This idea might come to mind upon observing how close the semi-leptonic branching ratio B_{SL} of $D^+(c\overline{d})$ is close to a naive estimate of 20%:

$$\begin{aligned} B_{SL} = \frac{\Gamma(C \to e^+ \nu_e X)}{\Gamma(C \to all)} &\sim \frac{1_{e\nu}}{1_{e\nu} + 1_{\mu\nu} + 3_{u\overline{d}}} = 20\% \\ B_{SL}(D^+ \to e^+ X) &= 17.2 \pm 1.9\% \end{aligned}$$

The comparison of D^+ semileptonic branching ratio to the semileptonic branching ratio of τ-lepton, which indeed is driven only by decay of a heavy fermion, is really striking:

$$B_{SL}(\tau^- \to e^- \overline{\nu}_e \nu_\tau) = 17.83 \pm 0.06\%.$$

The deviation from the ideal 20% for τ-lepton is explained by QCD-corrections [2].

Perhaps this early data on semileptonic branching ratios encouraged N. Cabibbo and L. Miani to conclude in 1977: "...Since the uncharmed antiquark acts as a spectator, one is led to predict equal lifetimes and equal semi-leptonic branching ratios for the three mesons..." [3]

As we know now, both statements turned out to be wrong: the $D^0(c\overline{u})$, $D_s^+(c\overline{s})$ and $D^+(c\overline{d})$ have different lifetimes and different semileptonic branching ratios, for example [4]:

$$\begin{aligned} \frac{\tau(D^+)}{\tau(D^0)} &= 2.547 \pm 0.036 \\ B_{SL}(D^0 \to e^+ X) &= 6.75 \pm 0.29\% \\ B_{SL}(D^+ \to e^+ X) &= 17.2 \pm 1.9\% \ . \end{aligned}$$

Further experimental data showed that the charm lifetimes differ more than a factor 10 $\tau(D^+(c\overline{d}))/\tau(\Omega_c^0(css)) \sim 20$ [4]. This clearly says that the light quarks are not just spectators but can significantly influence the decay dynamics.

1.1.1 Problem is in non-leptonic decays

The observed difference in D^+/D^0 lifetimes made the picture quite complicated, but still there was the good news that the absolute semileptonic decay rates were the same [4]:

$$\begin{aligned} \Gamma_{SL}(D^+) = B_{SL}/\tau(D^+) = (1.63 \pm 0.18) \times 10^{11}\ s^{-1} \\ \Gamma_{SL}(D^0) = B_{SL}/\tau(D^0) = (1.64 \pm 0.07) \times 10^{11}\ s^{-1} \end{aligned}$$

The difference in total decay rates must therefore come from non-leptonic decays, for which theoretical understanding is much more difficult.

The following picture emerges: in semileptonic decays D^+ and D^0 decay with the same rate. On the other hand, in hadronic modes a D^0 manages to decay 3 times faster than a D^+. What would make the neutral meson decay much faster than the charged meson? To answer this question, one may refer to the even more striking example of hadronic decays of the strange mesons, where the neutral meson decays 650 times faster than the charged meson:

$$\frac{\Gamma(K_s \to \pi\pi \quad \Delta I = 1/2, 3/2)}{\Gamma(K^+ \to \pi^+\pi^0 \ \ \Delta I = 3/2)} \simeq 650.$$

This effect is known as $\Delta I = 1/2$ rule and is affected by different QCD diagrams shown on Fig. 1.2. Because the charm quark mass m_c is heavy, it turns out that all those diagrams which significantly affect decays of strange mesons are suppressed in case of charm mesons. For example the first diagram called

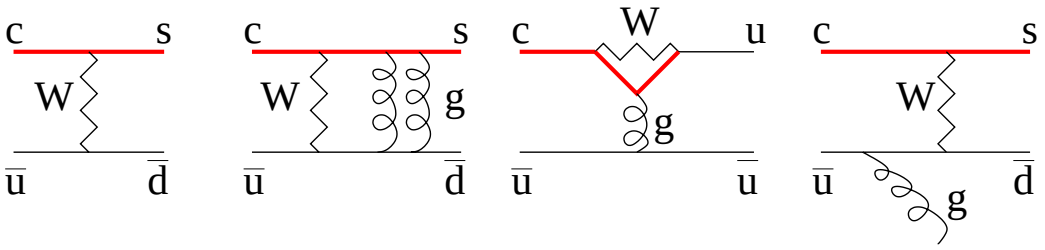

Figure 1.2: Diagrams that affect non-leptonic D^0 decays

W-scattering (WS), is suppressed because the size of the charm quark is small and there is a "wavefunction overlap" penalty $(f_D/m_c)^2 \sim 10^{-2}$, where f_D is pseudo-scalar decay constant. Also, because the D^0 is a spin 0 state, there is a helicity suppression factor of order $(m_s/m_c)^2 \sim 10^{-1}$. Helicity suppression may be weakened by soft gluon emission or the hadronisation processes discussed in Section 1.3.3. One important observation is that decay rate due to WS-diagrams decreases as an inverse power of the mass of heavy quark. To summarise, all these diagrams make the D^0 non-leptonic decay rate only $\sim$ 30-50% faster than D^+ [5], which is not enough to explain the experimentally observed difference of 300%.

1.1.2 Decreasing $\Gamma_{NL}(D^+)$: Pauli Interference

Another look at the situation suggests that the difference in D^+/D^0 non-leptonic decay rates is not because the D^0 decays too fast, but rather because the D^+ decays too slowly. The spectator decay diagram shown on Fig. 1.3. has two $\overline{d}$-quarks which interfere in the final state. The interference effect

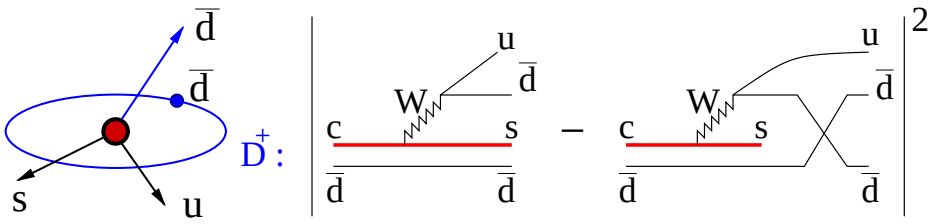

Figure 1.3: Pauli interference in D^+ decay

was generally thought to be small, especially in inclusive decays until it was shown that the two inclusive amplitudes were sufficiently coherent [6]. The

sign of interference is negative, which makes the decay rate of the D^+ smaller and hence the lifetime longer.

For two $\overline{d}$-quarks to interfere their waves should be sufficiently coherent. In the case of the D^+-meson decay the energy of the $\overline{d}$ quark from c-quark decay is about 500 MeV and is comparable to the energy of the spectator light quark $\overline{d}$, about few hundred MeV. One can immediately see that the PI effect decreases as the mass of heavy quark increases, because the $\overline{d}$ quark from the heavy quark decay becomes more energetic than the spectator $\overline{d}$ quark.

The name PI might be misleading as it suggests that interference between two quarks is always destructive. Actually the sign of the interference can be both positive and negative. PI can be destructive (D-mesons, Λ_c^+) and constructive (Ξ_c^0, Ω_c^0). In case of Ξ_c^+ both constructive and destructive amplitudes are present. In calculations of PI it is important to take into account role of QCD corrections. For example without QCD radiative corrections PI in D^+ would have been constructive, rather than destructive [7].

1.2 Heavy Quark Expansion

Ideas embodied in the spectator model, Pauli interference effect and W-annihilation/W-scattering diagrams were united in the so-called Heavy Quark Expansion (HQE) [8, 9, 7, 10]. In this approach the decay rate is expanded as a power series in terms of $(1/M_Q)^n$, where M_Q is the mass of a heavy quark Q.

Properties of heavy mesons are quite similar to properties of isotopes (Figure 1.4). For example the atomic spectra of hydrogen and deuterium are very similar, because the orbiting electron feels only the electric charge of the nucleus. In the first approximation its motion is not affected by the mass of the nucleus. So comparing spectra of deuterium to hydrogen, one would naturally arrive at an expansion in $1/M_N$ for nuclear mass M_N using reduced mass of electron m_r

$$m_r = m_e \frac{M_N}{m_e + M_N} = m_e \left[1 - \frac{m_e}{M_N} + \left(\frac{m_e}{M_N} \right)^2 + \mathcal{O}\left(\frac{m_e}{M_N} \right)^3 \right], \qquad (1.1)$$

Similarly the light quark in a D-meson feels only the colour field of the heavy quark, and in the first approximation its motion is not affected by the mass

Figure 1.4: Similarities between isotopes and particles with heavy quarks

of the heavy quark. Making the analogy to the isotopes one uses a $1/M_Q$ expansion in the HQE.

In the next two sections we will describe HQE calculations for masses and lifetimes of heavy quark particles.

1.2.1 Spectroscopy

First let's describe the application of HQE to calculate masses of pseudoscalar ground states and vector excited states of heavy mesons [9]. The mass of a heavy hadron H_Q is given by the expectation value of its Hamiltonian:

$$M_{H_Q} \;=\; \frac{1}{2M_{H_Q}}\langle H_Q|\mathcal{H}_{\rm tot}|H_Q\rangle\;, \tag{1.2}$$

where the Hamiltonian is the sum of the mass of the heavy quark m_Q, the Hamiltonian of the heavy quark $\mathcal{H}_Q$ and the Hamiltonian of the light degrees of freedom $\mathcal{H}_{\rm light}$:

$$\mathcal{H}_{\rm tot} \;=\; m_Q + \mathcal{H}_Q + \mathcal{H}_{\rm light}\;. \tag{1.3}$$

The Hamiltonian of the heavy quark $\mathcal{H}_Q$ is given by

$$\mathcal{H}_Q \;=\; \frac{1}{2m_Q}\left(\vec{\pi}^2 + \vec{\sigma}\cdot\vec{B}\right) \;+\; \mathcal{O}(1/{m_Q}^2). \tag{1.4}$$

The generalised momentum $\vec{\pi}$ is given by $\vec{\pi} = \vec{p} - \vec{A}$, where $\vec{p}$ is the momentum of the heavy quark, and $\vec{A}$ is the color vector potential. The Pauli term $\vec{\sigma}\cdot\vec{B}$ is due to the interaction of the heavy quark spin $\vec{\sigma}$ with the color "magnetic" field $\vec{B}$ induced by light quarks. Then the mass of the heavy particle is given by:

$$M_{H_Q} = m_Q + \bar{\Lambda} + \frac{1}{2m_Q}\frac{\langle H_Q|\vec{\pi}^2 + \vec{\sigma}\cdot\vec{B}|H_Q\rangle}{2M_{H_Q}} \;+\; \mathcal{O}(1/{m_Q}^2), \tag{1.5}$$

where $\bar{\Lambda}$ is the energy of light quarks and is of the scale of $\Lambda_{\rm QCD}$.

There are two contributions of order $\mathcal{O}(1/m_Q)$ to the mass of the heavy particle:

$$\mu_\pi^2 = \langle H_Q|\vec{\pi}^2|H_Q\rangle \quad (1.6)$$

$$\mu_G^2 = -\langle H_Q|\vec{\sigma}\cdot\vec{B}|H_Q\rangle \quad (1.7)$$

The first one μ_π^2 is due to the kinetic energy of the heavy quark, and the second one μ_G^2 is due to spin-colorfield interaction and is called chromomagnetic operator. Neither μ_π^2 nor μ_G^2 can currently be calculated from QCD first principles, different methods of approximate calculations are discussed in [7, 9, 8]

The second term μ_G^2 is analogous to hyperfine splitting in atoms. The color field $\vec{B}$ is proportional to the spin of the light quarks $\vec{j}$:

$$\vec{B} \propto \vec{j} \quad (1.8)$$

Expanding the square of the total spin of heavy particle $\vec{J} = \vec{\sigma} + \vec{j}$, one can calculate that:

$$\mu_G \equiv -\langle\vec{\sigma}\vec{B}\rangle \propto \left(J(J+1) - j(j+1) - \frac{3}{4}\right). \quad (1.9)$$

For vector and pseudo-scalar states $\langle\vec{\sigma}\vec{B}\rangle_P = -3\cdot\langle\vec{\sigma}\vec{B}\rangle_V$.

The expectation value of $\langle H_Q|\vec{\pi}^2|H_Q\rangle$ is spin independent and is the same for all states in hyperfine multiplet, so $\mu_\pi^2(D) = \mu_\pi^2(D^*)$. Then for heavy mesons:

$$M_D = m_c + \bar{\Lambda} + \frac{\mu_\pi^2(D)}{2m_c} - \frac{\mu_G^2(D)}{2m_c} + \mathcal{O}(1/m_c^2), \quad (1.10)$$

$$M_{D^*} = m_c + \bar{\Lambda} + \frac{\mu_\pi^2(D)}{2m_c} + \frac{1}{3}\cdot\frac{\mu_G^2(D)}{2m_c} + \mathcal{O}(1/m_c^2). \quad (1.11)$$

The expectation value of the chromomagnetic operator in this picture is:

$$\mu_G^2(D) \simeq \frac{3}{4}\cdot 2m_c\cdot(M_{D^*} - M_D) \simeq \frac{3}{4}(M_{D^*}^2 - M_D^2) \simeq 0.41\,\mathrm{GeV}^2 \quad (1.12)$$

Similar calculations for the chromomagnetic operator can be carried out for charm baryons, taking into account that $j_{\Lambda_c} = j_{\Xi_c} = 0$ and $j_{\Omega_c} = 1$. Then

$$\begin{aligned}\mu_G^2(\Lambda_c^+) &\simeq 0\\ \mu_G^2(\Xi_c^+) &\simeq 0\\ \mu_G^2(\Xi_c^0) &\simeq 0\\ \mu_G^2(\Omega_c^0) &\simeq 0.24\,\mathrm{GeV}^2\end{aligned}$$

A value of the kinetic energy of the heavy quark μ_π^2 can be only calculated in different models. On the general grounds it was established that [11, 12]:

$$\mu_\pi^2 > \mu_G^2 \tag{1.13}$$

1.2.2 Lifetimes

The calculation of lifetimes follows the same general pattern as the calculation of masses for heavy hadrons. In this case the decay rate is expanded as a $1/m_Q^n$ series.

$$\Gamma(H_Q \to f) = \frac{G_F^2 m_Q^5}{192\pi^3}|V_{CKM}|^2[c_0^{(f)}\langle H_Q|\bar{Q}Q|H_Q\rangle + c_2^{(f)}\frac{\mu_G^2(H_Q)}{m_Q^2} + \\ + \sum_i c_{3,i}^{(f)} \cdot \frac{\langle H_Q|(\bar{Q}\Gamma_i q)(\bar{q}\Gamma_i Q)|H_Q\rangle}{m_Q^3} + \mathcal{O}(1/m_Q^4)] \ , \tag{1.14}$$

The leading term $\frac{G_F^2 m_Q^5}{192\pi^3}$ is spectator quark decay rate, similar to the basic muon decay formula. $|V_{CKM}|$ is the corresponding CKM matrix element. The coefficients c_n take into account QCD radiative corrections, computed using perturbative QCD methods.

Matrix elements take into account non-perturbative effects and can be computed either using some model, or extracted from related observables [7]. The factor $\mu_G^2(H_Q)$ is the same as was used in the mass calculation (Eq. 1.6). Also, the first matrix element $\langle H_Q|\bar{Q}Q|H_Q\rangle$ can be expressed in terms of μ_π^2 and μ_G^2 [13]:

$$\langle H_Q|\bar{Q}Q|H_Q\rangle = 1 - \frac{\mu_\pi^2 - \mu_G^2}{2m_Q^2} + \mathcal{O}(1/m_Q^3) \tag{1.15}$$

W-annihilation (WA), W-scattering (WS), and Pauli Interference (PI) effects are included in $1/m_Q^3$ term.

Let me make a few comments about the decay formula (Eq 1.14). As $m_Q \to \infty$ the expansion converges to the spectator decay model. Unlike the mass of heavy hadron $M_Q = m_Q\left(1 + \bar{\Lambda}/m_Q + \mathcal{O}(1/m_Q^2)\right)$, there is no $1/m_Q$ term in the decay rate series, which was proven for HQE in [14, 15].

1.2.3 Quark-hadron duality assumption

In QCD theoretical calculations are done in terms of gluons and quarks, which are never detected experimentally. Hadronisation effects are non-perturbative and have not been calculated yet. Quark-hadron duality basically states that rates summed over a sufficient number of hadronic channels can be approximated by rates evaluated for quarks and gluons [16, 17].

The idea of quark-hadron duality was first suggested by Poggio, Quinn and Weinberg [18] to describe the total cross section $\sigma(s)$ for the process $e^+e^- \to$ hadrons . Instead of this exceedingly complicated problem one can calculate simpler cross section $\sigma(e^+e^- \to \text{quarks} + \text{gluons})$. But $\sigma(e^+e^- \to \text{hadrons})$ has resonant peaks that are absent in $\sigma(e^+e^- \to \text{quarks} + \text{gluons})$. So it was suggested that for cross section integrated over large energy region s both processes should have approximately the same answer.

The physical idea is that the process $e^+e^- \to \text{quarks} + \text{gluons}$ happens on small distances, and next process quarks+gluons→hadrons happens when quarks are far apart, and hadronisation effects (resonances, destructive or constructive interferences) can not affect significantly the overall rate of the process.

In case of the lifetime calculations the same approach is taken: instead of calculating the decay of the heavy quark into hadrons, one considers decay into quarks and gluons. The lifetime is a sum over all possible final hadron channels, so possible resonant structures and hadronisation effects are smeared out and do not affect the answer.

Open questions concern the precision of the quark-hadron duality assumption and what the consequences for the lifetime calculations can be. Some authors think that such effects in hadronisation might lead to "forbidden" $\mathcal{O}(1/m_Q)$ corrections [19]. This question is under active current discussion using both numerical [20] and analytical methods [21, 16].

1.3 HQE predictions

In this section we discuss some of the HQE predictions, especially for charm particles, and compare them to experimental measurements.

1.3.1 Semileptonic decay rates for mesons

One of the predictions of the HQE is equal semileptonic decay rates for mesons, because semileptonic decays are driven by the identical spectator decay diagrams in all three mesons D^+, D^0, D_s^+.

Experimental data supports this prediction very well [4]:

$$\begin{aligned} \Gamma_{SL}(D^+) &= (1.63 \pm 0.18) \times 10^{11}\, s^{-1} \\ \Gamma_{SL}(D^0) &= (1.64 \pm 0.07) \times 10^{11}\, s^{-1} \\ \Gamma_{SL}(D_s^+) &= (1.6 \pm 1.1) \times 10^{11}\, s^{-1} \end{aligned}$$

The semileptonic decay rate for the D_s^+ is the least precise measurement, but that should change soon, given copious data on D-meson decays in Fermilab fixed target experiments and in e^+e^- B-factories.

1.3.2 D^+/D^0 lifetime difference

The difference between D^+ and D^0 lifetimes comes mostly from Pauli interference between $\bar{d}$-quarks in D^+ decay. This effect is proportional to the $1/m_c^3$ term in the HQE series.

Calculations by Bigi and Uraltsev [22] based on the HQE expansion show that:

$$\frac{\tau(D^+)}{\tau(D^0)} \simeq 1 + (\frac{f_D}{200 MeV})^2 \sim 2,$$

Blok and Shifman in [10] also got similar answer: $\tau(D^+)/\tau(D^0) \sim 2$. Recent calculations of matrix elements using QCD sum rules done by Cheng and Yang [23] state that $\tau(D^+)/\tau(D^0) \simeq 2.56 \pm 0.52$. In each case due to the complexity of the problem, calculations of PI effects are very approximate. The large size of the effect raises the question of applicability of HQE for charm decays: PI is the third term in HQE series, and it is as big as the first term. For charm hadrons the convergence of the series and the influence of $1/m_c^4$ and higher terms are open questions.

Experimentally ratio of lifetime is [4]:

$$\frac{\tau(D^+)}{\tau(D^0)} = 2.547 \pm 0.035\ . \tag{1.16}$$

1.3.3 D_s^+/D^0 lifetime difference

There are a lot of similarities between D_s^+ and D^0 decays, which make their lifetimes almost equal. Thus, precision measurement of both lifetimes is quite important to verify theoretical calculation.

D_s^+ and D^0 have the same spectator decay diagram. Differences arise from the leptonic decay $D_s^+ \to \tau^+\nu_\tau$, Pauli interference in D_s^+ Cabibbo suppressed decay, the kinetic operator μ_π^2, the chromomagnetic operator μ_G^2 (Eq. 1.6), and WA/WS diagrams in D_s^+ and D^0.

Leptonic decay $D_s^+ \to \tau^+\nu_\tau$

Unlike the D^0, the D_s^+ has the additional leptonic WA decay (Figure 1.5), which makes it decay faster, and hence decreases the D_s^+ lifetime. The decay rate is defined by the decay constant f_{D_s}.

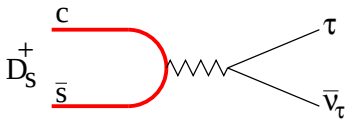

Figure 1.5: $D_s^+ \to \tau^+\nu_\tau$ leptonic decay

As in $\pi^+ \to \mu^+\nu_\mu$ [5], the leptonic decay rate is given by:

$$\Gamma(D_s^+ \to \tau^+\nu_\tau) \simeq \frac{G_F^2 m_\tau^2 f_{D_s}^2 M_{D_s}}{8\pi}|V_{cs}|^2(1 - m_\tau^2/M_{D_s}^2)^2. \tag{1.17}$$

For $f_{D_s} \simeq 280$ MeV [24] one can numerically estimate leptonic decay rate as:

$$\Gamma(D_s^+ \to \tau^+\nu_\tau) \simeq 0.05\,\Gamma(D^0) \tag{1.18}$$

Pauli Interference in D_s^+ Cabibbo suppressed decay

Analogue to the D^+ decay which has two identical $\overline{d}$-quarks in the final state, the D_s^+ can have two identical $\overline{s}$-quarks in Cabibbo suppressed spectator decay $c \to s\overline{s}u$ (Figure 1.3.3). The two $\overline{s}$ antiquarks interfere in the final state.

An estimate of this effect $\Gamma_{PI}(D_s^+)$ can be derived from the D^+/D^0 lifetime difference, which is driven mostly by PI in D^+ decay. In the D_s^+ the

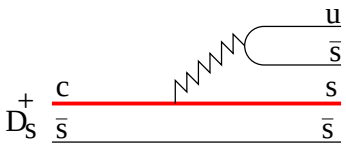

Figure 1.6: Cabibbo-suppressed D_s^+ decay

effect of PI is also destructive and decreases the decay rate. It is also suppressed by a factor $\tan^2\vartheta_c$ compared to the D^+. There is an additional factor S due to $SU(3)_f$ symmetry breaking, which reflects a difference between $\overline{d}$-quark and $\overline{s}$-quark interference:

$$\Delta\Gamma_{PI}(D_s) \simeq S \cdot \tan^2\vartheta_c(\Gamma(D^+) - \Gamma(D^0)), \tag{1.19}$$

so for $S \simeq 1.4$ [25] $\Gamma_{PI}(D_s)$ can be numerically estimated as:

$$\Delta\Gamma_{PI}(D_s^+) \simeq -0.04\,\Gamma(D^0). \tag{1.20}$$

Difference in μ_G^2 and μ_π^2 operators

Due to $SU(3)_f$ symmetry breaking, the heavier s-quark makes the c-quark move a little faster in the D_s^+ meson than in the D^0 meson. This effect increases the D_s^+ lifetime compared to the D^0.

The impact of the chromomagnetic operator μ_G^2 can be derived from the mass differences of the ground pseudo-scalar state and excited vector states:

$$\mu_G^2(D_s^+) \simeq \frac{3}{4}(M_{D_s^*}^2 - M_{D_s}^2) \;=\; 0.440\ \text{GeV}^2 \tag{1.21}$$

$$\mu_G^2(D^0) \simeq \frac{3}{4}(M_{D^{0*}}^2 - M_{D^0}^2) \;=\; 0.413\ \text{GeV}^2 \tag{1.22}$$

The μ_G^2 contribution to the lifetime difference is in the first and second terms of Eq 1.14:

$$\frac{\Delta\Gamma_{\mu_G^2}(D_s^+)}{\Gamma} = C \cdot \frac{\mu_G^2(D_s^+) - \mu_G^2(D^0)}{2 \cdot m_c^2} \simeq C \cdot 0.005, \tag{1.23}$$

where $C \sim 1$ is a coefficient that depends on $c_0^{(f)}, c_2^{(f)}$ arising from QCD radiative corrections [25]. An important point is that even with large variations of C, the contribution of μ_G^2 to the D_s^+/D_0 lifetime difference is small due to $SU(3)_f$ symmetry.

The lifetime difference due to the kinetic operator μ_π^2 can be estimated from the spin-averaged masses of heavy mesons, which does not depend on μ_G^2. The spin-averaged mass is given by:

$$\langle M_D \rangle \equiv \frac{M_D + 3M_{D^*}}{4} \simeq m_c + \bar{\Lambda}(D) + \frac{\mu_\pi^2(D)}{2m_c} + \mathcal{O}(1/m_c^2)., \tag{1.24}$$

The difference in kinetic operators is given by [25, 13]:

$$\mu_\pi^2(D_s^+) - \mu_\pi^2(D^0) \simeq \frac{2m_b m_c}{m_b - m_c} \left([\langle M_{D_s} \rangle - \langle M_D \rangle] - [\langle M_{B_s} \rangle - \langle M_B \rangle] \right). \tag{1.25}$$

The B_s^* mass is not measured yet, but based on analysis of observed B^*, B mass spectra and comparing it to D^*, D spectra, one can conservatively estimate the decay rate difference by [25]:

$$\frac{\Delta\Gamma_{\mu_\pi^2}(D_s^+)}{\Gamma} = -\frac{\mu_\pi^2(D_s^+) - \mu_\pi^2(D^0)}{2m_c^2} \simeq -0.04 \tag{1.26}$$

Contribution of WA/WS diagrams

Both D^0 and D_s^+ have WA or WS diagrams (Figure 1.7), which can be further complicated by gluon emission (Figure 1.2) and hadronisation processes.

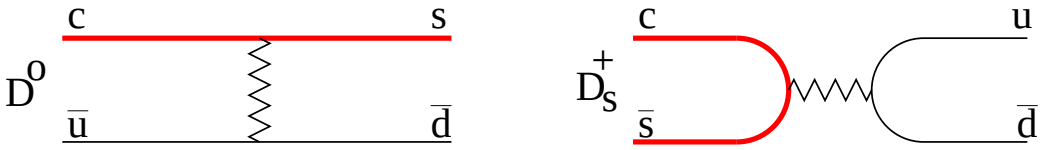

Figure 1.7: Tree WA/WS diagrams in D_s^+, D^0 decays

The contribution of all WA/WS diagrams to the total decay rate is not yet calculated well. The largest uncertainty in this calculation is in the size of helicity suppression. In tree diagrams the D^0 decay WA amplitude is helicity suppressed by a significant factor about $m_s/m_c \simeq 0.1$. It is suppressed even more strongly in the D_s^+, which has only u, d-quarks in the final state. Hence tree WA/WS diagrams can only add few percent to D_s^+/D^0 lifetime difference. However non-perturbative effects (soft gluon emission, hadronisation) can decrease helicity suppression effects. As a result WA diagrams can affect the D_s^+/D^0 lifetime difference by as much as $10 - 20\%$

[26]. Due to the complexity of the problem neither the size, nor even the sign of the contribution of WA diagrams can be currently calculated.

Different contributions to the D_s^+/D^0 lifetime difference are summarized in Table 1.1. The first three terms give a few percent to D_s^+/D^0 lifetime difference. The contribution of the WA term depends on the strength of helicity suppression and can range up to 10-20%.

Contribution	$\frac{\tau(D_s^+)-\tau(D^0)}{\tau(D^0)}$
Leptonic decay $D_s^+ \to \tau^+\nu_\tau$	-5%
PI in Cabibbo Suppressed D_s^+ decay	$+4\%$
Difference in μ_G^2 and μ_π^2	$+4\%$
WA in D^0 and D_s^+ decays	$\pm$10-20%

Table 1.1: Contributions to D_s^+/D^0 lifetime difference

These calculations are based on extracting matrix elements from the masses of heavy particles. Another approach is based on calculation of matrix elements using QCD sum rules. This approach gives a lifetime ratio close to unity [23]:

$$\frac{\tau(D_s^+)}{\tau(D^0)} \simeq 1.08 \pm 0.04 \tag{1.27}$$

Prior to the E791 measurement [28] in 1999, the D_s^+ and D^0 lifetimes were not measured precisely enough to compare theoretical predictions with data (Figure 1.8). Theory predicted the difference to be of the order of a few percent, since WA/WS processes were believed to be small. Experimentally the situation changed when E791 measured D_s^+/D^0 ratio to a few percent precision and found 6σ deviation from unity: $\frac{\tau(D_s^+)}{\tau(D^0)} = 1.19 \pm 0.03$ [28]. Subsequent CLEO measurement [29] and preliminary results from FOCUS [30] and SELEX [31] also support the E791 and CLEO measurement that D_s^+/D^0 lifetime ratio is bigger than simple prediction of few percent.

The current situation in the D_s^+/D^0 lifetime ratio is a good example of how precise measurements open a whole set of theoretical questions (contribution of WA processes, effects of quark-hadron duality) which were not previously addressed in great detail, due to the poor experimental measurements.

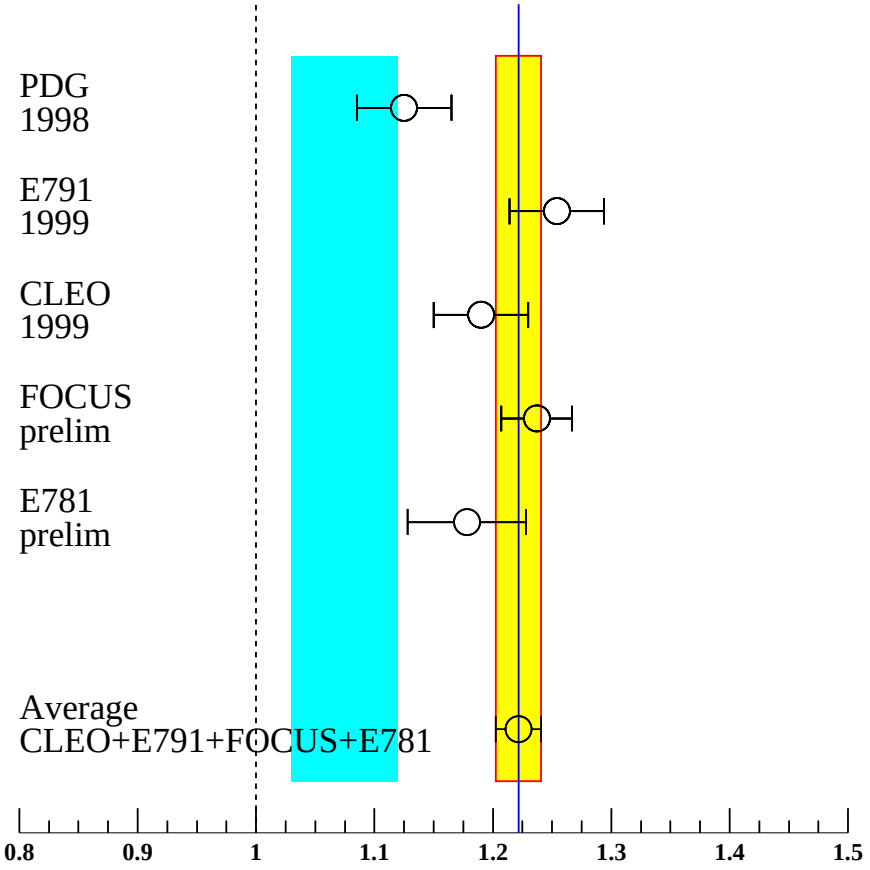

Figure 1.8: Experimental measurements of D_s^+/D^0 lifetime ratio. Particle Data Group value [27] combines results prior to 1998. Recent results are published by E791 [28], CLEO [29]. There are also preliminary results by FOCUS [30] and E781 [31]. Shadowed region shows theoretically "comfortable" region [23, 7].

1.3.4 Charm Baryon lifetimes

Calculation of charm baryon lifetimes is even more complicated than for mesons. The only simplification is that chromomagnetic operator μ_G^2 vanishes for Λ_c^+, Ξ_c^+ and Ξ_c^0 baryons, since the total spin of the light quarks $\vec{j} = 0$ (Eq. 1.9). While the $1/m_c^2$ terms for these baryons are simpler than for mesons, the $1/m_c^3$ terms are much more complicated. They include WA/WS terms similar to D-mesons, but they are not helicity suppressed. They also include PI terms which can be either destructive as in D^+ decay or constructive [32, 10]. So decay rates for baryons are given by:

$$\begin{aligned}
\Gamma(\Lambda_c^+\ cud) &\simeq \Gamma_0(1 + \frac{\mu_\pi^2}{2 \cdot {m_c}^2} + WS - PI_{uu}) \\
\Gamma(\Xi_c^+\ csu) &\simeq \Gamma_0(1 + \frac{\mu_\pi^2}{2 \cdot {m_c}^2} + PI_{ss} - PI_{uu}) \\
\Gamma(\Xi_c^0\ csd) &\simeq \Gamma_0(1 + \frac{\mu_\pi^2}{2 \cdot {m_c}^2} + WS + PI_{ss}) \\
\Gamma(\Omega_c^0\ css) &\simeq \Gamma_0(1 + \frac{\mu_\pi^2}{2 \cdot {m_c}^2} + \frac{\mu_G^2}{2 \cdot {m_c}^2} + \frac{10}{3} \cdot PI_{ss}).
\end{aligned}$$

Terms of order $1/m_c^3$ can be calculated within the framework of some model generally not to very high precision. On general grounds one can conclude only inequalities:

$$\begin{aligned}
\Gamma(\Lambda_c^+) &< \Gamma(\Xi_c^0) \\
\Gamma(\Xi_c^+) &< \Gamma(\Xi_c^0).
\end{aligned}$$

Different calculations of baryon lifetimes are summarized in Table 1.2. The authors do not quote the error on their calculations, but rather state that the numerical values are just estimates to establish the lifetime hierarchy.

1.3.5 Charm and Beauty lifetimes

One immediate prediction of HQE is that lifetimes of beauty hadrons should be much closer than for charm hadrons. In HQE decay rate of beauty hadron H_b is given by:

$$\Gamma(H_b \to f) = \Gamma_0(1 + A_2/{m_b}^2 + A_3/{m_b}^3 + ...) \tag{1.28}$$

	Ref. [10] [a]	Ref. [32] RBM [b]	Ref. [32] NRM [c]	Ref. [4] PDG [d]
$\tau(\Xi_c^+)/\tau(\Lambda_c^+)$	1.3	1.2	1.6	1.6 ± 0.2
$\tau(\Xi_c^0)/\tau(\Lambda_c^+)$	0.45	0.75	0.7	0.5 ± 0.1
$\tau(\Omega_c^0)/\tau(\Lambda_c^+)$	0.3	0.75	0.6	0.3 ± 0.1
$\tau(D^+)/\tau(\Lambda_c^+)$	5	2.8	4.5	5.1 ± 0.3

Table 1.2: Theoretical calculations of charm baryon lifetimes.
[a] Blok and Shifman (1993)
[b] Guberina et.al. (1986) Relativistic bag model
[c] Guberina et.al. (1986) Non-relativistic quark model
[d] Experimental data summarized by Particle Data Group (2000)

Indeed the second term in the series A_2/m_b^2 is about 10 times smaller than for charm decays. The third term A_3/m_b^3 is about 30 times smaller than for charm decays. So in b-hadron the decay rate is mostly defined by the the spectator decay rate Γ_0, which means that in b-hadrons the b-quark decays almost as a free quark. Also faster convergence of the $1/m_b^n$ series makes HQE much more applicable for beauty hadrons than for charm hadrons. Comparison of theoretical and experimental results for charm and beauty hadrons is presented on Figure 1.9. Indeed one see that measured beauty lifetimes are much closer than for charm. Theoretical predictions are shown with red lines, but they of course have large errors, because most of them are estimates. As theorists do not quote errors on their prediction, they are skipped on this plot.

Despite the fact that theorists agree that HQE is much more applicable to b-hadrons, there might be a problem in the Λ_b lifetime. The lifetime ratio between Λ_b baryon and B-mesons is predicted to be $\tau(\Lambda_b)/\tau(B) \simeq 0.9$ [33, 34]. Experimentally this ratio is 0.77 ± 0.05, which is an emerging problem in HQE calculations. Some theorists are trying to solve this problem by introducing a "forbidden" $1/m_Q$ term in the decay rate series (Eq 1.28) and justifying it by quark-hadron duality violation [20, 35]. Perhaps a careful study of charm lifetimes can shed some light on this problem in b-sector [36].

Comparison of the charm and beauty lifetimes is not trivial: one can not directly use the coefficients A_2, A_3 for the charm hadrons and apply them to the beauty lifetimes. QCD corrections for the charm and beauty decay are quite different, because the typical momentum in charm decay is

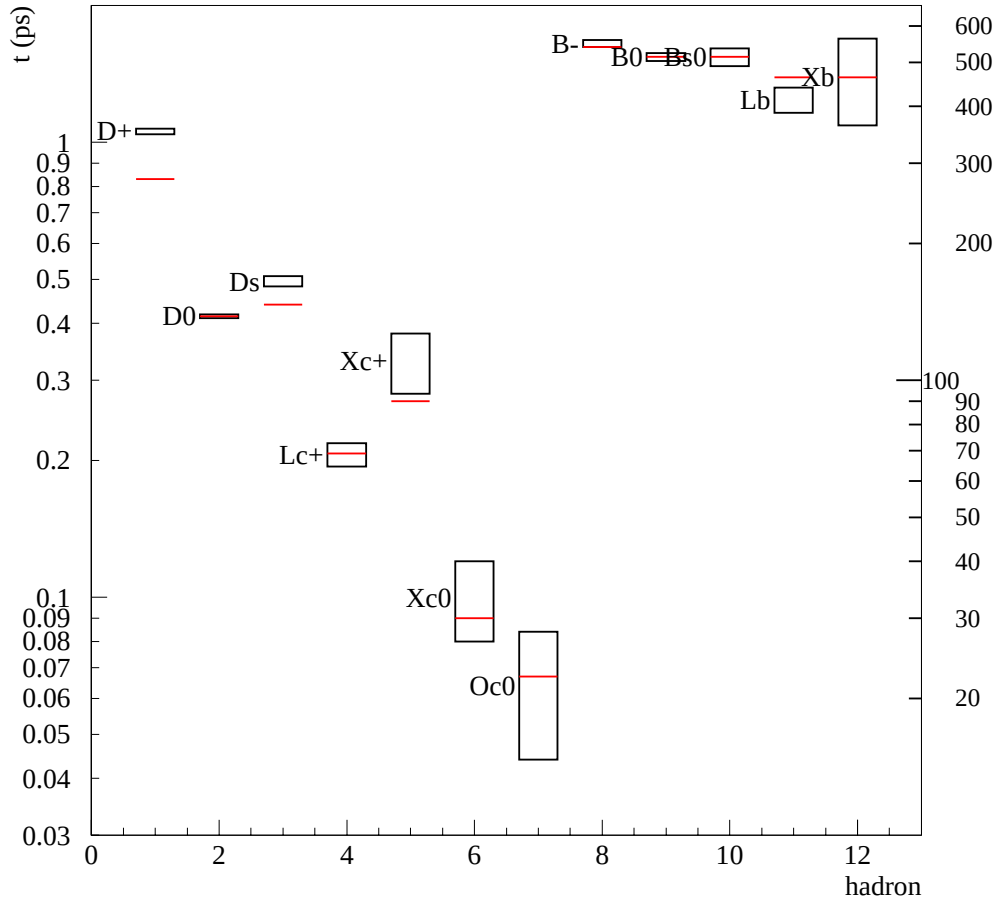

Figure 1.9: Comparison of the experimental measurements with the theoretical calculations of charm and beauty lifetimes. The black boxes represent the experimental measurements averaged by Particle Data Group [4]. The vertical size of the box shows the error of the measurement. The red lines show theoretical calculations [7], which have large errors, but they are not shown, as theorists in most cases do not quote them.

about 500 MeV, and in beauty decay it is about 1500 MeV. Hence all strong corrections and matrix elements in HQE should be recalculated at a different momentum scale. Despite the complications the simultaneous study of HQE in both charm and beauty sectors is very promising.

Overall it is clear that HQE is more applicable for decays of b-hadrons. On the other hand, small lifetime differences can hide problems in b-hadron analyses, since the observation of small differences requires much higher precision in experimental measurements. To contrast that the small mass of the charm quark works as a magnifying glass and makes the charm sector a better test ground to verify different approaches in heavy quark theories.

1.4 Conclusion

The overall picture of charm and beauty lifetimes shows that new precise lifetime measurements raised questions that had been previously undeveloped in theoretical calculations due to poor experimental measurements. A precision measurement of the D_s^+/D^0 lifetime ratio [28, 29] brought attention back to the issue of the strength of helicity suppression in WA/WS decays of D-mesons. Also effects of "quark-hadron" duality are under active discussion again, which are driven by precision lifetime measurements in the beauty sector [16], as well as in the charm sector [37].

Insufficient development of the theory of charm baryon decays has been excused by poor experimental data. In this work we decrease the Λ_c^+ lifetime measurement error by a factor of 2 compared to previous best measurement [38], which is an important experimental contribution to HQE study. More precise measurements of Ξ_c^+, Ξ_c^0 baryons lifetime are very valuable. They can illuminate problems in HQE calculations [16]. Preliminary results from FOCUS [39] became available just few month ago.

The last 2 years produced important new experimental results on charm lifetimes [28, 29, 40, 41, 42, 43], and more new results are expected soon [30, 31, 39]. This experimental progress revitalized theoretical calculations and is an important step in understanding heavy quark physics.

Chapter 2

SELEX experiment

Data for this analysis were taken in SELEX (E781) experiment. SELEX (Segmented Large x_F Baryon Spectrometer) was a new multi-stage spectrometer with high acceptance for forward interactions and decays. It took data in 1996-97 with 600 GeV Σ^-, π^- and 540 GeV p beams. The **goal** of SELEX was to obtain large sample of charm baryon decays using a variety of incident beam particles and targets.

2.1 SELEX Physics Program

SELEX experiment has a wide physics program which included both charm and non-charm physics topics.

2.1.1 Charm physics program

Charm hadro-production

Production of heavy quarks can be described by the perturbative QCD, but the hadronization of heavy quarks is non-perturbative process. The hadronization process can significantly affect a heavy quark's momenta after it is produced. Hadronization is described by models, which need experimental input to confirm them and establish their parameters. At hadron machines many important studies involve heavy quarks in the final state: top-production, Higgs decay, supersymmetry searches to name a few. Also large backgrounds in this studies come from QCD production of heavy quarks. In many studies signals are quite small, so reliable description of both signal

and background properties is the very important in the simulations. How can this information be checked?

The SELEX experiment can study charm hadroproduction in three different beams: Σ^-, π^- and p beams, which makes it a unique experiment. The experiment was designed to detect decays in the wide momentum range ($x_F > 0.1$), where x_F is approximately the fraction of the beam momentum carried by the charm particle. Study of the large x_F region is especially valuable, because that is the region where charm and anti-charm particle production differs the most [31].

In the SELEX experiment we study x_F and P_t distributions for charm and anticharm particles, charm-anticharm production asymmetry [44, 31]. The SELEX experiment also plans to study production of charm excited states, as well as charm pair production.

The production polarization of the charm baryons is similar to hyperons (Section 2.1.2) and is predicted by some models. A study of this effect is an important input in the understanding of heavy quark production and hadronization dynamics. Experimental data on this question is very limited [45].

Decay Physics

Having a large sample of charm decays allowed us to do precision measurements of charm lifetimes. For control of systematic errors it is important that the lifetimes of all stable charm particles be measured in the same apparatus. These lifetimes provide a valuable input to test the Heavy Quark Expansion calculations (Chapter 1).

Another important topic is the study of new decay modes and their branching ratios. Theoretical calculation of branching ratios of explicit decays of heavy quarks is still one of the most challenging areas of hadron physics. Experimental input is vital to understand decay dynamics.

The state-of-the-art particle identification system in the SELEX greatly helped in the study of Cabibbo-suppressed decays. These studies investigate the role of final state interactions in hadronic decays. The SELEX experiment was the first experiment to observe the decay $\Xi_c^+ \to pK^-\pi^+$ [46]. Semileptonic charm decays are theoretically better understood than hadronic decays, and new experimental data can push theoretical calculations to new levels of accuracy.

Charm spectroscopy

The majority of charm excited states can be detected and measured in the SELEX experiment. We plan to study excited state characteristics, such as mass and width. For example, the mass splitting of Σ_c and Λ_c^+ is an important test of HQET [47]. Widths of excited states are valuable input to HQET, and there is little experimental data available [48]. Confirmation of Ξ_c' states observed only by CLEO [49] would be an important accomplishment. We also plan to search for new excited states, especially for charm baryons.

2.1.2 Non-Charm physics program

Measurement of total cross sections

The hadronic total cross section is one of the most fundamental measurements of the strength of hadronic interactions. The total cross section initially decreases as a function of center of mass energy, and after about 10 GeV starts to grow again. SELEX measured Σ^- and π^- total cross sections on beryllium, copper, carbon and polyethylene targets. Also the total cross section was measured for protons on beryllium and carbon targets [50]. All measurements were done at 600 ± 50 GeV beam energy. These data were used to extract Σ^--p and π^--p total cross sections. This is the highest energy Σ^--p total cross section measurement. The previous highest energy measurement was done at 140 GeV [51]. The measurements clearly showed a rise of the Σ^--p cross section as a function of the center of mass energy.

Measurement of hadronic charge radii

The charge radius provides information about the internal structure of hadron. This measurement is important to verify models which describe confinement of quarks inside the hadron. Different theoretical calculations of charge radii give quite different answers and experimental input can clarify the situation [52]. Charge radii of π^-, Σ^-, p were measured in the SELEX experiment by studying π^--e [53] Σ^--e [52] and p-e [54] scattering.

Production polarization of hyperons

The discovery of the interaction of an unpolarized proton beam with unpolarized target which produced polarized hyperons in 1976 came as a complete

surprise [55]. Even after 24 years extensive experimental data still remain widely unexplained [56]. Hadronization is expected to play a major role in this process. SELEX measured production polarization of Σ^+ [57] and Λ^0 [58] as a function of x_F and p_T.

Other topics of the non-charm physics program include Primakoff production of excited states, pion polarizability, chiral anomaly tests and search for exotic states.

2.2 SELEX Apparatus

2.2.1 Apparatus overview

The heart of the experiment was the Vertex Silicon Strip Detector (SSD) capable of 4 μm transverse position resolution at 600 GeV. The vertex separation L was measured with precision $\sigma_L \simeq 0.5\,\mathrm{mm}$. It is very important to have small a error on vertex separation, as its significance L/σ_L is by far the most powerful cut to separate the charm signal from the background.

The SELEX experiment had an extensive particle identification system. Beam particles ($\Sigma^-/\pi^-, p/\pi^+$) were tagged with the Beam Transition Radiation Detector (TRD). The 3000 phototube Ring Imaging Cherenkov Counter (RICH) was used to identify the secondary particles: electrons, muons, pions, kaons, protons and even hyperons. The RICH detector was capable of K/π separation up to 165 GeV. The separation of the kaons from the pions is a vital feature for any charm experiment, because charm decays usually have kaons in the final state. The Electron Transition Radiation Detectors (ETRD) were used to separate electrons from the hadrons, which is important for the semileptonic decay physics. Three lead glass detectors were used to identify and measure the energy of the photons and electrons.

SELEX also has a precise tracking system and 3 analyzing magnets to measure particle momenta. Eight Beam SSD planes with hit resolution $\sigma \sim 6\,\mu$m were used to measure track parameters. The downstream tracking system included 26 proportional wire chambers (PWC) planes with hit spatial resolution $\sigma \sim 0.6 - 1\,\mathrm{mm}$. It also included three Vector Drift Chambers (VDC) each having 8 sensitive planes with hit resolution $\sigma \sim 100\,\mu$m. And finally there were 18 large SSDs with hit resolution $\sigma \sim 14\,\mu$m to measure very high-momentum tracks. In total SELEX the SSD system has 74000 strips.

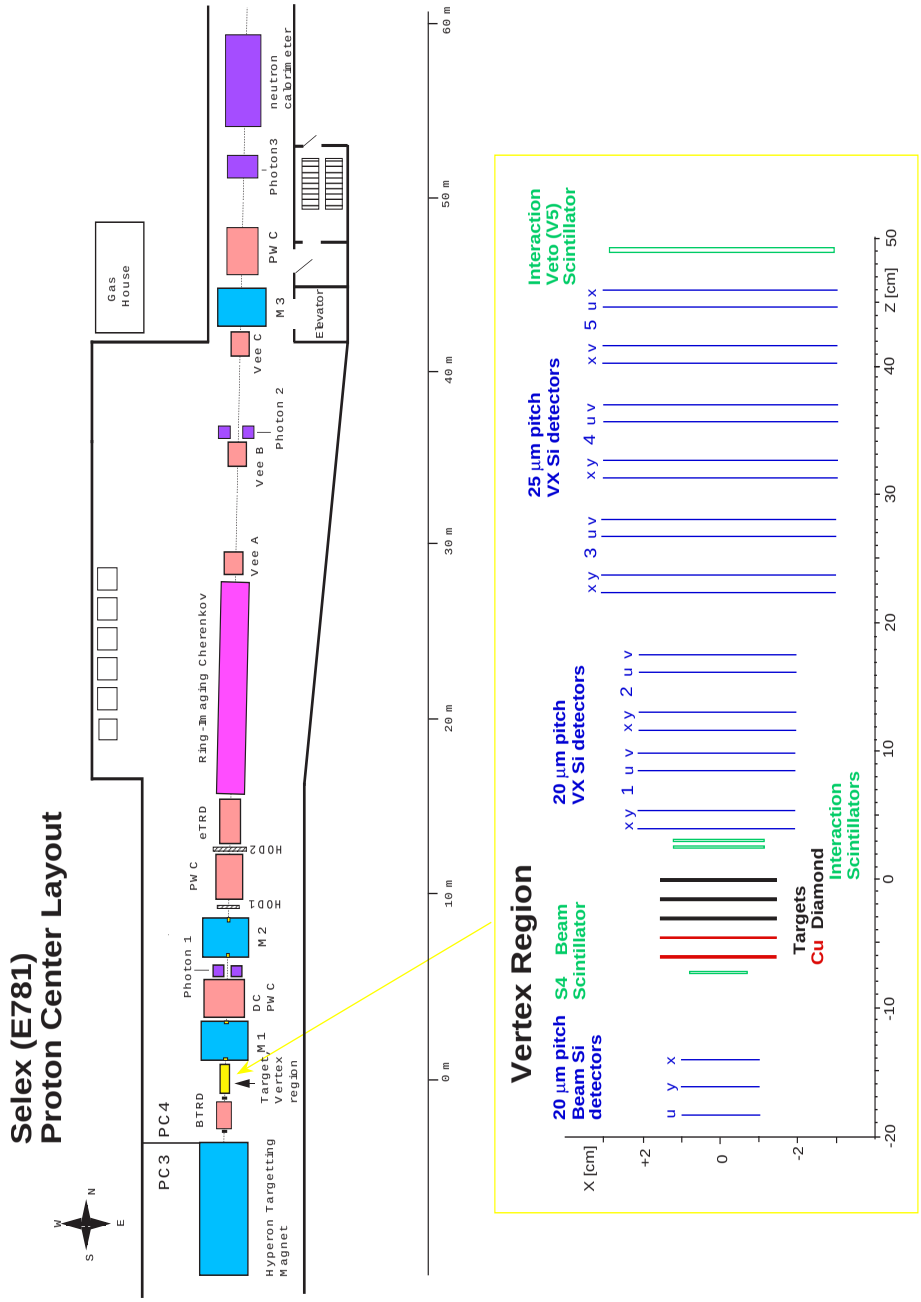

Figure 2.1: Schematic view of SELEX spectrometer and vertex region

2.2.2 SELEX coordinate system and spectrometers

The origin of the coordinate system is chosen to be in the middle of the downstream surface of the downstream target (Figure 2.2). The z-axis is along the beam direction, the y-axis is vertically up and the x-axis completes a right-handed coordinate system. Most detectors measured tracks in x, y projections, or in u, v projections, which form $\pm 45^0$ angle with respect to x, y axis.

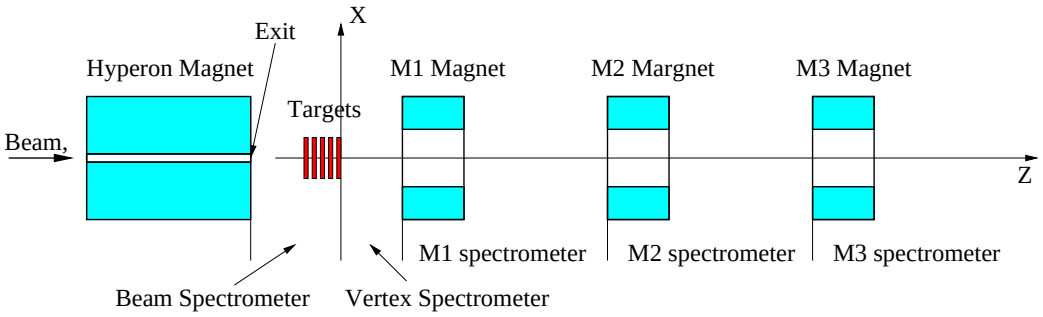

Figure 2.2: Schematic view of SELEX spectrometers (Off-scale).

The beam spectrometer included apparatus between the exit of the hyperon magnet and target region. The vertex spectrometer was between the targets and M1 magnet. The M1,M2,M3 spectrometers were located after the corresponding analyzing magnets.

2.2.3 Analyzing magnets

SELEX apparatus has 3 analyzing magnets that were used to measure track momenta. The magnetic fields for each magnet were measured with a flip-coil apparatus that determined B_x, B_y and B_z components on a 1-inch grid with a precision of 0.1%. These maps were used to propagate the particle tracks inside the magnets. Main parameters of the magnets are summarized in Table 2.1.

2.2.4 Beam Spectrometer

Hyperon beam. 800 GeV protons from the Fermilab Tevatron accelerator hit a 1 interaction length beryllium target. Forward-going secondary particles enter a thin (about $0.5 \times 0.5\,\mathrm{cm}$) 7.3 m long curved channel inside the

name	z [cm][a]	aperture [cm]×[cm][b]	B [kG][c]	p_t [GeV][d]
M1	190	61 x 51	11.98	0.73
M2	745	61 x 25	14.66	0.84
M3	4240	61 x 51	6.85	0.42

Table 2.1: Parameters of magnets in SELEX apparatus
[a] position of the center of the magnet along z-axis.
[b] the first dimension correspond to the horizontal and the second to the vertical size of the aperture.
[c] central field in the magnet.
[d] p_t-kick of the magnet - the transverse momenta that particle gains passing through the magnet.

3.5 T hyperon magnet. Only high energy particles about 600 ± 50 GeV can go through the magnet. Others are lost in tungsten walls of the channel (Figure 2.3). The relative fraction of hyperons in the secondary beam grows with the energy[59, 60]. Hence selecting high energy particles enhances the fraction of hyperons. At the target region the 600 GeV negative secondary beam consisted of approximately 50.9% π^-, 46.3% Σ^-, 1.6% K^- and 1.2% Ξ^-. With the opposite polarity of the magnetic field secondary beam consisted of approximately 89.2% protons, 5.7% π^+, 2.7% Σ^+ and 2.4% K^+ [50].

Beam Transition Radiation Detectors. Particles in the hyperon beam were tagged in the 10 Beam TRDs. Each module has a radiator made of 200 polypropylene foils 17 μm thick followed by 3 proportional wire chambers filled with the mixture of Xe+30% CH_4 gas, to detect transition radiation [62]. A relativistic particle crossing the boundary of media with different dielectric constants emits transition radiation photons. Typically the energy of such photons is a few keV. The probability of radiation of transition radiation photon is proportional to the Lorentz γ-factor. Hence a π^--meson produces more hits in the Beam TRD detectors than a baryon of the same energy. The total number of hits in the Beam TRD was used to separate the baryon component from the meson component of the beam (Figure 2.4). Beam TRD information was used in the T1 trigger (Section 2.3) to increase the fraction of Σ^- beam particles in the recorded interactions.

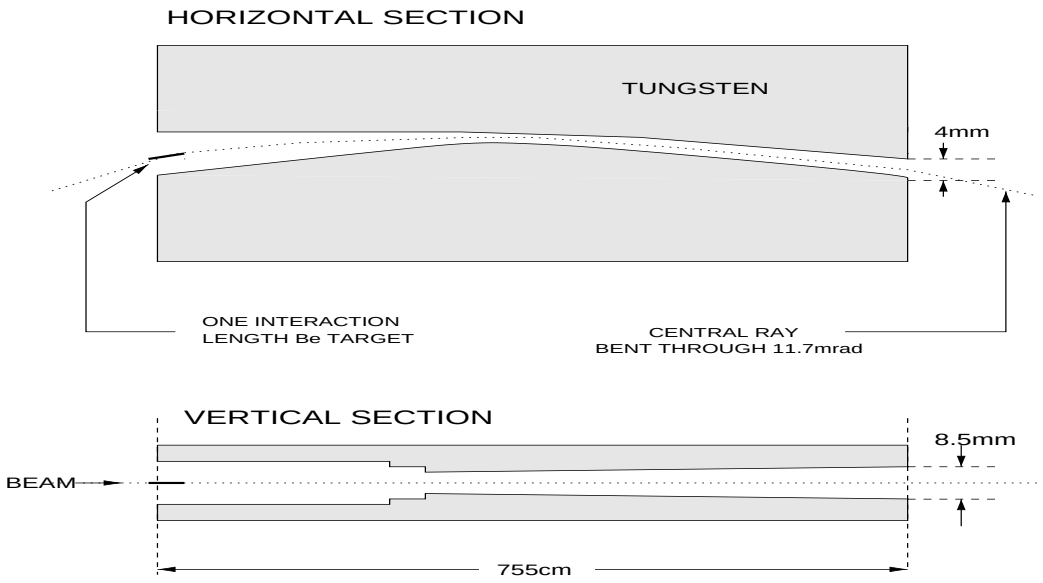

Figure 2.3: Schematic layout of the hyperon beam magnet [61].

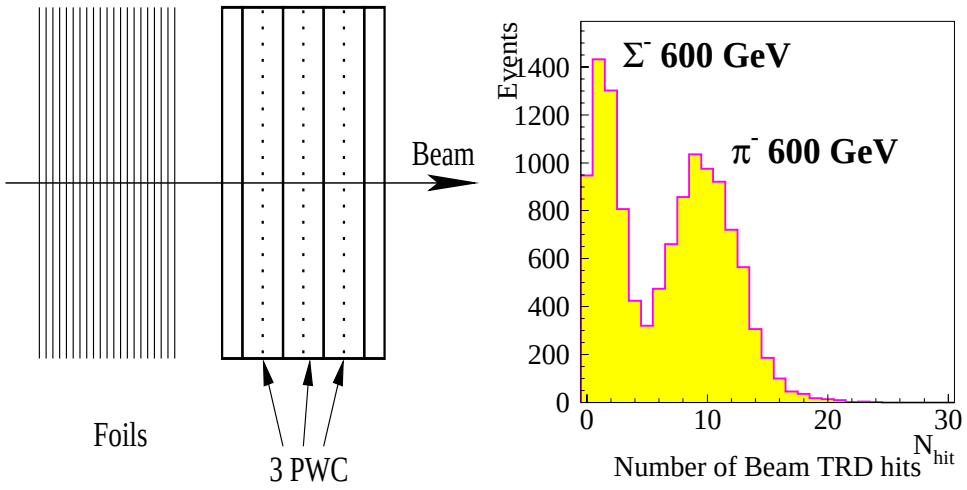

Figure 2.4: Schematic layout of the Beam TRD. Σ^-/π^- separation using the number of hits in the Beam TRD.

Beam silicon strip detectors. Beam tracks were measured with 8 planes of 20 μm pitch silicon strip detectors (SSD). Beam SSDs determined position of the beam track in the charm targets with about 4 μm resolution. Each detector has 1024 strips read out by SVX chips and has 2×2 cm sensitive area. Because the integration gate of the readout electronics was a few microseconds long, information about several beam tracks from the 1 MHz beam was stored in the beam SSD hit output. The beam track which triggered the event was identified using the hardware scattering silicon detectors and also using hit information from the vertex SSD.

Hardware scattering trigger silicon detectors (HSD). Four 50 μm-pitch SSD [63] were used to identify the beam track which triggered the interaction. They employed short 80 ns gates, so that only hits from the beam particle that triggered the event were read out. Beam track candidates were extrapolated from the Beam SSD to the HSD planes. The track that had 2 or more matching hits in the HSD was identified as the trigger beam track.

Charm targets. Beam particles interacted in 5 targets with combined interaction length 4.3%. Target spacing was 1.5 cm. Target properties are summarized in Table 2.2. Different materials were used to study charm production as a function of A.

target	material	thickness [mm]	z [cm]	Atomic number A	Density [g/cm^3]	Inter length [%]
1	copper	1.6	-6.13	63.5	8.96	1.06
2	copper	1.1	-4.62	63.5	8.96	0.76
3	diamond	2.2	-3.10	12	3.20	0.82
4	diamond	2.2	-1.61	12	3.20	0.82
5	diamond	2.2	-0.11	12	3.20	0.82

Table 2.2: Charm target properties

2.2.5 Vertex spectrometer

Vertex Silicon Strip Detectors. 20 SSDs downstream of the charm targets detected secondary tracks with high spatial resolution. The first 8 detectors, called 5-cm detectors, have 20 μm pitch and 5.1×5.0 cm^2 active area.

The downstream 12 detectors, called mosaic detectors, have 25 μm pitch and $8.3 \times 9.6\,\mathrm{cm}^2$ active area. The detectors were mounted on special granite optical bench, and measured tracks in x, y, u and v projections (Figure 2.5).

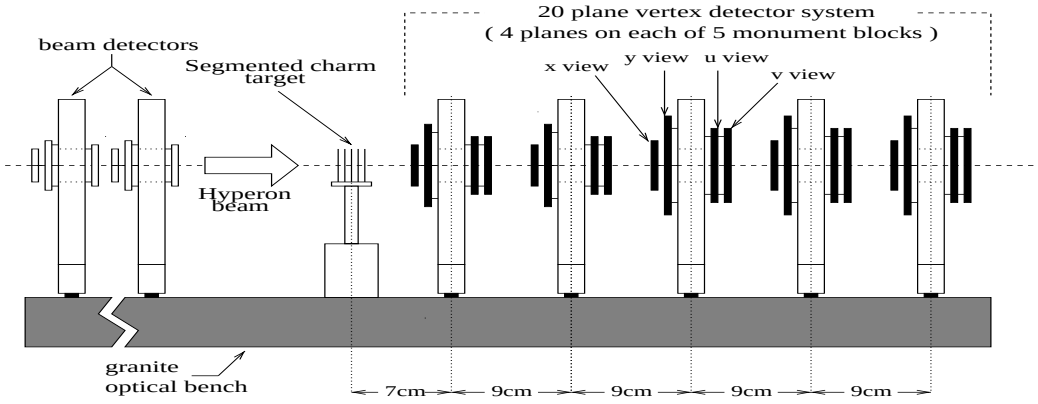

Figure 2.5: Beam and vertex silicon layout [61].

Five-cm type detectors read out every strip in the $3.1 \times 5.0\,\mathrm{cm}^2$ middle area of the detector, where the hit density is the largest. On the edges they have every-other strip readout, because the hit density is quite small there and only low energy tracks, which resolution is dominated by multiple scattering, can hit that region. Mosaic detectors were build out of three $8.3 \times 3.2\,\mathrm{cm}^2$ pieces of silicon. The detector in the middle has every strip readout, and the two edge detectors have every other strip readout.

Each of the detectors has greater than 98% hit detection efficiency and spatial resolution about 6.5 μm (Figure 2.6 [61]).

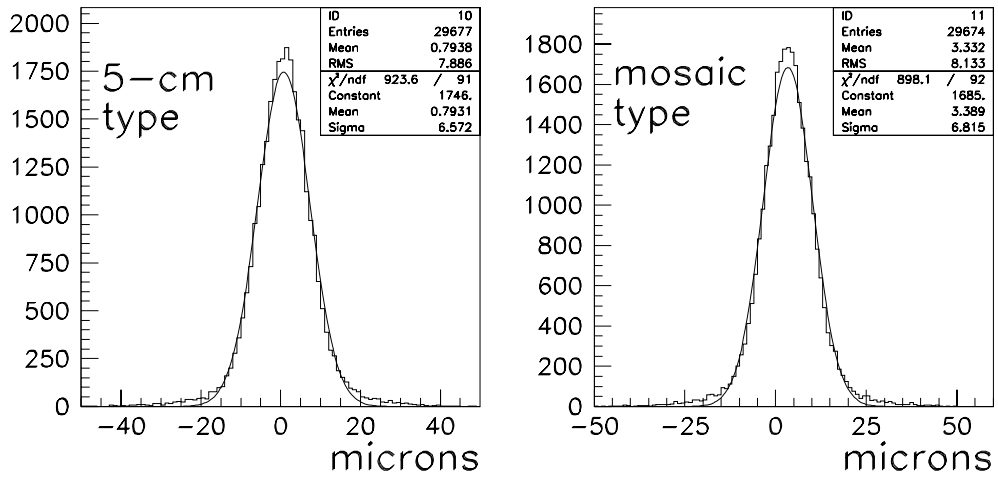

Figure 2.6: Typical resolutions of vertex detectors [61].

2.2.6 M1 spectrometer

.

Multiwire Proportional Chambers (MPWC) The M1 spectrometer had 3 chambers with 3 mm wire spacing and about $2 \times 2\,\mathrm{m}^2$ active area. Each chamber has 4 sensitive planes in 4 projections (Figure 2.7). Chambers have greater than 90% hit detection efficiency with 0.9 mm spatial resolution.

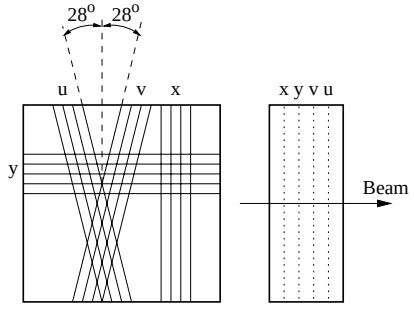

Figure 2.7: Schematic layout of M1 PWC chamber.

Drift chambers There were 2 drift chambers, each with 2 sensitive planes measuring hits in x projection. Chambers have $2.4 \times 1.7\,\mathrm{m}^2$ acceptance, they are about 80% efficient and has about 0.7 mm resolution [64].

Large Area Silicon Strip Detectors (LASD) There were 3 stations of Large Area Silicon Detectors located at the end plates of M1 and M2 magnets.

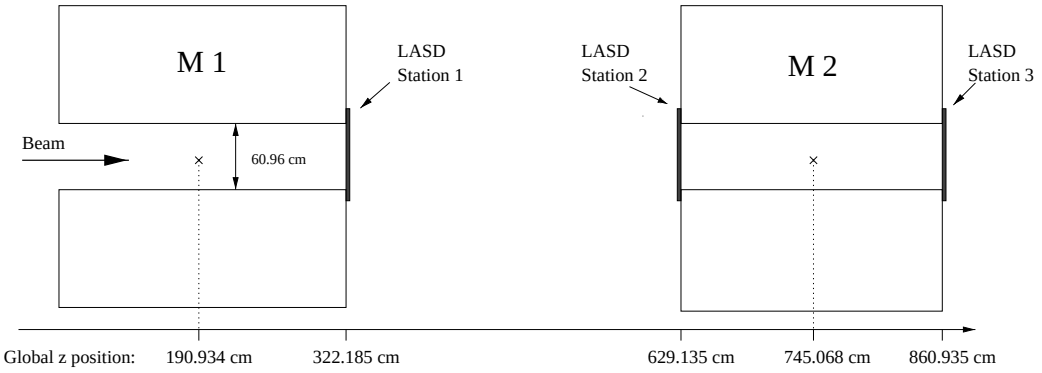

Figure 2.8: Location of the three LASD stations [65].

Each station had 2 planes of double-sided SSD with 50 μm strip pitch and $3.2 \times 2.6\text{cm}^2$ sensitive area. Double-sided SSD measured hits in x and y projections. 2 other planes were single-sided SSD with 50 μm strip pitch and $3.2 \times 3.2\text{cm}^2$ sensitive area. Single sided SSD measured hits in u and v projections. Detectors have 95-99% hit detection efficiency and the spatial resolution about 15 μm [53], [65].

Lead Glass Electromagnetic Calorimeters Three electromagnetic calorimeters were positioned at the end of M1, M2 and M3 spectrometers (Figure 2.1). Each calorimeter has hole in the middle to let beam and high energy particles through. Lead glass has density $4.1\,\text{g/cm}^3$ and radiation length 2.5 cm. The first 2 calorimeters were composed of blocks of 2 different sizes, smaller size blocks $4.25 \times 4.25 \times 34\,\text{cm}^3$ covering inside of the detector and bigger size blocks $8.5 \times 8.5 \times 34\,\text{cm}^3$ covering the outside of the detector [66]. The third calorimeter was built out of the same size blocks $3.8 \times 3.8 \times 45\,\text{cm}^3$ [67].

2.2.7 M2 spectrometer

.

Multiwire Proportional Chambers (PWC) There were 7 chambers with 2 mm wire spacing in the M2 spectrometer. The 3 upstream chambers

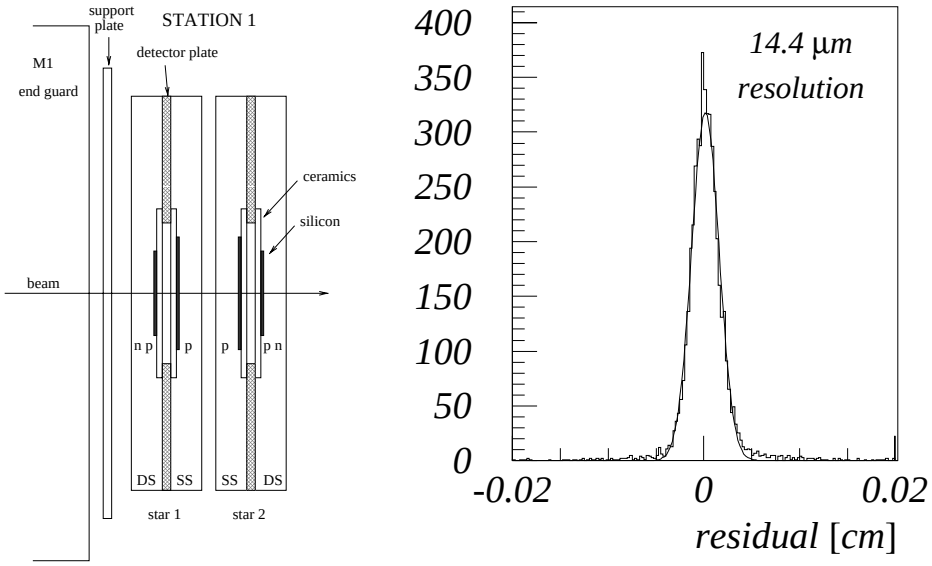

Figure 2.9: Layout and resolution of LASD. First figure shows schematic side-view of the LASD station with a sequence of a double sided, two single sided and another double sided detector. Second plot shows the resolution of the single sided detector [53]

have a $60 \times 60\,\mathrm{cm}^2$ aperture. The 4 downstream chambers have a $60 \times 100\,\mathrm{cm}^2$ aperture (Figure 2.10). Each chamber has 2 sensitive planes in 2 orthogonal projections. The chambers have greater than 95% hit detection efficiency with 0.6 mm spatial resolution [68].

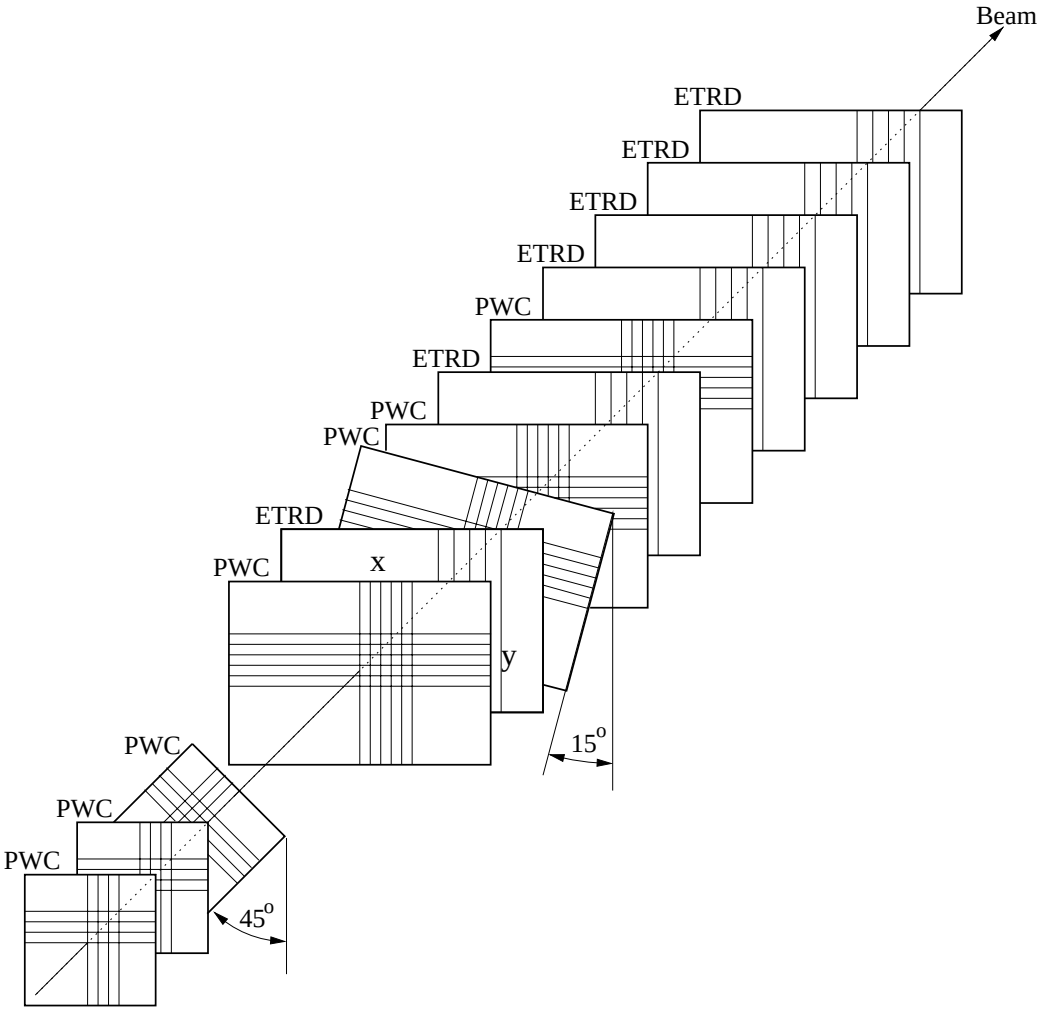

Figure 2.10: Schematic layout of M2 PWC chamber.

Electron Transition Radiation Detectors (ETRD) There were 6 electron TRDs in the M2 spectrometer whose primary purpose was to identify electrons. The transition radiation was generated in 200 polypropylene foils 17 μm thick positioned in front of each chamber. The radiation was detected

by $103 \times 63 \mathrm{cm}^2$ MPWC chambers with 4 mm wire spacing and filled with the mixture of Xe and methane [68]. The electrons have much higher γ-factor, then the same energy π, thus they have a larger number of clusters in TRD chambers, compared to π (Figure 2.11).

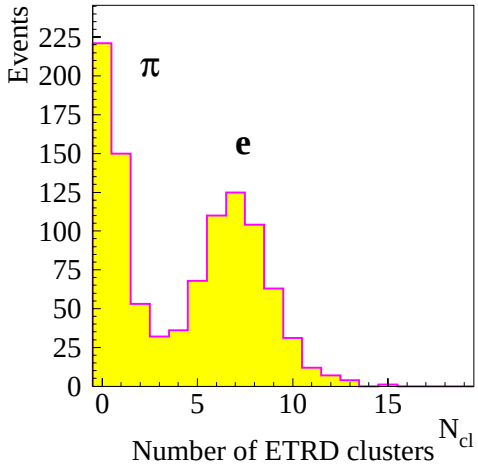

Figure 2.11: e/π separation using electron TRD

Ring Imaging Cherenkov Counter The RICH detector was the major particle identification device in the SELEX apparatus. Particles passed through 10 m long vessel filled with Ne gas emitting cherenkov light along the way (Figure 2.12). Cherenkov light was reflected on the spherical mirrors with 20 m curvature. Reflected light was focused on 2848 phototube array forming rings on it's surface.

The ring radius grows with the velocity of the particle (Figure 2.14). The $\beta = 1$ particle has a ring radius of 11.5 cm, with 13.6 hits on the ring. Each hit was measured with spatial resolution 5.5 mm, and ring radius r was measured with $\sigma_r = 1.8$ mm resolution in multi-track events, which allowed π/K separation up to $165\,GeV$ (Figure 2.13 [69]).

Vector drift chambers There were 9 Vector Drift Chambers (VDC) in SELEX experiment, united in 3 stations VeeA, VeeB, VeeC [70]. First 2 stations were located in in M2 spectrometer and the the third one in M3 spectrometer (Figure 2.1). Stations had $116 \times 116\,\mathrm{cm}^2$ aperture, about 90% efficiency and $\sim 100\mu$m resolution. The stations measured tracks in x, y, u or in x, y, v projections. Each chamber has 8 sensitive planes in the fine cells of the center region of the chamber. In the coarse cells it has 6 sensitive planes.

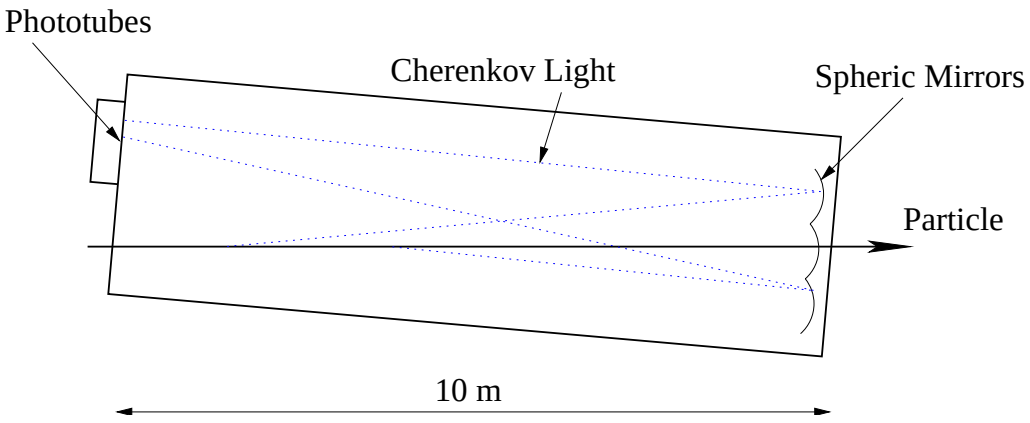

Figure 2.12: Schematic view of RICH detector.

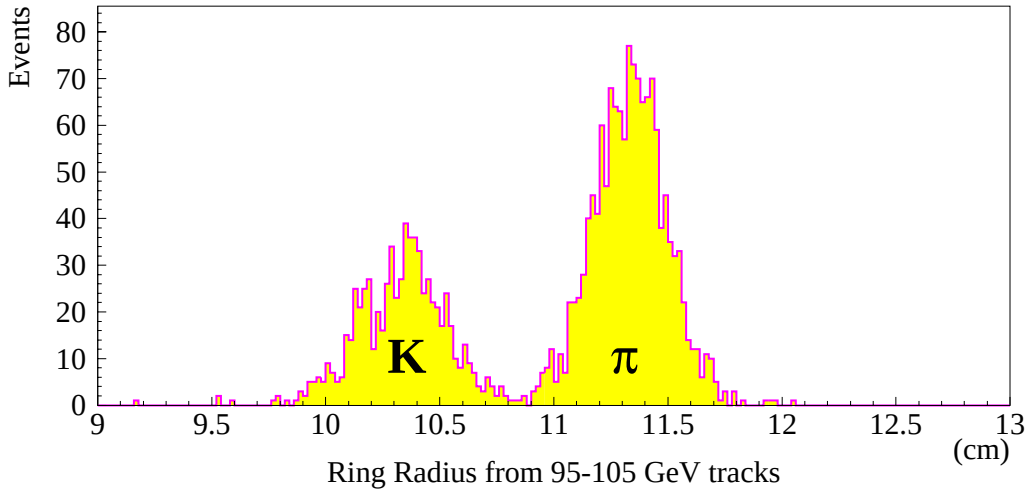

Figure 2.13: K/π separation at 95-105 GeV. [69].

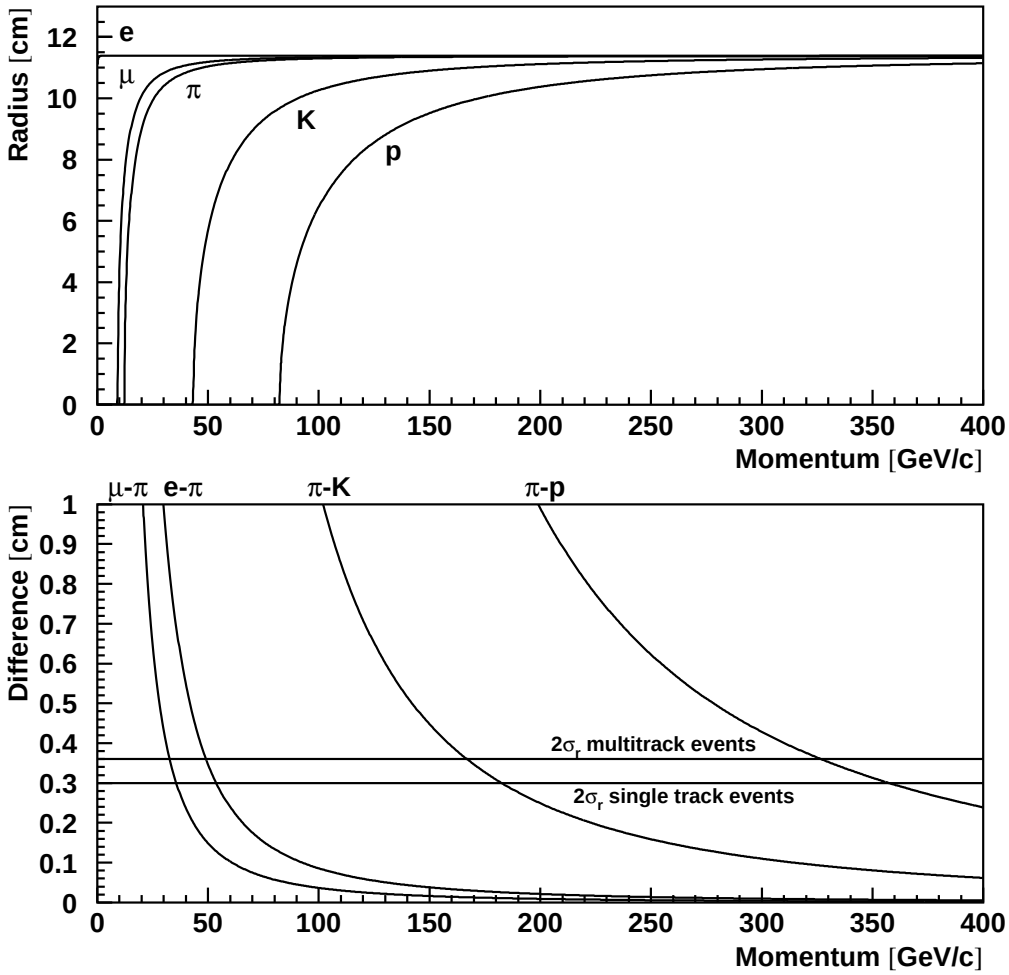

Figure 2.14: Ring radii (top) and separation (bottom) for different particles. The two horizontal lines on the lower plot show the achieved resolutions for the single track multiple tracks, respectively [69].

So each chamber measured a track at 6 or even 8 points and hence measured the track vector, not just its position.

2.3 Trigger and data acquisition system

One of the challenges of charm experiments is that apart from vertex displacement, events with charm particles do not have distinct kinematic features. The charm mass is not big enough to make an efficient trigger on events with large transverse momenta p_T, which is common in b-physics experiments. Most charm experiments use very loose triggers [71, 72], selecting just events with interactions. SELEX also used an open trigger requiring an interaction in the targets.

The trigger system in SELEX used a set of scintillation counters (S1-S4), veto counters (VH1,VH2), interaction counters (IC) and 2 hodoscopes (H1,H2) shown on Figure 2.15.

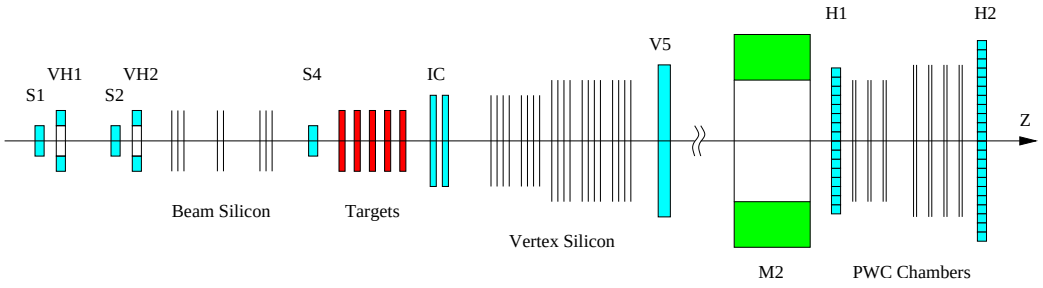

Figure 2.15: Schematic view of SELEX trigger elements

The interaction counters produced an output signal which amplitude was proportional to the number of particles that crossed them (Figure 2.16). The IC consisted of the two separate thin counters, and amplitude of the signal in each counter was measured. Using the smaller amplitude from the two counters for the particle multiplicity test greatly suppressed the effects of the Landau fluctuations of the amplitude in the individual counters [52].

The T0 trigger defined a beam particle as the coincidence of S1,S2,S4 counters with no hits in veto counters VH1 and VH2. Trigger T1 required an interaction in the targets, a signal from the Beam TRD and 2 hits in the positive region of the hodoscope H1 [73],[74]. An interaction in the targets was defined as the signal from the interaction counter IC larger than signal

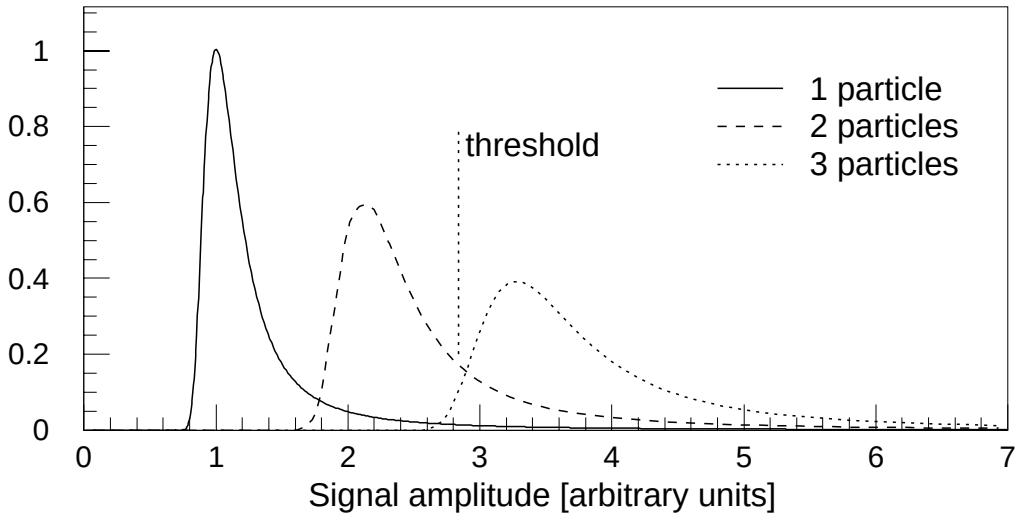

Figure 2.16: Simplified picture of multiplicity measurements in the interaction counters using the amplitude of the signal [52]. If the amplitude of the signal was greater than the threshold than multiplicity was considered to be greater than 3. The long tails of the amplitude spectra are due to the Landau fluctuation of the ionization losses. Combining information from the two counters greatly reduced the effect of the Landau fluctuations.

from 3 minimum ionizing particles. In early runs the signal from Beam TRD was not used, so that interactions from both π^- and Σ^- were accepted. In later runs the Beam TRD was used to trigger only on baryons (Σ^-, p).

Along with the charm trigger, there were other triggers which included a hadron-electron scattering trigger to measure electromagnetic radii of hadrons [52], an exotic trigger to study certain 3-prong events [75], and special calibration triggers to check apparatus performance.

If an event passed the trigger, it was digitized, packed and read out into dual-ported memories [74]. There were about 80000 events read out in each 20-second spill. They were processed in 40-second periods between spills by a 17-processor SGI Challenge computer by the SELEX Online Filter code. The Online Filter passed about 1 event in 8 (Section 2.3.1). These events were written out to disk. Events on disk were sampled by the monitoring program to check the apparatus performance during data-taking. Size of one event was about 6.5 kB. Events from disk were combined in 200 MB files, which were written to tapes and stored for the further processing. SELEX charm trigger rates are summarized in Table 2.3.

trigger/beam	definition	rate
proton beam	800 GeV protons from Tevatron	$4 \cdot 10^{10}$ Hz
Σ^-/π^- beam	600 GeV secondary beam	600 kHz
T0	$\mathrm{S1} \cdot \overline{\mathrm{VH1}} \cdot \mathrm{S2} \cdot \overline{\mathrm{VH2}} \cdot \mathrm{S4} \cdot \mathrm{V5}$	20 kHz
T1	$\mathrm{T0} \cdot (IC > 3) \cdot \mathrm{BTRD} \cdot (\mathrm{H1}, \mathrm{H2} > 2\,\mathrm{pos})$	4 kHz
Online filter	Event has more than just a primary vertex	500 Hz

Table 2.3: SELEX charm trigger rates

The schematic diagram of the SELEX trigger and DAQ is shown in Figure 2.17.

2.3.1 Online Filter

One of the innovations of the SELEX experiment was the online filter. This is a program which ran between the beam spills and processed data to reject events that did not have evidence for a secondary vertex.

First the filter program reconstructed tracks in the downstream PWC system. Only tracks with momenta greater above 15 GeV/c could make it

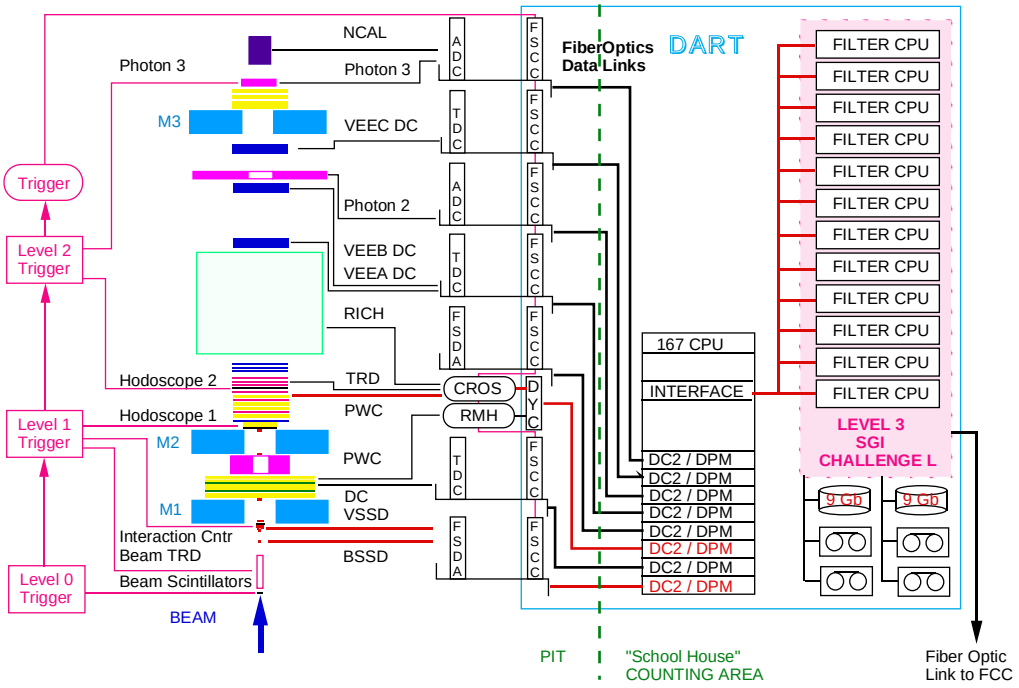

Figure 2.17: Schematic view of SELEX Trigger and DAQ systems

through the magnets to reach these chambers. After that a beam track was reconstructed. Tracks from the downstream PWC were extrapolated back to the vertex silicon, using beam track information as a guidance to the approximate primary vertex location. A special fast reconstruction program searched for track segments in the vertex silicon, using downstream track extrapolations as an initial starting parameters and looking for hits in searching windows around them. The sizes of searching windows were calculated based on the resolutions of the detectors and the effects of multiple scattering. Because only relatively large momentum tracks ($> 15\,\mathrm{GeV}$) were extrapolated back to the vertex silicon multiple scattering errors were kept under control. The beam track and tracks reconstructed in the vertex silicon and downstream chambers were fitted to a primary vertex. If the fit had an acceptable χ^2 and used all tracks, the event was rejected as non-charm. On the other hand if one or more tracks did not point to the common vertex, the event was kept.

Special studies showed that the online filter program was approximately equivalent to the cut $L/\sigma_L > 3$, where L is the distance between the primary and the secondary vertex. The Online Filter decreased the background by a factor of 8 and was about 50% efficient for a typical charm signal. So experiment benefited by decreasing the time to process the tapes by a factor of 8 at the cost of modest sacrifice in charm signal. It took us about half a year to process all the tapes, so the factor of 8 played an important role in expediting the path to the physics results.

2.4 SELEX data taking and charm data sets

SELEX started to take data in July 1996. The first runs were taken to verify the trigger, to check apparatus, to establish chamber efficiencies, to calibrate photon detectors, to optimize online filter and to perform similar tasks dedicated to establish a high quality of the data written to tape. Data written to tape since February 1997 was used in the final charm analysis. The first set of these data did not use signal from Beam TRD, so interactions from both π^- and Σ^- were written to tape. The second part used the Beam TRD response in the T1 trigger (Section 2.3) and mostly Σ^- interactions were written to the tape. In the third part polarity of the hyperon beam was reversed, which provided beam composed of mostly protons (Figure 2.18). Overall, the experiment took data for almost year and a half.

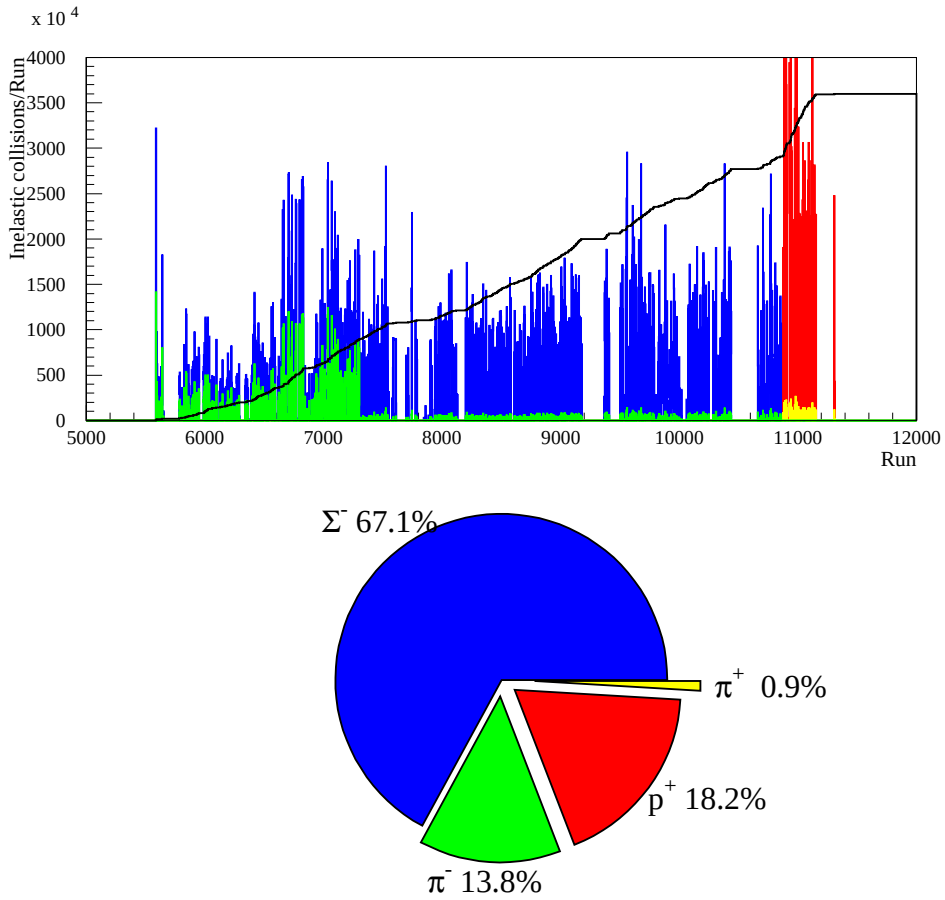

Figure 2.18: SELEX data sets

Special alignment runs were taken every day to verify the geometrical positions of silicon detectors and downstream PWC chambers. The detector performance and the Online Filter were constantly monitored. Also special runs were taken to study π^-, Σ^- and p total cross sections [76], [50].

2.4.1 Improving Detector performance

SELEX was a new detector and a lot of effort went into making it work properly. One of the problems was in the online filter. When the code was written its performance was tested on Monte-Carlo (MC) events. The code was efficient and fast enough on MC simulations. When the apparatus was turned on, the number of hits in the downstream M2 PWC chambers was twice as big as in the MC case. The code was still capable of reconstructing those events with about the same efficiency, but it did it too slowly. The speed of the code was proportional to $n_{hit}^{3.5}$, where n_{hit} was the number of hits in the PWC chambers. Twice as many hits required about 10 times more computing power to process those high-multiplicity events in the available time window. At first we just threw out 50% of events with high-multiplicity in the M2 PWC chambers, to allow the online filter to process remaining 50% in time. But it was fairly large chunk of data to lose. A lot of effort went into improvement of the Online Filter: fast searching algorithms were implemented, code was timed and optimized. This gave a factor of 2 improvement in speed: good, but not enough. Significant improvement came from my physics study that pointed out characteristics of the tracks we wanted to find first, which gave about a factor of 4 speed improvement.

Along with the Online Filter optimization, there were also many improvements in the apparatus. Noise levels were reduced, trigger and DAQ were modified to read out events faster. By the last half of data-taking the yield of reconstructed charm events per billion interactions was three times higher than the yield at the beginning of data taking.

Chapter 3

Measurement procedure

After applying selection cuts we ended up with a small sample of about 30000 events, which included about 10210 D^0 and 1630 Λ_c^+ events along with a large number of background events. Large sample of background events was used to extract background properties. In this chapter we are going to discuss how the D^0 and Λ_c^+ lifetimes were extracted from that sample.

3.1 Lifetime Fitting Technique

If the data had no background and were measured with the infinite precision in an apparatus with uniform acceptance, then extracting lifetime would be exceedingly simple. One would simply book a histogram of proper decay times t for events in such a sample, where the proper decay time t is:

$$t = \frac{L}{c\gamma\beta} \approx \frac{L \cdot M_c}{c \cdot p_z} \tag{3.1}$$

Here L is the distance the charm particle traveled in the laboratory system, c is the speed of light, $\gamma\beta$ are Lorentz factors, M_c is the mass of a charm particle, and p_z is the momentum of the charm particle along the apparatus. Then the number of events in each histogram bin $n(t)$ is fitted with an exponential function:

$$n(t) \propto e^{-t/\tau}, \tag{3.2}$$

where τ is the lifetime we are looking for. We assume the bin width Δt is small compared to the lifetime τ.

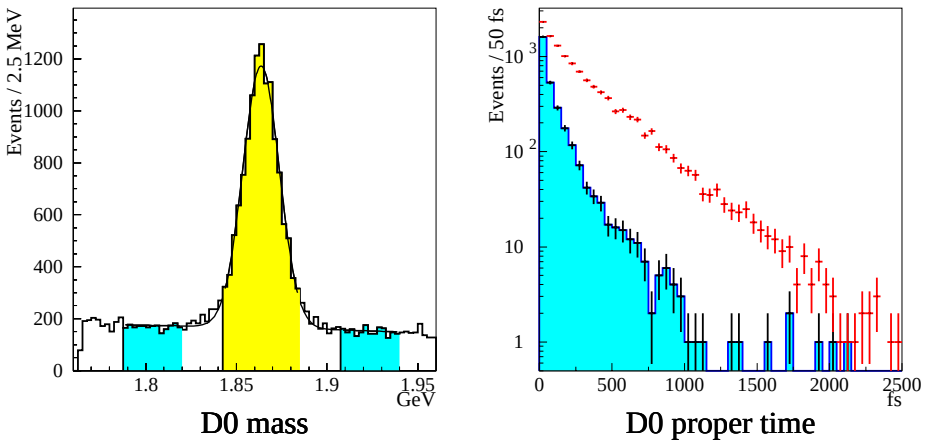

Figure 3.1: Illustration of proper time distributions for signal and sideband regions. Left plot shows the reconstructed mass. Shaded regions on this plot correspond to signal and background. The proper time distribution of the events from the signal region is shown with data points on the right plot. The proper time distribution of the background events is shown with the shaded histogram on the right plot.

For the real experimental data we applied the same technique, making a histogram of proper times $n(t)$ (Figure 3.1), but it deviated from a simple exponential form $e^{-t/\tau}$ due to three main effects:

- Presence of background
- Acceptance correction for signal events
- Resolution smearing

The following sections describe how these effects were taken into account in the fitting procedure of the overall proper time distribution $n(t)$.

3.1.1 Background fitting

Background was taken into account by studying events from the mass sidebands which contain only background events. We assumed that properties of background events inside the signal region were the same as in the sidebands. We verified that the last assumption was true by choosing different sidebands (Section 4.4).

Often one would use the so-called "sideband subtraction" method based on the observed proper time distributions in the signal region $N_s(t)$ and in the background regions $N_b(t)$. For each proper time bin t the number of events in the background region $N_b(t)$ is given by:

$$N_b(t) = B_{left}(t) + B_{right}(t) \equiv B(t), \tag{3.3}$$

where B_{left} and B_{right} are the number of events from left and right sideband respectively.

Events in the signal region have both signal and background events. Common case is when the number of background events changes linearly as a function of mass. In this approximation the number of events in the signal region $N_s(t)$ is given by:

$$N_s(t) = S(t) + C \cdot B(t), \tag{3.4}$$

where $S(t)$ is the number of signal events and $C \cdot B(t)$ is the number of background events. Coefficient C depends on widths of signal (w_s) and sideband regions (w_{left}, w_{right}):

$$C = \frac{w_s}{w_{left} + w_{right}}, \tag{3.5}$$

Then the number of signal events is given by

$$S(t) = N_s(t) - C \cdot N_b(t) \propto e^{-t/\tau}. \tag{3.6}$$

To summarize: in this method the number of signal events $S(t)$ is extracted by statistically subtracting background contribution $N_b(t)$ from $N_s(t)$. After that one can fit $S(t)$ with an exponential $e^{-t/\tau}$ form.

This is a very useful procedure, but unfortunately it has problems when one deals with sparsely-populated bins. Both $N_s(t)$ and $N_b(t)$ have Poisson-distributed number of events in the bin. On the other hand $S(t)$ is the linear combination of both, and the number of events for $S(t)$ is no longer Poisson-distributed. For example after the statistical subtraction (Eq. 3.6) $S(t)$ can have negative number of entries in some bin, because of the statistical fluctuation. This is clearly forbidden in Poisson distribution. So to fit $S(t)$ one can use neither Poisson errors for log-likelihood fitting technique, nor Gaussian errors for χ^2-fitting, as Gaussian approximation is true only when both $N_s(t)$ and $N_b(t)$ are large.

To calculate the mean value and errors correctly, it is necessary to fit simultaneously $N_s(t)$ and $N_b(t)$ rather than to fit the sideband subtracted signal $S(t)$. However the problem with this technique is that one must assume some shape for the distribution of background events $N_b(t)$, for which one has no a priori knowledge. Usually one uses a smooth function which describes the background distribution reasonably well.

3.1.2 Acceptance correction

This problem has a very straightforward approach. The number of signal events $S(t)$ is given by the lifetime decay curve $e^{-t/\tau}$ and the acceptance correction (or in other words overall efficiency) $\epsilon(t)$, so that

$$S(t) = \epsilon(t) \cdot e^{-t/\tau}. \tag{3.7}$$

One can, of course, fit $S(t)/\epsilon(t)$ with an exponential distribution, but it has the same disadvantage as the sideband subtraction procedure - the number of events $S(t)$ is no longer Poisson-distributed. So, it's much better to fit the product $\epsilon(t) \cdot e^{-t/\tau}$

3.1.3 Resolution smearing

The finite resolution of the detector leads to three consequences:

- The measured proper time will deviate from its actual value. An event can migrate from the proper time bin to which it belongs into some neighboring bin. For this experiment the proper time resolution $\sigma_t \approx$ 15 fs, which was much smaller than even the Λ_c^+ lifetime ($\tau \approx 200$ fs). Because the lifetime is an average proper time of different events, the resolution error will lead to an error in the lifetime measurement of order $\sigma_\tau \approx \sigma_t/\sqrt{N}$, where N is the number of events in the sample. For Λ_c^+ this error is about 0.4 fs and for D^0 about 0.15 fs, which is negligible compared to the lifetime statistical errors ~ 6 fs.

- Some events will be smeared into an area forbidden by the cuts. For example, let's consider the $L/\sigma > 8$ cut: an event with $L/\sigma = 8.2$ may be measured as an event with $L/\sigma = 7.8$ and be thrown out of the sample. On the other hand there are events with $L/\sigma = 7.8$ which will be measured as $L/\sigma = 8.2$ and thus compensate for the loss. As

there are more events with $L/\sigma = 7.8$ than events with $L/\sigma = 8.2$ some imbalance will occur. We included this mechanism in our analysis by simulating resolution smearing. It can not dominate our error, because of good resolution. It is very similar to resolution smearing, which we just discussed. It produces migration of events between proper time bins and introduces uncertainty of the same scale as resolution smearing.

- Some events can be irrevocably lost. For example if a 4-prong secondary vertex lies just outside a target, then almost inevitably some pair of tracks will form a vertex inside target which triggers the mechanism of secondary interactions suppression (Section 3.3.3). The event will be thrown out of the sample. Clearly, events just inside the target will not compensate for the loss, as they will be thrown out of the sample by the same mechanism (Figure 3.6). Again, we simulate the resolution smearing to account for this effect.

3.1.4 Final choice of fitting function

We have chosen to make a simultaneous fit for signal and background to extract the lifetime. The proper time distribution for the events in the signal region $N_s(t)$ and sidebands $N_b(t)$ were fitted using

$$N_s(t) = S(t) + C \cdot B(t) = \frac{N_0}{\tau} e^{-t/\tau} \cdot \epsilon(t) + C \cdot B(t) \tag{3.8}$$

$$N_b(t) = B(t) = \frac{N_1}{\tau_1} e^{-t/\tau_1} + \frac{N_2}{\tau_2} e^{-t/\tau_2} \tag{3.9}$$

where $\epsilon(t)$ is the efficiency for signal events, and C is the relative fraction of background under the signal peak, which depends on the width of the signal and background regions (3.5). The background $B(t)$ was fitted as a sum of 2 exponents, which describes background reasonably well. There were six free parameters in the fit:

- N_0 - number of signal events
- τ - signal lifetime
- N_1, N_2 - number of background events
- τ_1, τ_2 - lifetime of background

Both $N_s(t)$ and $N_b(t)$ have Poisson distributions, thus log-likelihood minimization was chosen in the fit.

3.2 Efficiency calculations

In this section we discuss method that we used to find the efficiency of apparatus $\epsilon(t)$ for the sample of observed events.

3.2.1 Formulation of the problem

Consider a set of observed charm events $n(\vec{p})$, which are completely described by decay physical parameters $\vec{p}$. For example $\vec{p} = (\vec{p_c}, \vec{p_i} \ldots)$ may include the momentum of the charm particle and its decay products, the target where the charm particle was produced, and other parameters that describe the decay. Let's assume that for the event described by decay parameter $\vec{p}$ the efficiency of the apparatus as a function of proper time t is $\epsilon(\vec{p}, t)$. Efficiency of the apparatus is defined by a set of explicit cuts, losses in the targets and efficiency of the offline reconstruction program, which are discussed in detail in Section 3.3. Our task is to find $n(t)$, the expected number of events at proper time t for the observed sample $n(\vec{p})$.

For a subsample of events described by parameter $\vec{p}$ the expected proper time distribution $n(\vec{p}, t)$ is given by

$$n(\vec{p}, t) = n_0(\vec{p}, t) \times \epsilon(\vec{p}, t), \tag{3.10}$$

where $n_0(\vec{p}, t)$ is the proper time distribution of events described by parameter $\vec{p}$ in an apparatus of 100% efficiency . Throughout this section we are going to use subscript 0 to indicate a sample before the efficiency of apparatus is applied i.e., what we would observe if the apparatus were 100% efficient.

Since the proper time t of particle decay is independent of any other physical properties of event, then the expected proper time distribution $n_0(\vec{p}, t)$ is given by

$$n_0(\vec{p}, t) = n_0(\vec{p}) \cdot \frac{1}{\tau} e^{-t/\tau}, \tag{3.11}$$

where $n_0(\vec{p})$ is the number of events described by parameter $\vec{p}$.

The proper time distribution $n_0(t)$ of all events $n_0(\vec{p})$ is given by

$$n_0(t) = \int n_0(\vec{p}, t)\, d\vec{p} = \frac{1}{\tau} e^{-t/\tau} \times \int n_0(\vec{p})\, d\vec{p}, \tag{3.12}$$

which is quite obvious without any derivation at all. The integral $\int n_0(\vec{p})\, d\vec{p}$ is just a constant equal to the total number of events.

The observed proper time distribution $n(t)$ in the apparatus with the efficiency $\epsilon(\vec{p}, t)$ is:

$$n(t) = \int n(\vec{p}, t)\, d\vec{p} = \frac{1}{\tau} e^{-t/\tau} \times \int \epsilon(\vec{p}, t) \cdot n_0(\vec{p}) \cdot\, d\vec{p} = \frac{1}{\tau} e^{-t/\tau} \cdot \epsilon(t), \quad (3.13)$$

where overall efficiency $\epsilon(t)$ for the sample $n_0(\vec{p})$ is given by:

$$\epsilon(t) = \int \epsilon(\vec{p}, t) \cdot n_0(\vec{p}) \cdot\, d\vec{p} \quad (3.14)$$

3.2.2 Disadvantages of conventional Monte-Carlo.

To calculate efficiency according to Eq. 3.14 one has to know both $n_0(\vec{p})$ and $\epsilon(\vec{p}, t)$. Both functions are rather complicated and have many variables that describe them. Also there can be correlations between variables. All these reasons make construction of these functions rather complex.

In the conventional Monte-Carlo technique one calculates the apparatus efficiency $\epsilon(\vec{p}, t)$ using a Monte-Carlo simulation and generates the original distribution $n_0(\vec{p})$ using some event generator. However, charm hadroproduction is not cleanly described theoretically, so $n_0(\vec{p})$ cannot be simulated exactly. Simulation of $n_0(\vec{p})$ is usually based on some phenomenological model. To verify the simulated distribution $n_0(\vec{p})$ one compares $n_0(\vec{p}) \cdot \epsilon(\vec{p})$ with the observed distribution $n(\vec{p})$. But if there is a discrepancy it is not always clear if the discrepancy is due to simulation of apparatus $\epsilon(\vec{p}, t)$ or due to the simulation of the production spectra $n_0(\vec{p})$.

So the main disadvantage of the conventional Monte-Carlo is that it requires knowledge of the production spectra $n_0(\vec{p})$, which is not the primary goal in the lifetime study. On the other hand if $n_0(\vec{p})$ is established with sufficient precision it can be used in the lifetime study and also in many other studies.

3.2.3 Another way to calculate the overall efficiency

In this analysis we want to take out uncertainty in $n_0(\vec{p})$. Indeed it seems strange that simulation of the efficiency of apparatus $\epsilon(\vec{p}, t)$ is not enough, that we also need to know $n_0(\vec{p})$. Imagine that we have a subsample $n(\vec{p}, t)$ in

a very small phase space of $\vec{p}$. If we calculate the efficiency $\epsilon(\vec{p},t)$ correctly, then:

$$\frac{n(\vec{p},t)}{\epsilon(\vec{p},t)} = n_0(\vec{p},t) \propto e^{-t/\tau}. \tag{3.15}$$

Thus for individual subsamples we actually need to know nothing at all about $n_0(\vec{p})$ to extract the lifetime τ. This $n_0(\vec{p})$ problem arises only when we put all the data subsamples together.

To relate $n(\vec{p})$ to $n_0(\vec{p})$ we construct the weight $w(\vec{p})$ for each event:

$$w(\vec{p})^{-1} = \int \epsilon(\vec{p},t) \times \frac{1}{\tau} e^{-t/\tau} dt, \tag{3.16}$$

Then indeed the number of events $n(\vec{p})$ described by parameter $\vec{p}$ is related to original number of events $n_0(\vec{p})$ by:

$$\begin{aligned} n(\vec{p}) &= \int n(\vec{p},t) \cdot dt = \int n_0(\vec{p}) \cdot \frac{1}{\tau} e^{-t/\tau} \cdot \epsilon(\vec{p},t)\, dt \\ &= n_0(\vec{p}) \cdot w^{-1}(\vec{p}), \end{aligned} \tag{3.17}$$

or

$$n_0(\vec{p}) = n(\vec{p}) \cdot w(\vec{p}). \tag{3.18}$$

If we substitute Eq.3.18 into Eq.3.13 we get:

$$n(t) = \frac{1}{\tau} e^{-t/\tau} \times \int \epsilon(\vec{p},t) \cdot n(\vec{p}) \cdot w(\vec{p})\, d\vec{p} \tag{3.19}$$

and finally overall efficiency $\epsilon(t)$

$$\epsilon(t) = \frac{n(t)}{n_0(t)} = \frac{\int \epsilon(\vec{p},t) \cdot n(\vec{p}) \cdot w(\vec{p})\, d\vec{p}}{\int n(\vec{p}) \cdot w(\vec{p})\, d\vec{p}}, \tag{3.20}$$

And we reached the goal: overall efficiency does not depend on $n_0(\vec{p})$. The formula in Eq. 3.20 basically says that the overall efficiency $\epsilon(t)$ is the weighted average of the individual event efficiencies $\epsilon(\vec{p},t)$.

3.2.4 Cancellation of the downstream efficiency

Calculation of the individual event efficiency $\epsilon(\vec{p},t)$ is quite complicated. Because charm particle live only few centimeters in our apparatus, one can factorize $\epsilon(\vec{p},t)$ into the efficiency of "vertex region", which is a function of t, and the "downstream" efficiency, which is independent of proper time t. Formally we write:

$$\epsilon(\vec{p},t) = \epsilon_{down}(\vec{p}) \cdot \epsilon_{vtx}(\vec{p},t) \tag{3.21}$$

The downstream efficiency is not a function of t, because the chance that the downstream system will reconstruct the tracks from a charm particle that decayed after 2cm of flight are the same as for a charm particle that decayed after 1cm of flight. Conversely t is quite important for reconstruction in the vertex region. Then

$$w(\vec{p})^{-1} = \epsilon_{down}(\vec{p}) \int \epsilon_{vtx}(\vec{p},t) \cdot \frac{1}{\tau} e^{-t/\tau} dt = w_{vtx}(\vec{p})^{-1} \cdot \epsilon_{down}(\vec{p}), \tag{3.22}$$

Now if we use Eq.3.21 and Eq.3.22 in calculations for overall efficiency $\epsilon(t)$ in Eq.3.20, then

$$\epsilon(t) = \frac{\int n(\vec{p}) \cdot \epsilon_{vtx}(\vec{p},t) \epsilon_{down}(\vec{p}) \cdot w_{vtx}(\vec{p}) / \epsilon_{down}(\vec{p})\, d\vec{p}}{\int n(\vec{p}) \cdot w(\vec{p})\, d\vec{p}} \tag{3.23}$$

$$= \frac{\int \epsilon_{vtx}(\vec{p},t) \cdot n(\vec{p}) \cdot w_{vtx}(\vec{p})\, d\vec{p}}{\int n(\vec{p}) \cdot w_{vtx}(\vec{p})\, d\vec{p}}, \tag{3.24}$$

$\epsilon_{down}(\vec{p})$ canceled out in the numerator. In the denominator $w(\vec{p})$ was replaced with $w_{vtx}(\vec{p})$, since this integral is not a function of proper time t, but just a number for the normalization.

Cancellation of the downstream efficiency is quite helpful in this analysis, because we did not need to simulate reconstruction efficiency of the downstream chambers or the RICH detector.

3.2.5 Reduced proper time

In fixed target experiments a cut on the vertex separation significance L/σ_L is almost mandatory because of the high levels of background. For the sake of simplicity let's assume that it is the only cut we are dealing with. Consider a subsample of $D^0 \to K^-\pi^+$ decays, with fixed decay configuration $\vec{p}$, so that

the momenta of the D^0, K^-, π^+ are fixed, as well as all angles between tracks. Then a cut $L/\sigma > N$ will suppress all events with proper time t smaller than minimum proper time t_{min} defined by

$$t_{min} \simeq \frac{N\sigma}{\gamma \cdot c} \tag{3.25}$$

where γ is the relativistic γ factor of the D^0 particle. We will discuss a more precise way to calculate t_{min} later. The important thing is that the subsample has an exponential distribution for $t > t_{min}$. We can split the whole sample into subsamples, each having its own minimum proper time $t_{min}(\vec{p})$. All those distributions are exponential for $t > t_{min}(\vec{p})$. Summing up all distributions measuring time from $t = t_{min}(\vec{p})$ would produce an exponential distribution with the same lifetime τ. Hence we can histogram the reduced proper time $t_r = t - t_{min}(\vec{p})$, instead of the proper time t and still get back an exponential distribution with the same lifetime.

Why use reduced proper time? In illustrative Fig.3.2 subsamples with different t_{min} are shown on the upper left plot. Because of the resolution smearing the $L/\sigma > N$ cut will not be a sharp vertical line. In the shaded region one needs to know details of measurement errors to calculate the exact shape of the proper time distribution. It is usually quite difficult to find this shape because non-Gaussian errors are always present in the data and are usually missed in simulation. So if one just histograms proper time, then after summing all these subsamples one would get the distribution shown in the bottom left corner. The "uncertain" shaded region is quite large, and hence the acceptance correction is big. On the other hand if one histograms reduced proper time t_r he gets a much smaller "uncertain" region, and acceptance corrections will be small in most regions of the distribution.

We prefer the reduced proper time technique. However if one knows the efficiency for all subsamples exactly, both methods will give the same answer.

3.2.6 Modifications in efficiency calculations

The change of variables $t \to t_r = t - t_{min}(\vec{p})$ leads to small changes in efficiency calculations. Calculations are very straightforward, keeping in mind that new "reduced proper time" distributions relate to ordinary "proper time" distributions by the following relations:

$$n_{0r}(\vec{p}, t_r) \quad = \quad n_0(\vec{p}, t_r + t_{min}(\vec{p})) \tag{3.26}$$

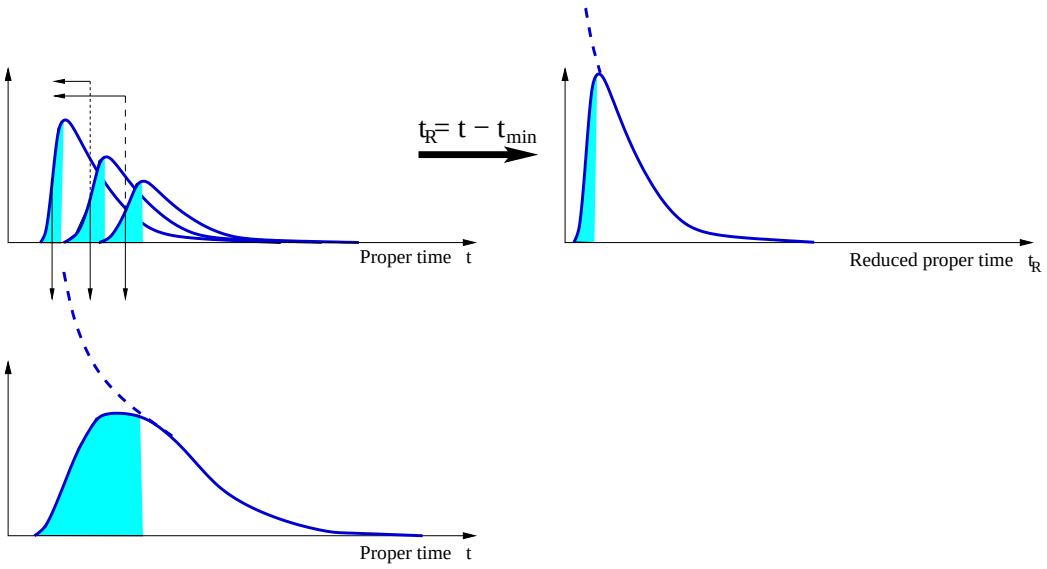

Figure 3.2: Why choose reduced proper time? To make smaller shaded "uncertain region".

$$n_r(\vec{p}, t_r) = n(\vec{p}, t_r + t_{min}(\vec{p})) \quad (3.27)$$

$$\epsilon_r(\vec{p}, t_r) = \epsilon(\vec{p}, t_r + t_{min}(\vec{p})) \quad (3.28)$$

Applying these rules one arrives at the following result for reduced proper time efficiency:

$$\epsilon_r(t_r) = \frac{n_r(t_r)}{n_{0r}(t_r)} = \frac{\int \epsilon_r(\vec{p}, t_r) \cdot n(\vec{p}) e^{-t_{min}(\vec{p})/\tau} \cdot w(\vec{p})\, d\vec{p}}{\int n(\vec{p}) e^{-t_{min}(\vec{p})/\tau} \cdot w(\vec{p})\, d\vec{p}}, \quad (3.29)$$

where weights $w(\vec{p})$ are calculated in the same way using Eq.3.16. The result is very similar to Eq.3.14; the product $n(\vec{p})e^{-t_{min}(\vec{p})/\tau}$ is just the original number of events $n_0(\vec{p}, t_r)$ at $t_r = 0$.

3.3 The individual event efficiency

In this section we discuss how we computed the individual event efficiency $\epsilon(\vec{p}, t)$, which is a critical input in the overall efficiency function $\epsilon(t)$ given by Eq.3.20. To calculate an individual event efficiency one has to take the event and keeping all the physical decay parameters $\vec{p}$ constant vary t, i.e., move

the event along the apparatus and see how the efficiency varies. Explicit cuts ($L/\sigma > 8$, $z_{sec} < 2.3$ cm, etc), losses in the targets and offline code reconstruction efficiency affect the individual event efficiency $\epsilon(\vec{p}, t)$. In the next two sections we list and discuss these cuts. A sketch of an individual event efficiency is shown in Figure 3.3.

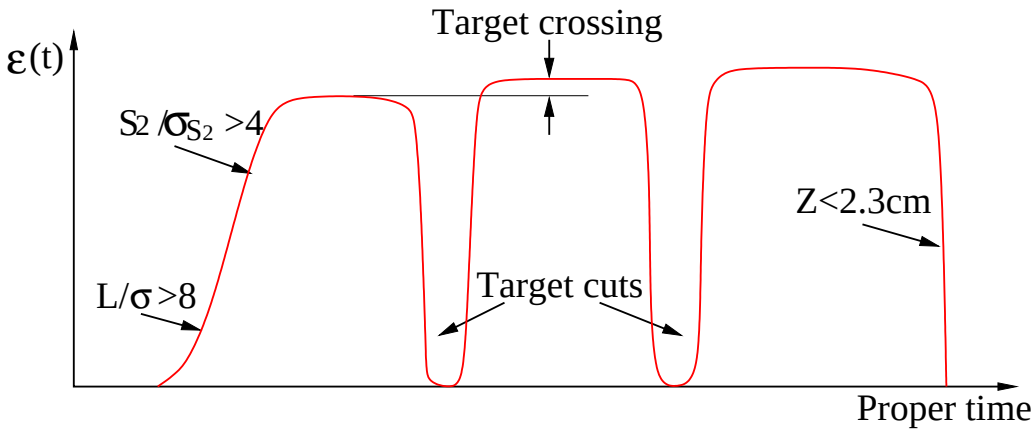

Figure 3.3: Sketch of an individual event efficiency

3.3.1 Explicit cuts

Signals for D^0 and Λ_c^+ are large, and each individual measurement is quite precise. For our measurements it was important to keep cuts simple, because generally it's easier to simulate simple cuts than complicated ones.

Vertex separation cut $L/\sigma_L > 8$

L is the distance between primary and secondary vertices. As all the angles are very small ($\sim$ 10 mrad) then $L = z_{sec} - z_{prim}$ is an excellent approximation. The secondary vertex position is defined by the fit of the secondary vertex tracks to the common vertex. The primary vertex is defined by the fit of the tracks from the primary vertex z_{vtx}, but we also know that the primary interaction has to happen in a target whose position z_{tgt} is known. To incorporate this additional information we calculated the primary vertex z_{prim} as the weighted average of vertex position z_{vtx} and target position z_{tgt}:

$$z_{prim} = \frac{w_{vtx} z_{vtx} + w_{tygt} z_{tgt}}{w_{vtx} + w_{tgt}}, \tag{3.30}$$

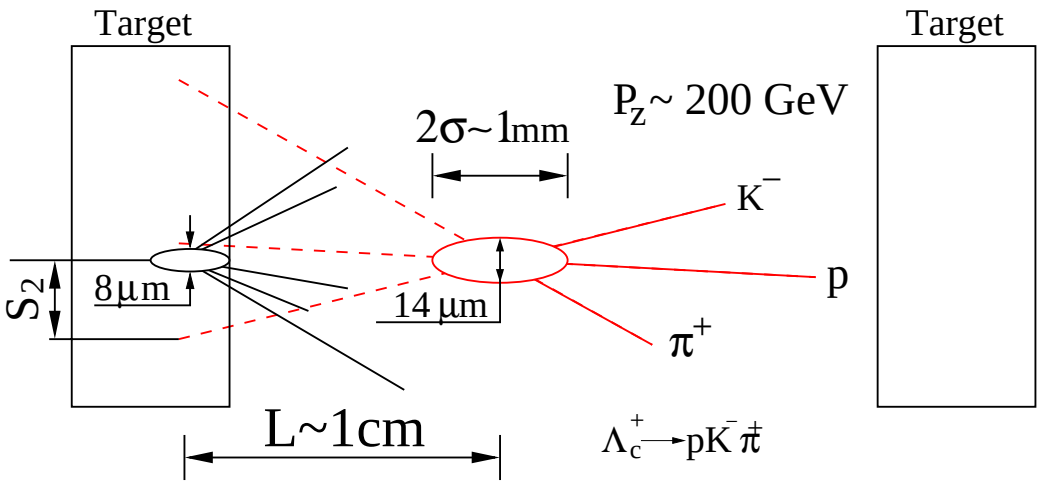

Figure 3.4: Illustration of explicit cuts applied to select charm sample events

where $w_{vtx} = 1/\sigma_{vtx}^2$ is the weight of primary vertex fit, and $w_{tgt} = 12/H_{tgt}^2$, where H_{tgt} is the thickness of the target.

Calculation of σ_L is very straightforward:

$$\sigma_L = \sqrt{\sigma_{prim}^2 + \sigma_{sec}^2} \tag{3.31}$$

One should keep in mind that σ_{sec} depends on the proper time t of the decay: the larger t, the closer we get to the silicon detector, and the smaller σ_{sec} gets.

Second largest miss-distance significance $s_2/\sigma_{s_2} > 4$

The miss-distance of secondary tracks was calculated by extrapolating them back to the primary vertex location z_{prim}. The miss-distance s is the distance between the primary vertex and the secondary trajectory at $z = z_{prim}$. s_2 is the second largest miss-distance, and σ_{s_2} is the extrapolated error, calculated using the track error matrix. This cut suppresses background generated when tracks from a secondary interaction cross tracks from the primary vertex (Fig. 3.5).

Charm track points back to primary vertex $P_{vtx} < 12$

The charm track was constructed as the vector sum of its secondary tracks. This track was extrapolated back to the primary vertex z_{prim} and the miss-

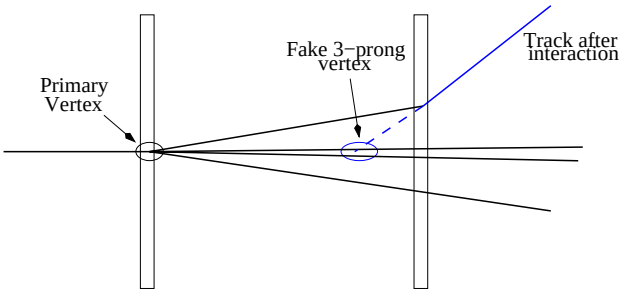

Figure 3.5: Backgrounds suppressed by s_2 cut

distance with respect to the primary vertex was calculated. The pointback value P_{vtx} is this miss-distance divided by its error.

No escape into silicon $z_{sec} < 2.3$ cm

Some charm events lived long enough to get into the silicon detector region. The apparatus was still capable of reconstructing charm events in that area, but the efficiency slowly degraded in that region. The degradation was not easy to simulate adequately, so we decided to use only events with $z_{sec} <$ 2.3 cm where efficiency simulation was simpler.

Distance to the closest target $\Delta\ z_{tgt} > 500\mu m$

Most of the events in the experiment were certainly not charm, but rather secondary interactions in the targets, where tracks could accidently form a mass close to a charm mass. Removing events which have a secondary vertex z_{sec} close to one of targets significantly reduced that background.

K, p should be identified by RICH

For $D^0 \to K\pi, K\pi\pi\pi$ decays positive identification of the kaon is quite critical. Without particle identification one has to do all possible track combinations assigning kaon mass to different tracks, which are most likely to be pions, as pions are usually produced 10 times more copiously than kaons. The absence of particle identification leads to a significant increase of possible candidates and hence background. Similarly it is important to identify the proton in $\Lambda_c^+ \to pK^-\pi^+$ decays. For each track the RICH code calculated

the likelihood of this track being a proton, kaon or pion. (We also calculated likelihoods for other particles, but this is irrelevant in this discussion). A kaon was assumed to be positively identified if the likelihood of the track's being a kaon was greater than the likelihood of its being a pion. A proton was assumed to be positively identified if the likelihood of the track's being a proton was greater than likelihood of its being a pion.

In addition to p/π and K/π separation in the Λ_c^+ analysis we had to add p/K^+ separation to suppress the $D_s^+ \to K^-K^+\pi^+$ mass reflection (see Section 4.1 for details). For a track assumed to be proton we required that the likelihood of its being a proton was greater than 0.1, and the likelihood of its being a kaon was less than 0.9 - a very soft cut. It kept 97.5% of the Λ_c^+ signal but significantly suppressed the mass reflection.

Slow π rejection $p_\pi > 8\,\mathrm{GeV}$

Low energy pions were quite copious in the sample and because of multiple scattering their track errors were large. Because of the large errors those tracks could be assigned to both primary and secondary vertices, i.e., those tracks carried very little information about from which vertex they originated. It turned out that throwing those tracks out cost very little signal, and significantly decreased background.

3.3.2 Secondary interactions in the target

When a charm particle crosses a target, it can interact in the target and get lost. Thus the efficiency of the apparatus decreases as a function of proper time. On the other hand charm decay products can interact in the targets and get lost. The more targets a track has to cross before it can be measured in the vertex silicon, the bigger the loss. This effect increases the efficiency as a function of proper time.

The charm inelastic cross-section is not known, 13 mb is an estimate. Studies showed that effect of charm losses in the target contribute to very small changes in lifetime: $\Delta\tau(D^0) \sim 1$ fs and $\Delta\tau(\Lambda_c^+) \sim 0.5$ fs. This is small compared to the statistical error of lifetime measurement ~ 6 fs, an order-of-magnitude estimate of the charm inelastic cross-section is adequate for this study.

particle	Inel cross section	Losses per target
π	24 mb	0.57%
p	35 mb	0.82%
K	21 mb	0.49%
Charm	13 mb [a]	0.32%

Table 3.1: Losses of particles when they cross target
[a] This number is not measured. Rough estimate of this cross-section is adequate in this studies (see text for details).

3.3.3 Offline code reconstruction efficiency

Reconstruction code is never 100% efficient, and some charm events are always lost, which affects the individual event efficiency. There are many implicit cuts in the SELEX offline code, and we will describe only few important ones. Generally the reconstruction efficiency of the code is best calculated by processing simulated events directly with the offline code. This is the approach that we took in this analysis.

Good quality charm vertex.

One of the sources of background is tracks from the primary vertex that accidently form a secondary vertex outside of targets. For example if one track is mismeasured because a wrong hit is assigned to it, then it can form a fake vertex with another track. Such an event can pass the L/σ_L cut and sneak into the sample. Because such vertices are accidental, they usually have a bad vertex fit or large χ^2 value. On the other hand, real charm events should have a good vertex fit or small χ^2. We decided to accept only events with reduced $\chi^2_r = \frac{\chi^2}{ndf} < 5$, where ndf is the number of degrees of freedom of the fit. For example for 2-prong decays $ndf = 1$, for 4-prong decays $ndf = 5$.

For any given decay $\chi^2_r < 5$ will have a small inefficiency due to fluctuations in charm track measurement which can make $\chi^2_r > 5$. Ideally this efficiency is a fixed number and is not a function of proper time t. For example for 2-prong decay it's 97.5%, for 4-prong decays it's 99.9% In reality the efficiency is not a fixed number, but it is a function of proper time. It happens because we do not calculate resolution errors quite right, mainly because of non-gaussian effects. In our case we under/over estimated errors

in our calculations by a certain factor $f_\sigma = \sigma_{real}/\sigma_{calc}$, where σ_{real} are the real vertex errors and σ_{calc} are errors that we calculate. This error correction factor f_σ varied with the target where the primary interaction occurred and between which targets the charm particle decayed. The efficiency of the $\chi^2_r < 5$ cut depends on f_σ, which depends on origin and decay position of charm particle. Hence the efficiency of χ^2_r cut depends on t: efficiency changes when charm particle crosses the target.

Correction factors f_σ were calculated using the $K_s \to \pi^+\pi^-$ sample (Section 4.8.2) by comparing observed and expected vertex χ^2 distributions. Results of this study and are summarized in the Table 3.2.

target region where charm decayed	target where charm was produced				
	1	2	3	4	5
1-2	1.026				
2-3	1.063	1.109			
3-4	1.028	1.136	1.152		
4-5	0.918	1.148	1.215	1.235	
5-6	0.820	1.048	1.281	1.370	1.475

Table 3.2: Error correction coefficients f_σ

Suppression of secondary interactions in the targets

In the discussion of explicit cuts we explained why we did not accept vertices inside or close to the targets. To increase background suppression even more we decided also to reject tracks from secondary interactions. Tracks that formed a vertex inside a target downstream of the primary vertex were rejected from the track list and were not used to form secondary vertices. As shown in Fig. 3.6 it helps to suppress fake vertices formed between secondary interaction tracks and primary tracks. However it also suppresses 3,4-prong charm vertices which are close to the targets. Two-prong vertices will not be suppressed by this mechanism, as they are either inside or outside the targets. Multi-prong vertices which really lie outside targets may have two tracks which accidently form a vertex inside target and hence are rejected. This removes a valid charm multi-prong decay.

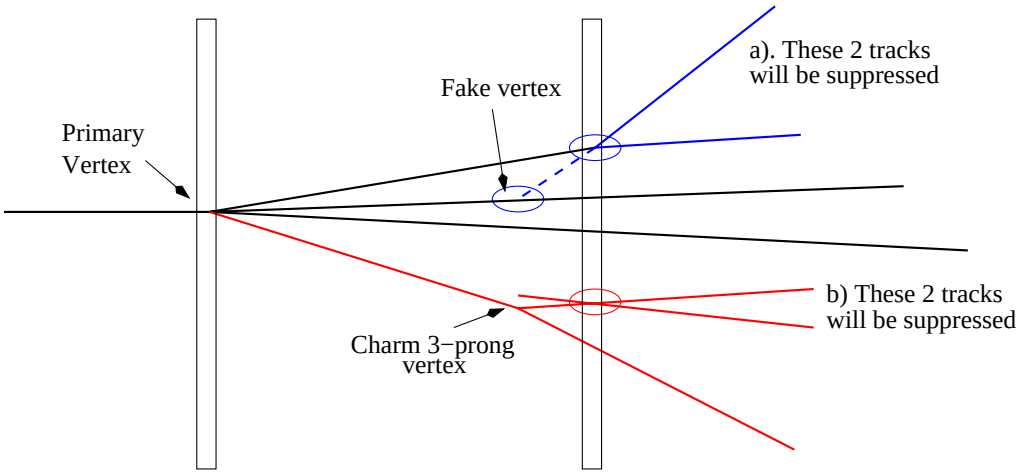

Figure 3.6: Suppression of secondary interactions.
[a] **Background suppression** these 2 secondary tracks form vertex inside the target. They will be suppressed, and the "fake" vertex formed by a secondary interaction track and a track from the primary will be suppressed.
[b] **Signal inefficiency** these 2 charm tracks form a vertex inside the target because one of them scattered. The charm tracks will be suppressed and the 3-prong vertex will be lost despite the fact that it is outside the target.

Reconstruction of high-multiplicity events

Reconstruction of secondary vertices is more complicated in events with high primary vertex track multiplicity. The efficiency of vertex reconstruction decreases. Interestingly enough it does not decrease uniformly, but is a function of proper time. The offline code first tests all events to see if they have just a primary vertex by fitting all the tracks to a common vertex. If the reduced χ^2_r fit of all tracks is satisfactory, then the event is rejected. In very high-multiplicity events, which have many low momentum tracks, an event that should have passed all the explicit cuts can be rejected because the low momentum tracks dominate the χ^2_r and hide the fact that there is a secondary vertex. This effect suppresses events with small proper time. Another effect is due to the suppression of secondary interactions in the targets, which in very high multiplicity events suppress events with large proper times.

3.4 Implementation of the method

In this analysis the following procedure was used to measure the lifetime:

- Find individual event efficiency $\epsilon(\vec{p}, t)$ as a function of proper time
- Generate a sample of "rethrown" events, that have the same configuration $\vec{p}$, but have different proper time t.
- Calculate the weight of each event $w(\vec{p})$
- Calculate the minimum proper time $t_{min}(\vec{p})$ for each event
- Calculate the overall efficiency of the observed sample $\epsilon(t)$
- Simultaneously fit the signal and background

3.4.1 Calculation of the individual event efficiency

In the first step the individual event efficiency $\epsilon(\vec{p}_0, t)$ was mapped out as a function of the proper time t. To do that each event described by parameters $\vec{p}_0$ was generated with different decay proper times t, keeping the decay configuration the same. Kinematical parameters (momenta, decay angles), target and primary vertex position were kept intact; other parameters were recalculated.

The proper time t is proportional to the length L between the secondary and the primary vertices. Individual event efficiency was calculated in 200 μm steps in L, which was sufficiently small compared to the L error $\sigma_L \simeq 500$ μm

The efficiency of the apparatus is defined by explicit cuts, losses in the targets and efficiency of the offline reconstruction program, which are discussed in detail in Section 3.3:

$$\epsilon = \epsilon_{code} \cdot \epsilon_{targets} \cdot \epsilon_{explicit} \tag{3.32}$$

Explicit cuts (like $L/\sigma_L > 8$) and losses in the targets were calculated. The efficiency of the reconstruction code was simulated: each rethrown event was fed back to the SELEX offline reconstruction program to find if it passed the code.

Simulation of the offline code reconstruction efficiency required a lot of computing: it needed about 50 times more computing time than all the other steps in the lifetime analysis combined. On the other hand explicit cuts are very easy to compute. So to save computing we calculated on this first step only the offline code reconstruction efficiency and saved the result. When the total efficiency was needed, the saved result was multiplied by the efficiency of the explicit cuts and losses in the targets. This was very helpful when the lifetime was studied as a function of different explicit cuts: the most time-consuming calculations were done only once.

3.4.2 Generation of the sample of rethrown events

Each event in the data sample $n(\vec{p})$ was used multiple times to generate $n_r(\vec{p}, t)$ - a set of events with the same decay properties $\vec{p}_0$, which only differ by decay proper time t. This set is referred to as a set of "rethrown" events. In this analysis we used each event to generate 1000 new rethrown events distributed exponentially in proper time. So each individual event produced a set of rethrown events:

$$n_r^{ind}(\vec{p}, t) = 1000 \cdot \delta(\vec{p} - \vec{p}_0) \cdot \frac{1}{\tau} e^{-t/\tau}. \tag{3.33}$$

Then the whole sample of rethrown events was described by:

$$n_r^{all}(\vec{p}, t) = \int n_r^{ind}(\vec{p}, t)\, d\vec{p} = 1000 \cdot n(\vec{p}) \cdot \frac{1}{\tau} e^{-t/\tau}. \tag{3.34}$$

This generated sample of 1000 rethrown events was found to be large enough by comparing to a lifetime calculation based on 100 rethrown events. The difference was less than 0.3 fs which is very small compared to the lifetime statistical error of ~ 6 fs.

After the rethrown sample was generated, resolution effects were applied. Parameters of the charm track and both primary and secondary vertices were smeared according to track and vertex error matrices. Secondary parameters like track intercepts, vertex separation resolution σ_L and others were recalculated. After that all rethrown events were tagged if they pass or fail the cuts by the procedure describe in Section 3.4.1.

3.4.3 Calculation of the weight of each event

Next the weight for each individual event was calculated (Eq.3.16). The rethrown sample $n_r^{ind}(\vec{p},t)$ had an exponential distribution $e^{-t/\tau}$ (Eq. 3.33). Calculation of the integral in Eq.3.16 is very simple: the inverse of the weight is equal to the fraction of generated events that passed the cuts:

$$\frac{\int n_r^{ind}(\vec{p},t)\cdot\epsilon(\vec{p},t)\,dt}{1000} = \int \frac{1}{\tau}e^{-t/\tau}\cdot\epsilon(\vec{p}_0,t)\,dt = w^{-1}(\vec{p}_0) \tag{3.35}$$

3.4.4 Calculation of the minimum proper time t_{min} for each event

The choice of minimum proper time is somewhat arbitrary: if you shift all $t_{min}(\vec{p})$ by some amount which may even differ for different subsamples, then the reduced proper time distribution will still have an exponential shape. Formally, the choice of $t_{min}(\vec{p})$ only has to be consistent: for every decay configuration $\vec{p}$ there has to be unique choice of $t_{min}(\vec{p})$. Indeed, the reduced proper time distribution $n_r(t_r)$ relates to the proper time distribution $n(t)$ as:

$$n_r(t_r) = n(t_r + t_{min}(\vec{p}))\times|\frac{dt}{dt_r}|. \tag{3.36}$$

Under a change of variables $t_r = t - t_{min}(\vec{p})$, $n(t)$ transforms as a probability density. If t_{min} depends only on $\vec{p}$ and does not depend on t then $|\frac{dt}{dt_r}| = 1$, and $n_r(t_r)$ has the same time-dependence as $n(t)$. As we already discussed, $t_{min} = 8\cdot\sigma_L$ is not a very good choice, because σ_L depends on t. Although

there is a certain freedom in choosing $t_{min}(\vec{p})$, in practice you choose it close to the proper time t where most data passes the cut, as you fit reduced proper time distribution for $t_r > 0$.

In this analysis we have chosen the following procedure to find $t_{min}(\vec{p})$.

1. For each event an ideal, non-smeared event was formed: all charm secondary tracks come from a secondary vertex point, the charm track points exactly to the primary vertex point, which was perfectly aligned along the beam. This was done to exclude randomness due to resolution smearing in calculation of t_{min}.

2. After that, the event was moved upstream along the direction of the charm, keeping all the properties of decay $\vec{p}$ fixed until it triggered any cut that would throw it out of the sample. Effectively t_{min} was defined by 3 cuts: vertex separation $L/\sigma_L > 8$, second largest misdistance $s_2/\sigma_{s_2} > 4$ cm and distance to the closest target $\Delta z_{tgt} > 0.05$ cm. Since the vertex error changes when we move upstream, σ_L was recalculated on every step.

3. Cuts like L/σ_L or s_2/σ_{s_2} are non-linear as a function of proper time t, so an iterative numerical procedure was used to find $t = t_{min}(\vec{p})$. The starting point for this iterative procedure was chosen by generating a sample of events $n(\vec{p}, t)$ with the same decay parameters $\vec{p}$, but different t and picking the smallest t for which event still passed the cuts.

This procedure guaranteed that for every event described by parameters $\vec{p}$ we have a unique choice of $t_{min}(\vec{p})$ independent of t. The numerical error on $t_{min}(\vec{p})$ was less than 0.3 fs and its effect on final answer was of order $\sigma_t/\sqrt{N} < 0.006$ fs, totally negligible.

3.4.5 Calculation of the overall efficiency

The rethrown events $n_r(\vec{p}, t)$ was used to calculate the overall efficiency $\epsilon(t)$ in Eq.3.20. For proper time t $\epsilon(t)$ (Eq. 3.20) was equal to the fraction of all weighted rethrown events that passed the cuts:

$$\frac{\int n_r^{all}(\vec{p}, t)\, w(\vec{p}) \cdot \epsilon(\vec{p}, t)\, d\vec{p}}{\int n_r(\vec{p}, t)\, w(\vec{p})\, d\vec{p}} = \frac{\int n(\vec{p})\, w(\vec{p}) \cdot \epsilon(\vec{p}, t)\, d\vec{p}}{\int n(\vec{p})\, w(\vec{p})\, d\vec{p}} = \epsilon(t) \qquad (3.37)$$

As shown in Eq. 3.33 we generated rethrown events $n_r(\vec{p}, t)$ exponentially distributed in proper time. It's purely a matter of convenience: it simplified

the weight calculations and also made calculations of efficiency $\epsilon(t)$ for small proper times more accurate. This is because there were more generated events $n_r(\vec{p}, t)$ at small proper time, making the statistical error smaller at small proper time t. This is very useful, as most of our events have small proper times.

Efficiency calculations in Eq.3.20 were derived for signal events only. In the data we had background contamination as well. To take that into account, we calculated both numerator and denominator in Eq.3.20 for signal and background regions, and applied the sideband subtraction technique as discussed in Section 3.1.1 to extract numerator and denominator for signal events.

3.4.6 Fitting procedure

As we discussed in Section 3.1.4 we simultaneously fit proper time distribution of events in the sidebands $N_b(t)$ and of events in the signal region $N_s(t)$ using functions:

$$N_s(t) = \frac{N_0}{\tau} e^{-t/\tau} \cdot \epsilon(t) + C \cdot B(t) \tag{3.38}$$

$$N_b(t) = \frac{N_1}{\tau_1} e^{-t/\tau_1} + \frac{N_2}{\tau_2} e^{-t/\tau_2} \tag{3.39}$$

$N_s(t)$ and $N_b(t)$ are just integer numbers of observed events in proper time bin t. In each bin these numbers have a Poisson distribution. For that reason we a used binned log-likelihood fitting technique to accommodate Poisson errors.

If either of the above functions $N_{s,b}(t)$ changes rapidly inside a bin then one has to take into account that the number of events $N_{s,b}(t)$ is the integral of the distribution function over the width of the bin, rather than just the absolute value of $N_{s,b}(t)$ in the middle of the bin, as assumed in most fitting packages. We took integration over the bin width into account.

In the binned log-likelihood procedure one has to normalize the integral of fitting function to the known number of events in the signal and background regions N_{tot}:

$$N_{tot} = N_0 \cdot \epsilon + N_1 + N_2, \tag{3.40}$$

So instead of 6 free parameters the fit should have 5 free parameters and the normalization condition (Eq. 3.40). It turns out that both procedures (with

6 free parameters and with 5 free parameters + normalization condition) give very close lifetimes. The difference was less than 0.1 fs, which is negligible compared to the lifetime statistical error ~ 6 fs.

To do the fitting we used programs PAW and MINFIT, which use MINUIT [77] package for minimization. Both gave the same results.

3.5 Discussion of the method

In this method we heavily exploit the fact that the lifetime is independent of the parameters $\vec{p}$ that describe the decay. One should be careful in choosing this set of parameters, so that no parameter of the set $\vec{p}$ depends on the proper time t. Parameters such as track momenta, angles between tracks and similar parameters that describe decay kinematics certainly qualify for this list. On the other hand vertex resolution σ does not qualify: if we fix everything else in a decay and vary t , then for larger t the vertex resolution σ gets smaller as events get closer to the silicon detector. In other words events with the same σ will not be distributed exponentially. Mathematically speaking, Eq.3.11 will no longer be true.

To calculate the weight in Eq.3.16 one needs to know the lifetime τ. Evaluating the lifetime is our final goal, and we need it as an input. The formal solution to this is to use iterative procedure: one starts with some starting lifetime τ_0 to find the efficiency and extract a more precise estimate τ_1, then use it for the next iteration and so on. Special studies showed that this procedure converges extremely quickly. From other experiments both D^0 and Λ_c^+ lifetimes were known with a few percent error, so estimators were not a problem (Section 4.5).

3.5.1 Procedure verification

This lifetime analysis technique is new. So we decided to check that all the formulas and procedure were implemented right. To do that a sample of events was simulated with a known lifetime. The simulated events were processed through the whole chain of lifetime analysis procedure, and the lifetime for each sample was calculated. The input lifetime 413.7 fs agrees quite well with average reconstructed lifetime 415.4 ± 1.5 fs (Figure 3.7). Even the calculated lifetime error 6.0 fs is close to observed RMS of 4.8 fs.

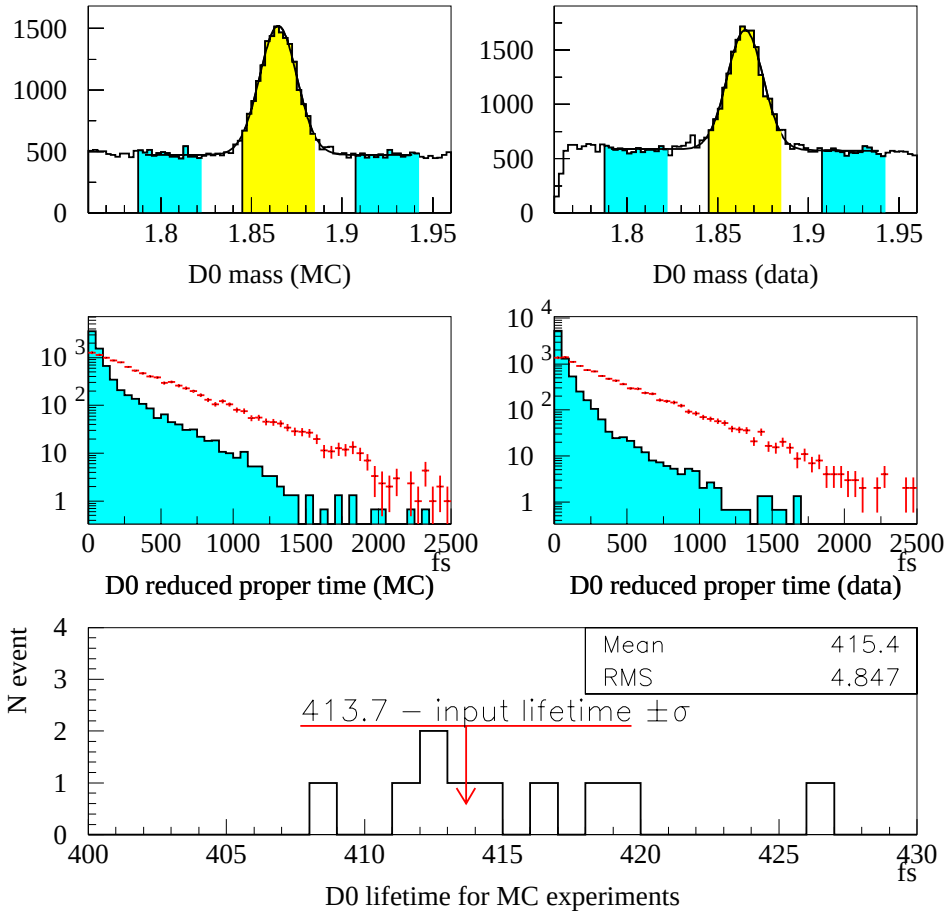

Figure 3.7: Procedure verification

3.5.2 Advantages, disadvantages and unsolved issues

A big advantage of this method is that one does not need to know the production properties of the charm sample $n_0(\vec{p})$. Also, there is no need to simulate the efficiency of detectors which are not sensitive to the decay proper time t. In our case we did not simulate RICH or downstream chambers, but concentrated on vertex silicon and target region.

However as any method it has its disadvantages. First of all it explicitly assumes an exponential shape of the decay curve. If someone would like to study the deviation of the decay curve from a pure exponential (mixing for example) this method is not directly applicable. Also this method concentrates on efficiency calculations and mostly ignores resolution effects. In our case it was a right choice - the experiment has a non-trivial acceptance, and resolution effects were tiny. For some other experiments the situation is the opposite: the efficiency is quite simple, and the resolution is the problem. For example, in CLEO where the charm particle travels a few millimeters, the acceptance is uniform. All the emphasis of the analysis is concentrated on the understanding of resolution effects [29].

In this method the efficiency is basically a sum of individual event efficiencies. If one has a large sample of events the resulting overall function is a smooth function, as it should be. If one has only a few events, the resulting function may have sudden jumps due to sample fluctuations. So the error on the efficiency for small sample may be large. In our case we had several thousands signal events and it was not a problem. We verified that on simulated samples, and also checked that smaller subsamples give consistent lifetimes. If one has only a few dozen events, the efficiency calculated with our method will not be precise enough. Then the conventional method, which predicts efficiency with large sample of simulated events may be more applicable.

This method will have problem when weights of events are very large. That corresponds to very small acceptance. In our case weights for reduced time were about 1.5. If the weights were about 100 and one would observe only 20 events, then this method would extrapolate behavior of original 2000 events based on only 20 events, which clearly would have problems with statistical fluctuations. But if the weights are so large, perhaps measurement of lifetimes in such apparatus is not a good idea in the first place.

There are at least two unsolved issues in this method. First of all it is not clear how to incorporate large proper time resolution effects in the method. Secondly it is not clear what is the smallest sample when the procedure is

still applicable.

3.5.3 Conclusion

To summarize we constructed a method to combine lifetime measurements for different subsamples and to find the efficiency correction for overall sample. The formalism can be used to combine lifetime measurements for different decay modes or for charm particles produced in different targets. It was very important that we did not need to assume a production distribution $n_0(\vec{p})$ of the events, but rather we calculated the efficiency $\epsilon(t)$ for the events $n(\vec{p})$ that we actually observed.

Chapter 4

Systematic Errors

In this section I'm going to discuss systematic errors of lifetime measurement and various checks we used to verify them. Here is the list of systematics we are going to discuss in this chapter:

- Mass reflections
- Background systematics
- Charm induced backgrounds
- Mismeasurement of the primary vertex
- Initial Lifetime uncertainty
- Efficiency calculations
  - Lifetime for different targets
  - Lifetime for different decay modes
  - Lifetime for different charm momentum
  - Lifetime for different track multiplicities
  - Lifetime for different L/σ cuts
  - Lifetime for different minimum distances to the closest target
  - Lifetime for different L_{max} cut
  - Lifetime for different minimum π energy
- Miscellaneous systematics

4.1 Mass reflections

Mass reflections are caused by misidentification of particles and result in missassignment of particle mass. An example would be K/p misidentifica-

tion when a proton mass is assigned to a kaon. In this case some decays $D_s^+ \to K^+K^-\pi^+$ would be interpreted as $\Lambda_c^+ \to pK^-\pi^+$. Some of those misinterpreted D_s^+ may end up having the Λ_c^+ mass, thus contaminating the Λ_c^+ sample . This phenomenon is known as a mass reflection. The D_s^+ has a lifetime twice as long as Λ_c^+, so this may increase the observed Λ_c^+ lifetime. Another example of reflection due to p/K misidentification is the reflection of Cabibbo suppressed $D^+ \to K^-K^+\pi^+$ on Λ_c^+. There is also p/π misidentification, which causes a different $D^+ - \Lambda_c^+$ reflection: $D^+ \to K^-\pi^+\pi^+$ and one π^+ is misidentified with p. In SELEX the RICH detector [69] had excellent p/π separation (Figure 2.14)and greatly suppressed this mass reflection.

First let's find how D_s^+, D^+ would reflect on Λ_c^+. One can do that from D_s^+, D^+ data samples, but relatively large backgrounds would make it quite complicated. Instead we used the Monte-Carlo for this study. Simulation included, as usual, complete tracking and particle identification. Events were completely reconstructed by offline code with the same cuts as in lifetime analysis. We generated samples which contained only D_s^+ or D^+ events, so that Λ_c^+ candidate events could be generated only due to mass reflections. The lower plots in Fig.4.1 show $D_s^+ \to K^-K^+\pi^+$ and $D^+ \to K^-\pi^+\pi^+$ samples that passed the cuts and went into this study. The upper plots show fake Λ_c^+ events generated by mass reflections. The shaded regions on the upper plots show regions that we used for signal and sidebands in the Λ_c^+ lifetime study.

One can clearly see that the D^+ reflection was greatly suppressed mostly by RICH p/π separation. Also this reflection populated the $pK^-\pi^+$ mass spectrum with a linear mass dependance and was effectively suppressed by the background subtraction procedure described in Section 3.1.1. D^+ reflection was quite small. On the other hand misidentified D_s^+ clearly did not fit a linear mass dependance. After background subtraction some D_s^+ mismeasured events remain in the Λ_c^+ signal.

For the D^0 meson there were no reflection problems, as D^0 is the only stable neutral charm meson.

4.1.1 $D_s^+ - \Lambda_c^+$ reflection without p/K separation

In this section we did not use any information from the RICH to separate p from K^+. To estimate the number of D_s^+ that remained in the Λ_c^+ signal we took all $\Lambda_c^+ \to pK^-\pi^+$ candidate events, including background, replaced the p mass by the K mass and tried to find a $D_s^+ \to K^+K^-\pi^+$ signal. And

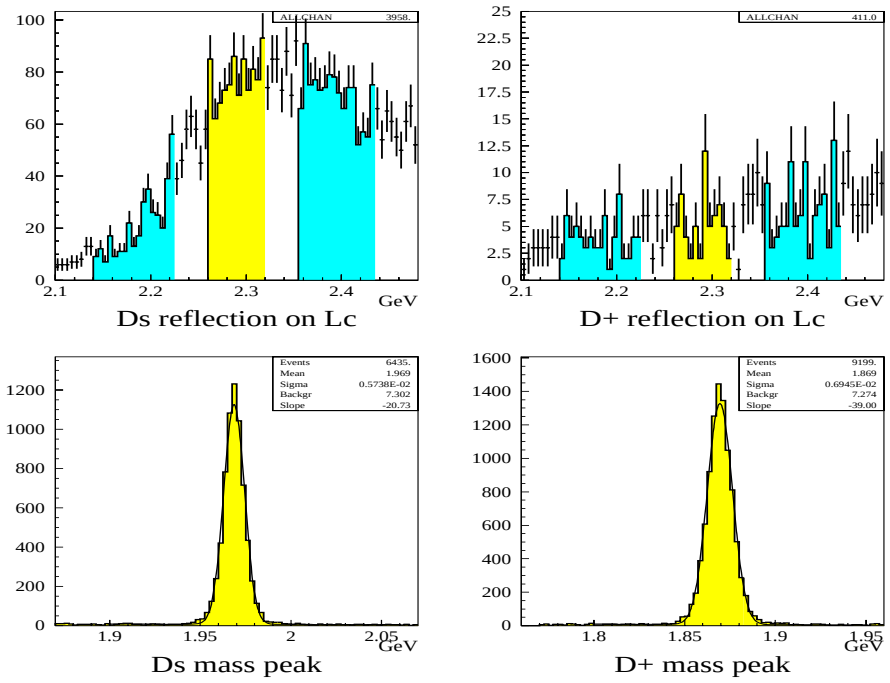

Figure 4.1: Reflection of D_s^+ and D^+ on Λ_c^+ mass spectrum from Monte-Carlo

we did detect D_s^+ events in Λ_c^+ sample (Fig.4.2). One can also see a hint of ≤ 80 Cabibbo suppressed $D^+ \to K^+K^-\pi^+$ events reflected on Λ_c^+ in upper right plot.

mode	mass region	MC prediction		Data
		fraction	events[a]	events
D_s^+ from all $\Lambda_c^+ \to pK^-\pi^+$	2.100 - 2.480	100.0%	norm	246 ± 60
D_s^+ from Λ_c^+ left sideband	2.140 - 2.220	7.7%	19	
D_s^+ from Λ_c^+ central area	2.260 - 2.315	21.1%	51	
D_s^+ from Λ_c^+ right sideband	2.355 - 2.435	28.7%	71	74 ± 19
D_s^+ from Λ_c^+ right side	2.320 - 2.480	56.5%	139	111 ± 22
$D_s^+ \to K^+K^-\pi^+$ signal[b]		163.0%	401	406 ± 61
unsubtracted D_s^+	2.260 - 2.315	8.6%	21	

Table 4.1: D_s yields from different samples. Actual fits are shown on Fig.4.2. Information from RICH was not used to separate p from K^+.
[a] We normalised the predicted number of MC events to 246 events observed in all Λ_c^+ sample.
[b] Actual D_s^+ signal observed in the data. MC predicted the fraction of these events which reflected on Λ_c^+ reasonably well.

One can see reasonable agreement between MC predictions and the actual number of D_s^+ observed in Λ_c^+ sample (Table 4.1). The MC prediction is that 21 D_s^+ contaminate the Λ_c^+ signal (Fig.4.1), because of incomplete background subtraction. These 21 D_s^+ events have longer lifetime than Λ_c^+ ($\tau_{D_s} = 496 \pm 10$ fs, $\tau_{\Lambda_c} = 206 \pm 12$ fs [4]), which would lead to increase of observed lifetime $\Delta\tau$ approximately by:

$$\Delta\tau \simeq \frac{N_{\Lambda_c} \cdot \tau_{\Lambda_c} + N_{D_s} \cdot \tau_{D_s}}{N_{\Lambda_c} + N_{D_s}} - \tau_{\Lambda_c} \approx \frac{N_{D_s}}{N_{\Lambda_c}}(\tau_{D_s} - \tau_{\Lambda_c}) \approx 3.7 \text{ fs} \qquad (4.1)$$

as in our case $N_{\Lambda_c} = 1630$ and $N_{D_s} \approx 21$.

4.1.2 Suppression of mass reflections using information from RICH.

As we saw, without RICH information the systematic error is understood, but it is quite large. Bringing information from the RICH to separate p from

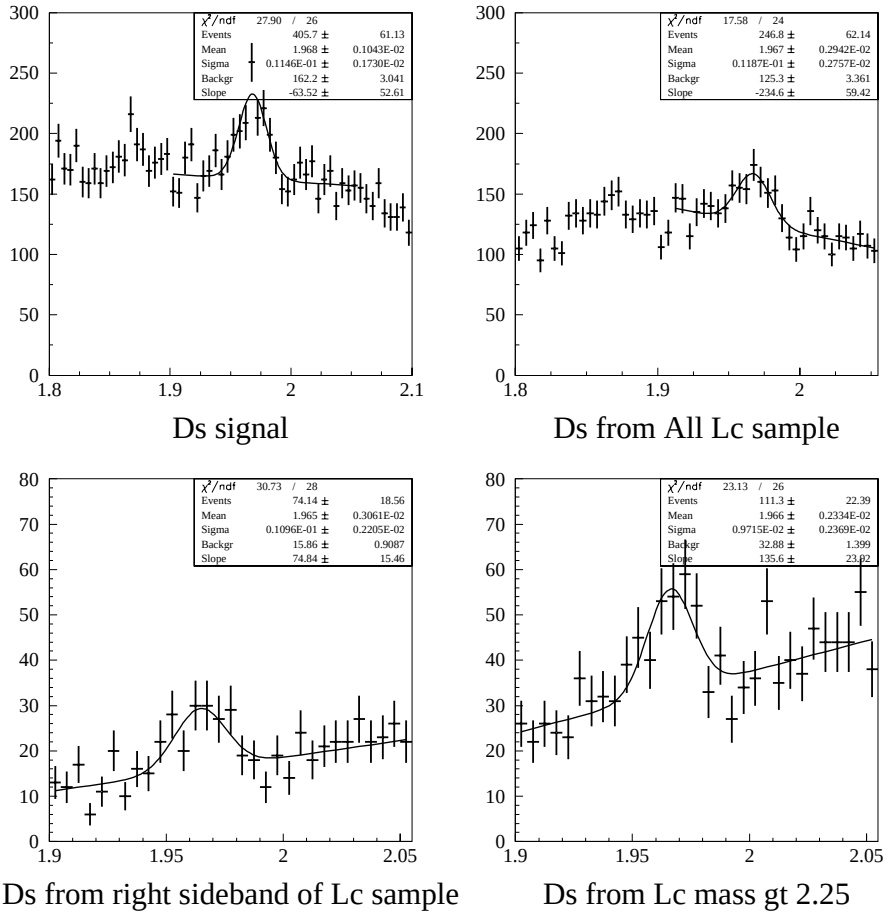

Figure 4.2: D_s^+ signal in Λ_c^+ sample, information from RICH was not used to separate p from K^+.

K dramatically improved the situation. It turned out that applying even the softest cuts on particle identification: likelihood of proton candidate to be proton > 0.1 and likelihood of it to be kaon < 0.9, significantly suppresses the D_s^+ reflection.

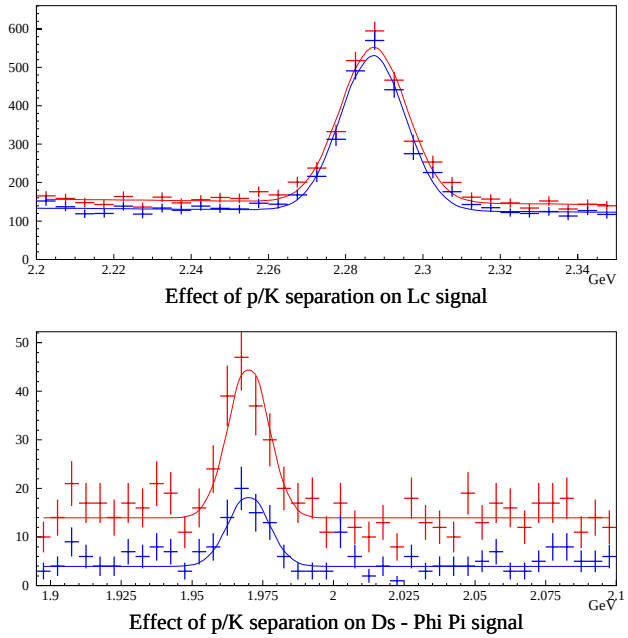

Figure 4.3: Effect of applying RICH p/K^+ separation on Λ_c^+ and $D_s^+ \to \phi\pi^+$ signals. Results of the fit are summarized in Table 4.2

The extra cut to separate p from K^+ slightly reduced the signal, but suppressed the reflection by a factor of $\times 2.2$. This cut also changes the shape of the mass reflection and hence the fraction of events that would contaminate Λ_c^+ signal after sideband subtraction.

We did not observe any $D^+ \to K^-\pi^+\pi^+$ reflection in the Λ_c^+ signal. From the MC we know that about 4.1% of all $D^+ \to K^-\pi^+\pi^+$ signal reflected into the Λ_c^+ 400 MeV-mass window. We observed 1890 D^+, so we expected about 75 events to be reflected on Λ_c^+. For all 3 reflections we used analysis similar to $D_s^+ - \Lambda_c^+$ reflection that was discussed in previous section 4.1.1. Results of mass reflection systematics caused by D^+, D_s^+ are summarized in Table 4.3.

Decay	Yield		Ratio
	no p/K^+ separation	with p/K^+ separation	
$\Lambda_c^+ \to pK^-\pi^+$	1750 ± 58	1704 ± 55	97.4 %
$D_s^+ \to \phi\pi^+$	113 ± 14	52 ± 9	46.0 %

Table 4.2: Effect of applying p/K^+ separation on Λ_c^+ and $D_s^+ \to \phi\pi^+$ signals

Decay	No p/K^+ separation			
	unsubtracted fraction[a]	observed signal[b]	unsubtracted signal[c]	$\Delta\tau^d$ (fs)
$D_s^+ \to K^-K^+\pi^+$	8.6 %	246	21	3.6
$D^+ \to K^-K^+\pi^+$	2.8 %	≤ 80	2.2	1.1
$D^+ \to K^-\pi^+\pi^+$	1.0 %	75[e]	0.8	0.4
Total				5.1
Decay	With p/K^+ separation			
$D_s^+ \to K^-K^+\pi^+$	1.2 %	112[f]	1.3	0.2
$D^+ \to K^-K^+\pi^+$	4.0 %	35[f]	1.4	0.7
$D^+ \to K^-\pi^+\pi^+$	1.0 %	75[e]	0.8	0.4
Total				1.3

Table 4.3: Summary of systematics caused by mass reflections. Using RICH to separate p from K^+ greatly decrease this systematic error.

[a] Fraction of decay reflections that will remain in the Λ_c^+ signal after sideband subtraction. Predicted by Monte Carlo.

[b] Number of decay reflections present in the whole Λ_c^+ sample.

[c] Number of decay reflections that will remain in Λ_c^+ signal after background subtraction. It is equal to the product of the observed signal times unsubtracted fraction.

[d] Systematics error on Λ_c^+ lifetime.

[e] Signal was too small to be observed in the data, MC prediction was used instead, see text for details.

[f] Applying p/K^+ separation suppressed those signals by factor 2.2

4.2 Charm induced backgrounds

One possible source of background is events induced by the presence of different charm decays. Consider a $D^+ \to K^-\pi^+\pi^+$ decay. It forms a valid 3-prong vertex, but if there is another soft π^- in the event and if one of π^+ is mismeasured, then these tracks can accidently form a 4-prong vertex $K^-\pi^+\pi^+\pi-$ and have the D^0 mass. The lifetime of such events is dictated by the D^+ lifetime and hence can potentially make the observed D^0 lifetime longer. As in the case of any other background, background subtraction is supposed to take care of that, unless the background shape in the mass distribution is significantly non-linear. To check this, we used the Monte-Carlo and generated different charm decay samples for $D^+, D^0, D_s^+, \Lambda_c^+ + cc$ to see if they formed some unusual background shape.

As seen in Fig.4.4 charm-induced backgrounds do not form any significantly nonlinear background shape. Sideband subtraction will take care of those events. We are going to discuss systematics caused by sideband subtraction in Section 4.4.

4.3 Mismeasurement of the primary vertex

Another systematic may be caused by mismeasurements of the primary vertex. An event with a charm decay has always an anti-charm decay, as c and $\overline{c}$-quarks are produced in pairs. This anti-charm decay can be close to the primary vertex, so that its tracks are included in primary vertex fit. Then the observed position of the primary vertex will be measured downstream of its actual position.

If t' is the measured proper time, and t is the real proper time of the decay, then the measured proper time distribution $n'(t')$ refers to real proper time distribution $n(t)$ as:

$$n'(t') = \frac{n(t)}{|dt'/dt|} \tag{4.2}$$

If t' is systematically mismeasured, so that $t' = (1-\alpha)\cdot t$ - then the observed charm lifetime τ' will also be mismeasured: $\tau' = (1-\alpha)\cdot\tau$

To observe this systematic mismeasurement one can study the distribution of the secondary vertex position s'_z with respect to the primary vertex position p'_z. In ideal case there should be no correlation between the two. Correlation between the two would indicate systematic mismeasurement. The

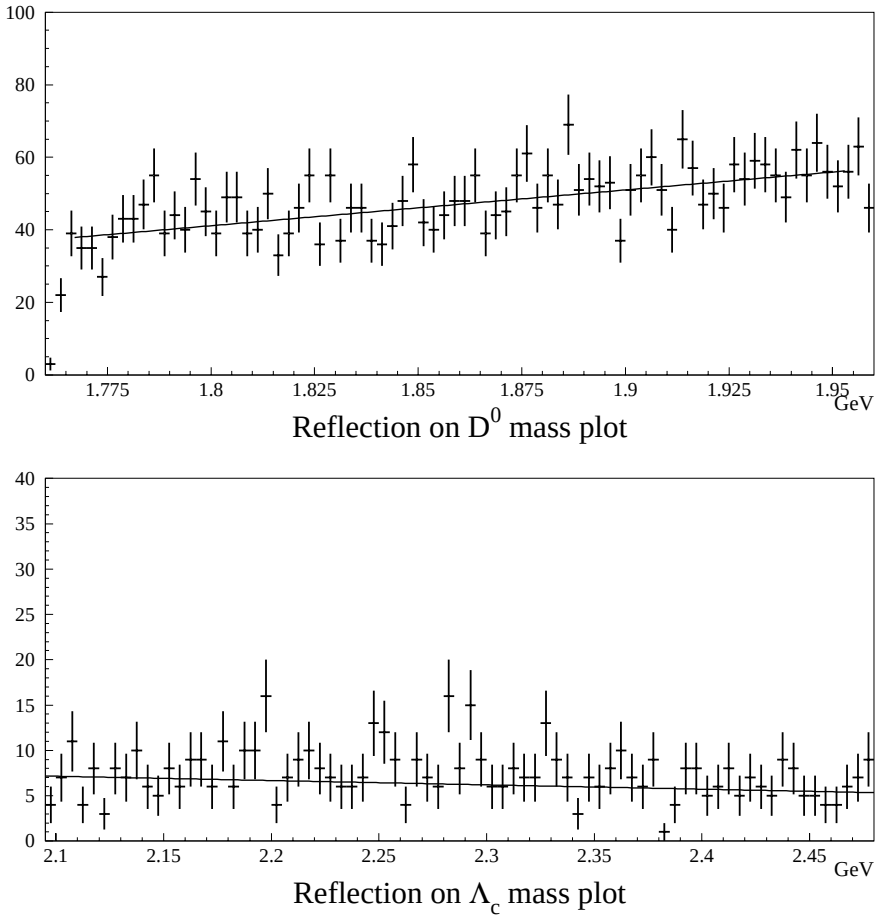

Figure 4.4: Charm induced backgrounds for D^0 and Λ_c^+

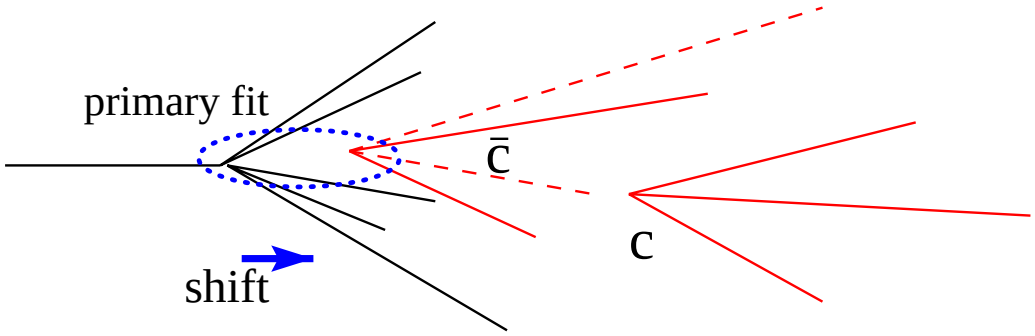

Figure 4.5: Systematics due to primary vertex mismeasurements. Second charm decay in the event systematically shifts downstream the observed primary vertex position.

reduced proper time is give by:

$$t_r = \frac{L - L_{min}}{c \cdot \gamma} = \frac{z_{sec}}{c \cdot \gamma} - \frac{z_{prim}}{c \cdot \gamma} - t_{min}, \tag{4.3}$$

where z_{prim} is given by Eq. 3.30. We studied the correlation between $t_{sec} \equiv z_{sec}/(c \cdot \gamma) - t_{min}$ and $t_{prim} \equiv z_{sec}/c \cdot \gamma$. A correlation α between them would make a systematic error $\alpha \cdot \tau$ in the lifetime measurement. A small correlation was observed in this study and upper bounds were set (Figure 4.6). Systematic errors are summarized in Table 4.4

Particle	α	σ_α	bound [a]	σ_{syst} [b] [fs]
Λ_c^+	0.0028	0.0030	0.0058	1.1
D^0	0.0014	0.0009	0.0023	1.0

Table 4.4: Systematic errors due to mismeasurement of the primary vertex.
[a] bound is equal to mean value of the slope plus one standard deviation
[b] systematic error is equal to $\alpha \cdot \tau$.

4.4 Background subtraction systematics

In previous sections we discussed specific systematics associated with different backgrounds. In this section we would like to check if there are any

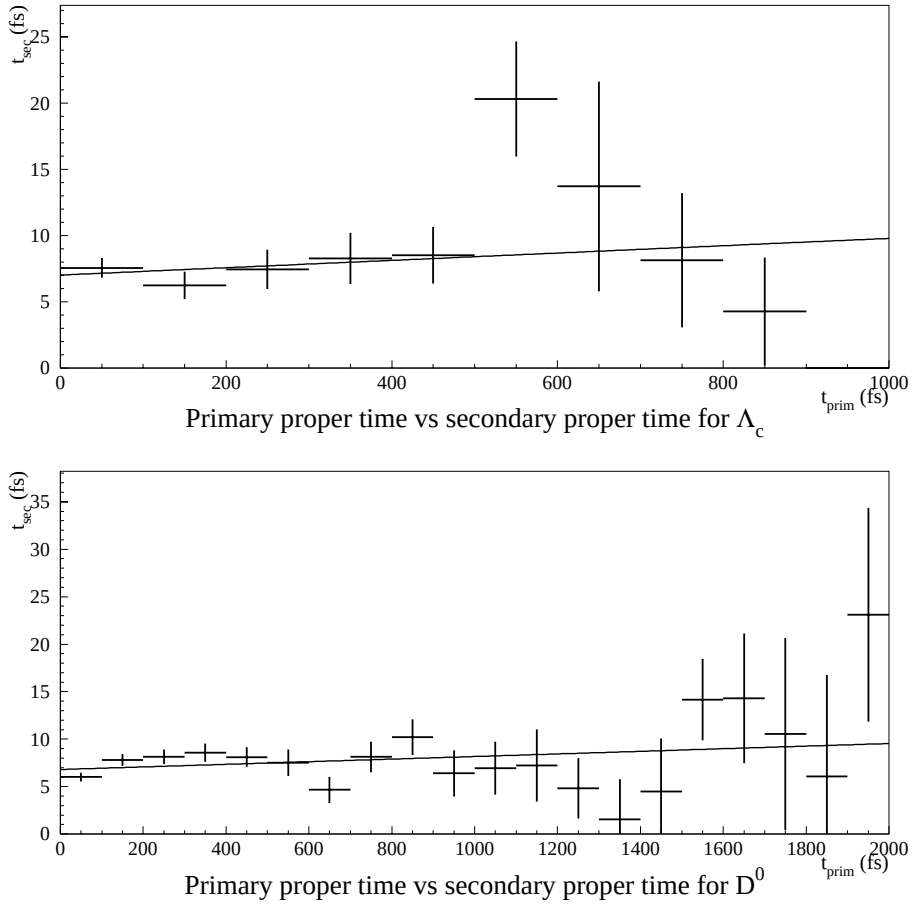

Figure 4.6: Systematics due to primary vertex mismeasurement. There was little correlation between t_{sec} and t_{prim} observed. We used the same fitting limits as in lifetime fit. Note large difference in scale on two axis. We put a bound equal to mean value of the slope + 1 standard deviation.

systematics left due to background. This lifetime analysis is fundamentally based on the assumption that the background behavior under the signal peak can be extracted from the events in the mass sidebands. We can verify this assumption, choosing different regions for sidebands. If the choice of region affects the final answer by an amount larger than just statistical fluctuations, that would indicate presence of some systematics. We estimate systematics due to background by choosing 5 different sidebands and computing 5 different lifetimes. After that RMS of those 5 measurements was calculated to characterize variations of lifetime.

We observed that different choices of sidebands caused variation of lifetime with RMS equal to 1.18 fs for D^0 and 0.80 fs for Λ_c^+. To find the significance of those variations in lifetime we performed a special study: 100 samples were generated by a simplified "toy" Monte-Carlo for D^0 and Λ_c^+. Properties of events in the simulated samples were close to those in observed sample, and background properties for simulated events indeed were the same for signal regions and sidebands. After that we made exactly the same analysis for those toy samples as for real events and measured the RMS variation in lifetime, which in this case arises purely from statistical fluctuations in the sidebands.

Simulated events predicted that the expected statistical variation of RMS was equal to 0.61 fs for D^0 and 1.02 fs for Λ_c^+. (Fig.4.8). For Λ_c^+ the observed variation in lifetime did not exceed expected variations, so no systematic error was assigned to Λ_c^+. For D^0 the observed RMS was larger than expected, and systematic error was assigned according to:

$$\sigma_{observed} = \sqrt{\sigma^2_{expected} + \sigma^2_{syst}} \tag{4.4}$$

In the fitting procedure the statistical error on lifetime already includes statistical fluctuations in background. One should not add the observed variations $\sigma_{observed}$ in lifetime as an extra systematic error. Only excess of the observed variation over the expected variation qualifies as a systematic error.

4.5 Systematics due to initial lifetime uncertainty

To calculate efficiency corrections, one needs to know the individual event weights $w(\vec{p})$, which are given by formula 3.16. Weight calculations require

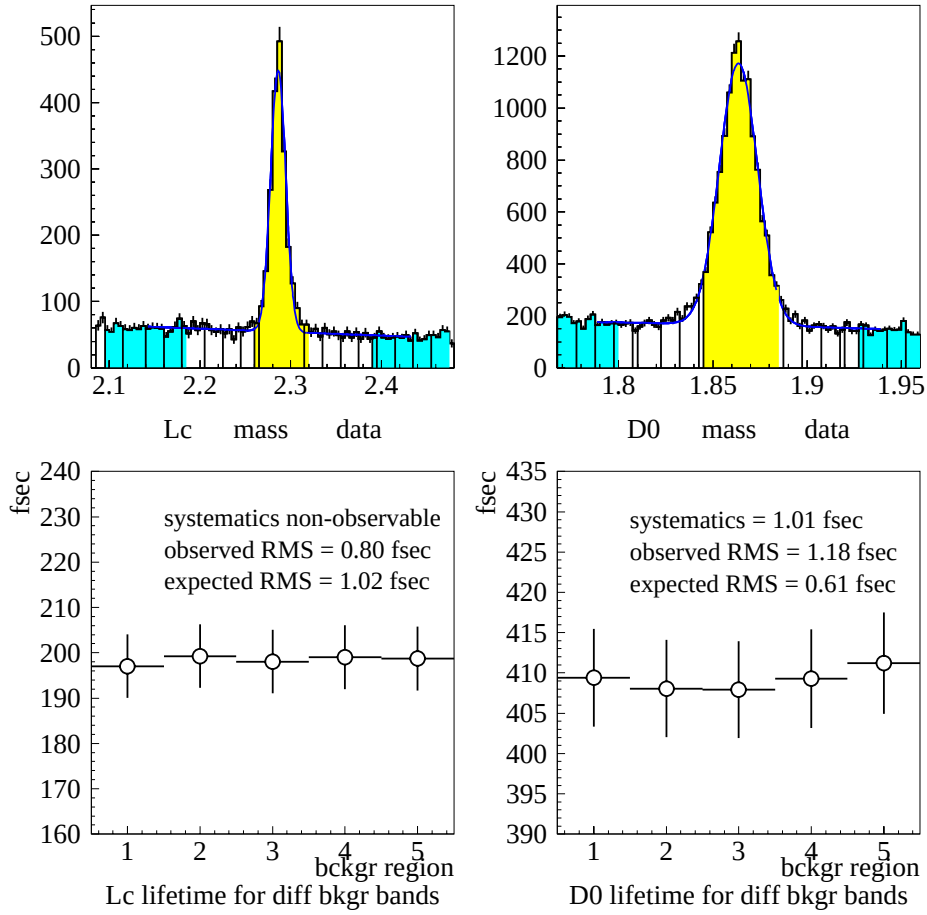

Figure 4.7: Background systematics: lifetime for different sideband regions. Observed RMS of 5 points was measured. Expected RMS was studied using Monte-Carlo samples (Figure 4.8). Systematic error was extracted using formula in Eq. 4.4

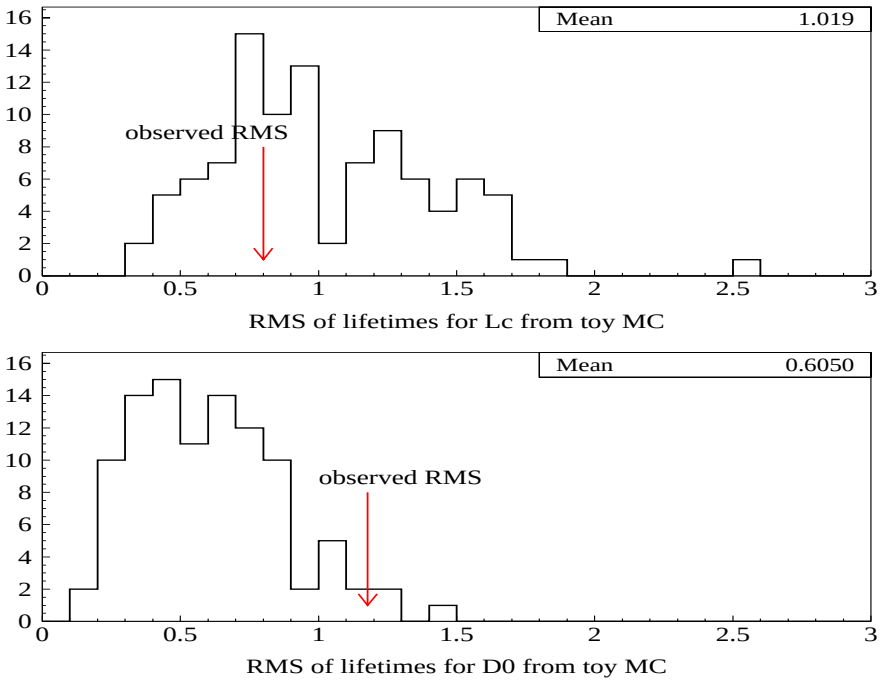

Figure 4.8: Background systematics: comparison of expected and observed RMS of lifetimes for different sideband regions. Expected RMS was generated by 100 MC samples and is caused purely by statistical fluctuations in sidebands. There is no evidence for extra systematics in Λ_c^+ signal. The observed RMS for the D^0 lifetime exceeds expected value, and a systematic error was assigned

knowledge of the lifetime as an input, yet lifetime is what we are looking for. As we discussed in Section 3.5 a rigorous approach would require an iterative procedure: first you calculate weights and efficiency 3.20 based on some initial lifetime τ_0, and use those calculations to find next lifetime iteration τ_1, recalculate weights and efficiency to find τ_2 and so on, until procedure converges to some final lifetime τ_f (Figure 4.9).

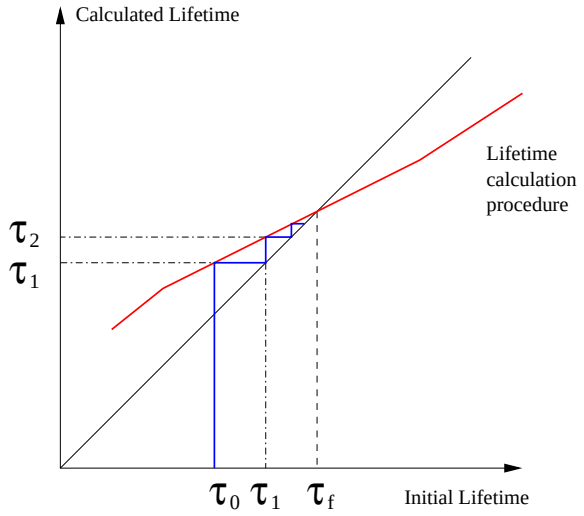

Figure 4.9: Iterative procedure of lifetime calculations

But it turned out that the overall efficiency didn't depend very much on the weights, and lifetimes of D^0, Λ_c^+ had been measured by previous experiments to within a few percent. Thus one iteration was quite enough for these lifetime measurements. If one linearizes the lifetime calculation procedure in the vicinity of τ_f and denotes the slope as k, then

$$k = \frac{\tau_{i+1} - \tau_f}{\tau_i - \tau_f}, \tag{4.5}$$

where τ_{i+1}, τ_i are consecutive iterative steps of lifetime measurement procedure. The deviation of the first iteration from the final answer is given by:

$$\tau_1 - \tau_f = \frac{k(\tau_0 - \tau_1)}{1 - k} \approx k(\tau_0 - \tau_1), \tag{4.6}$$

as k is small. To estimate k we studied how much the first lifetime iteration τ_1 changed when initial lifetime τ_0 was varied by 10%. Results of this

Particle	τ_0 [fs]	$\Delta\tau_1$ for 10% change in τ_0 [fs]	k	τ_1 [fs]	observed $\tau_1 - \tau_0$ [fs]	syst err $\tau_1 - \tau_f$ [fs]
Λ_c^+	206	0.6	0.029	198.1	-7.9	0.23
D^0	415	1.4	0.034	407.9	-7.1	0.24

Table 4.5: Systematics due to the uncertainty in the initial lifetime

systematics study are summarized in Table 4.5. Even one iteration gave a lifetime estimate τ_1 very close to the final lifetime τ_f, so we decided not to do several iterations and used τ_1 as our lifetime measurement.

4.6 Systematics due to efficiency calculations

It turned out that systematic effects due to efficiency calculations produce the biggest error that we have. In this chapter we discuss several studies we made to test the efficiency calculations.

There were two types of studies we made: lifetime for independent subsamples and lifetime stability versus cut variation. In addition we made indirect verifications of the efficiency calculations.

4.6.1 Lifetime for independent subsamples

In this study the charm sample was divided in several smaller subsamples. Each event was only in one subsample, so lifetimes calculated for each subsample were independent measurements. If there were no systematic errors, lifetimes for each subsample should be consistent with each other. Deviations between them may be due only to statistical fluctuations.

To quantify the systematic error the following procedure was used. All independent measurements were fit to a constant value and χ^2 value of the fit was calculated. For m subsamples number of degrees of freedom of the fit is $ndf = m-1$. If $\chi^2/ndf < 1$ no systematics was assigned. If $\chi^2/ndf > 1$ an excess of $\chi^2/ndf - 1$ was assigned to systematic error using simple scaling:

$$\frac{\chi^2}{ndf} - 1 = \left(\frac{\sigma_{syst}}{\sigma_{stat}}\right)^2, \tag{4.7}$$

4.6.2 Stability of lifetime versus cut variation

In this study the lifetime was calculated for different values of one of the explicit cuts (Section 3.3.1). The lifetime should be the same regardless of the choice of cuts. In this study different measurements are not independent, on the contrary they are highly correlated. So $\chi^2/ndf > 1$ analysis and formula in Eq. 4.7 are not applicable in this case.

Let's consider the lifetime calculated for different L/σ_L cuts. The D^0 sample defined by $L/\sigma_L > 8$ cut and sample defined by $L/\sigma_L > 9$ cut have 96% events in common. Because of the high overlap these two measurements cannot differ from each other by much unless there is a systematic error. We decided to estimate how much two highly-correlated measurements could differ due to statistical fluctuations. A systematic error is assigned if the difference is larger than this expectation.

Consider a sample of N_0 events. After applying a tighter cut the sample consists of N_1 events. The number of events that are thrown own out of the sample is $N_2 = N_0 - N_1 \ll N_0$. Let the lifetimes of the these samples be τ_0, τ_1 and τ_2 and weights (or $1/\sigma_\tau^2$) of those measurements be w_0, w_1 and w_2. The weight of a lifetime measurement is approximately proportional to the number of events in the sample:

$$w \equiv \frac{1}{\sigma^2} \propto N \ . \tag{4.8}$$

The samples N_1 and N_2 do not have events in common. They are independent measurements and combined together would have lifetime τ_0. Then:

$$\begin{aligned} \tau_0 &= \frac{\tau_1 \cdot w_1 + \tau_2 \cdot w_2}{w_1 + w_2}, \quad \text{or} \\ \tau_1 - \tau_0 &= (\tau_0 - \tau_2) \cdot \frac{w_2}{w_1} \end{aligned} \tag{4.9}$$

Equation 4.9 gives a relation between the fluctuations of N_1 and N_2 samples. The $1 \cdot \sigma$ fluctuation of small sample $N_2 \ll N_0$ from τ_0 is approximately σ_{τ_2}. Then, using Eq. 4.8 for weight, $1 \cdot \sigma$ deviation of the N_1 sample is approximately:

$$\sigma_1 \simeq \sigma_0 \sqrt{\frac{N_0 - N_1}{N_1}}, \tag{4.10}$$

where σ_0 is lifetime error for the sample N_0.

If the deviation $\tau_1 - \tau_0$ exceeds expected σ_1 then the systematic error was assigned:

$$\frac{\sigma_{syst}}{\sigma_0} = \frac{|\tau_1 - \tau_0|}{\sigma_1} - 1 \tag{4.11}$$

We used Eq. 4.10, to evaluate how much lifetimes for highly-correlated samples N_0 and N_1 can deviate from each other. An excess over σ_1 in the lifetime difference was attributed to systematic error. Equation 4.10 is approximate. It does not take into account effects of background or efficiency $\epsilon(t)$, but it is a reasonable estimate.

Both methods (Eq.4.7 and Eq. 4.10) are just estimates, because they basically compare lifetime differences and $1 \cdot \sigma$ statistical fluctuation. Statistical fluctuations may be larger than $1 \cdot \sigma$. These formulas work quite well when systematic errors are large compared to statistical. When the systematic error is small, one can conclude only that it is smaller than the statistical error. The formulas give an estimate of an effect, but they are not a precise measure by any means. On the other hand these methods are very general. They can indicate presence of systematics even if the source of it is unknown.

4.6.3 Lifetime for different targets

The efficiency for different targets is quite different. Charm particles from target 5 have only 2.3 cm to decay, while those from target 1 have 10 cm to decay. Charm that was produced in target 5 encounters no targets in its path, while charm produced in the first target has 4 targets along the way. Also vertex resolution changes when we go upstream. Lifetimes measured in different targets are independent measurements and we used method discussed in Section 4.6.1.

Results of this study are shown in Figure 4.10 and are summarized in Table 4.6. There was no evidence for systematics for Λ_c^+ or D^0.

	Λ_c^+	D^0
χ^2/ndf	3.5 / 4	2.2 / 4
stat error	7.0 fs	6.0 fs
syst error	0 fs	0 fs

Table 4.6: Systematics extracted from lifetimes for different targets. Actual fits are shown in Fig.4.10

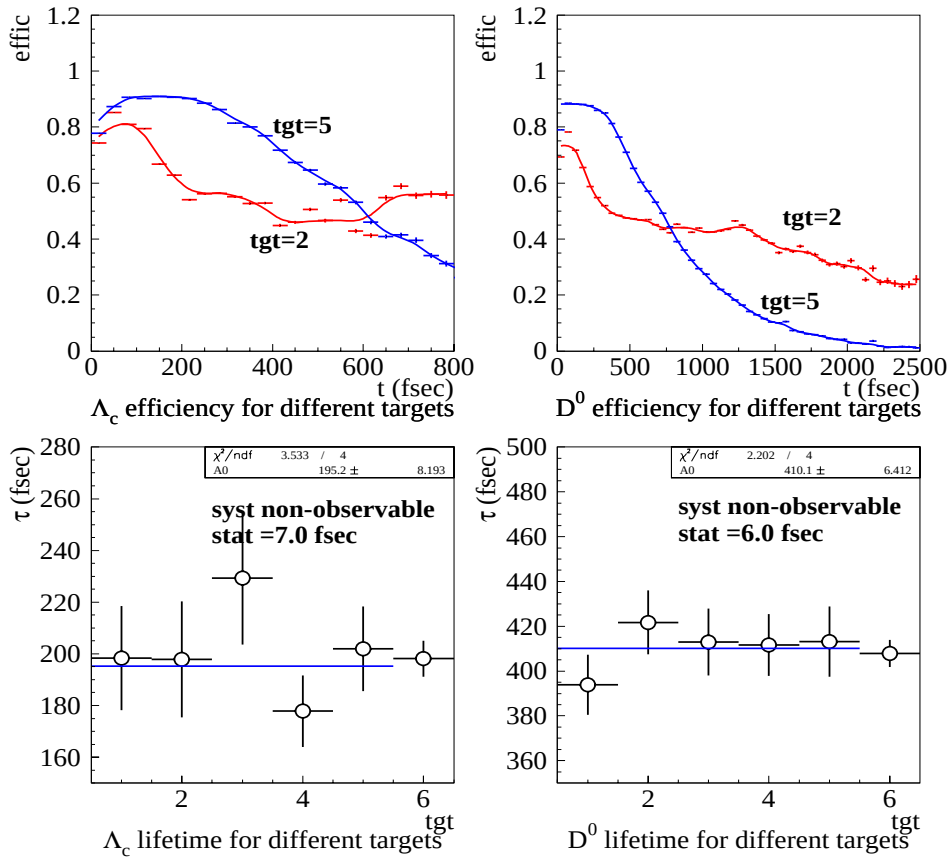

Figure 4.10: Efficiency systematics: lifetime for different targets. Two upper plots show efficiency calculated for target 2 and target 5 for Λ_c^+ (left) and D^0 (right). Efficiency is more flat for target 2 because charm has larger distance to travel before it reaches $z = 2.3$ cm. Lower plots show lifetimes for 5 different targets. The 6-th point is the lifetime for the whole sample and is shown for reference. For both Λ_c^+ and D^0 fit of independent measurements has $\chi^2/ndf < 1$. There is no evidence for systematics in this study.

4.6.4 Lifetime for different decay modes

For $D^0, \overline{D^0}$ we have observed 4 decay modes: $D^0 \to K^-\pi^+$, $\overline{D^0} \to K^+\pi^-$, $D^0 \to K^+\pi^+\pi^-\pi^-$ and $\overline{D^0} \to K^-\pi^-\pi^+\pi^+$. Those are independent samples, and we can compare their lifetimes to check for systematics. There is not much difference between D^0 and $\overline{D^0}$ decays, but 2 and 4-body decays are quite different. They have different efficiency functions, due to different momentum spectra: we cut out low-energy particles, so observed 4-body decays on average have higher momenta than 2-body decays of D^0. More importantly, the 4-body decay mode has higher losses around the targets, due to mechanism of suppression of secondary interactions that is discussed in Section 3.3.3. The 2-body mode is sensitive to the secondary vertex $\chi^2_{sec} < 5$ cut discussed in Section 3.3.3 while 4-body mode is not.

Results of this study are shown in Figure 4.11 and are summarized in Table 4.7. Comparison of the four different modes did not show any systematics. Comparison of combined 2-prong ($K^-\pi^+$ and $K^+\pi^-$) versus 4-prong decays ($K^-\pi^+\pi^-\pi^+$ and $K^+\pi^-\pi^+\pi^-$) showed small systematics.

	Comparison of 4 modes	2-prong vs 4-prong
χ^2/ndf	1.46 / 3	1.28 / 1
stat error σ_{stat}	6.0 fs	6.0 fs
syst error σ_{syst}	0 fs	3.3 fs

Table 4.7: Systematics extracted from lifetimes for different D^0 decay modes

4.6.5 Lifetime for different charm momentum

The efficiency function is sensitive to the momentum of the charm particle, since the proper time $t \propto L/p_z$, where p_z is the momentum of charm. We calculated lifetime for different $x_F \simeq p_z/p_{beam}$ ranges.

Results of this studies are shown in Figure 4.12 and in Table 4.9. No systematics was observed in this study for Λ_c^+ or D^0.

4.6.6 Lifetime for different event track multiplicities

As a general rule the efficiency of reconstruction decreases when the number of tracks in the event increases. This effect is discussed in detail in Sec-

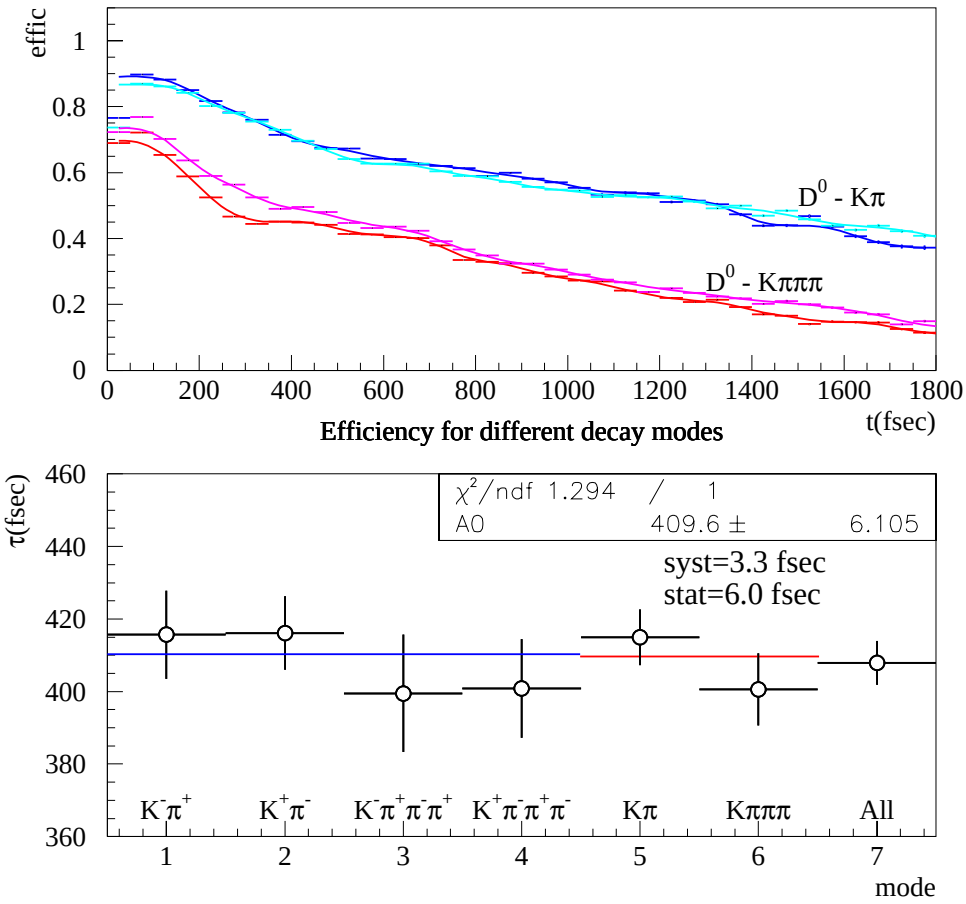

Figure 4.11: Efficiency systematics: $D^0, \overline{D^0}$ lifetime for different decay modes. The upper plot shows efficiencies for 2 different decay modes and their charge conjugates. A global fit of all four modes is shown on the lower plot. It also includes comparison of 2-prong and 4-prong decay modes. Last point "All" shows lifetime measurement for the whole sample. Results of this study are summarized in Table 4.7

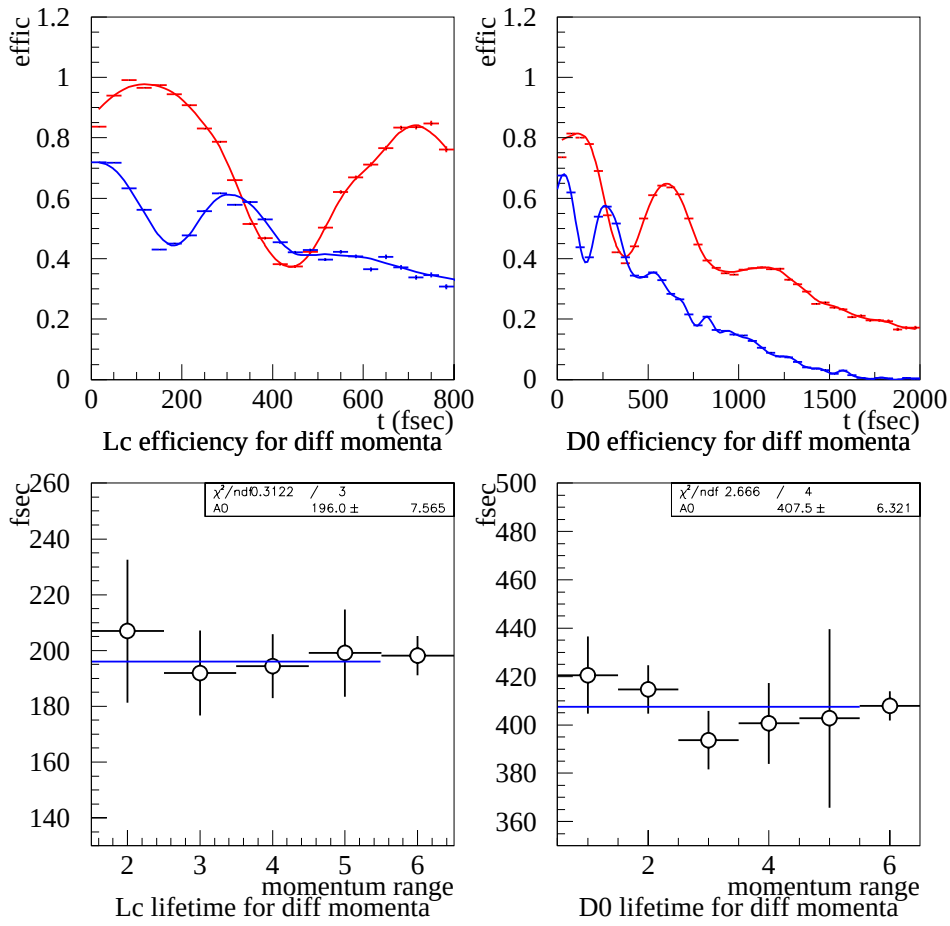

Figure 4.12: Efficiency systematics: lifetime for different charm $x_F \simeq \frac{p_{charm}}{p_{beam}}$ ranges. Definitions of ranges are given in Table 4.8. Upper plots show efficiencies for x_F ranges number 3 and number 5. One can see deeps in efficiency functions, that correspond to the next downstream target located at about 1.5 cm downstream. First points 1-5 correspond to independent measurements in different x_F ranges. 6-th point shows lifetime for the whole sample and is shown for the reference. Λ_c^+ sample has almost no data in the 1-st range and this point was omitted. There was no evidence for systematics in this study.

Range	x_F values
1	less than 0.15
2	0.15 - 0.25
3	0.25 - 0.35
4	0.35 - 0.50
5	greater than 0.5

Table 4.8: x_F values for different ranges

	Λ_c^+	D^0
χ^2/ndf	0.3 / 3	2.7 / 4
stat error σ_{stat}	7.0 fs	6.0 fs
syst error σ_{syst}	0 fs	0 fs

Table 4.9: Systematics extracted from lifetimes for different x_F regions. Actual fits are shown in Figure 4.12

tion 3.3.3. This study is an important check of the simulation of the SELEX offline reconstruction efficiency. Ignoring the fact that efficiency depends on event multiplicity would result in large systematic error about 2 times the size of the statistical error.

Results of the studies are shown in Figure 4.13 and are summarized in Table 4.11. Small systematics was observed for Λ_c^+.

Range	Number of tracks in primary vertex
1	Less than 8
2	8 - 11
3	12 - 13
4	13 - 15
5	greater than 15

Table 4.10: Track multiplicities for different ranges

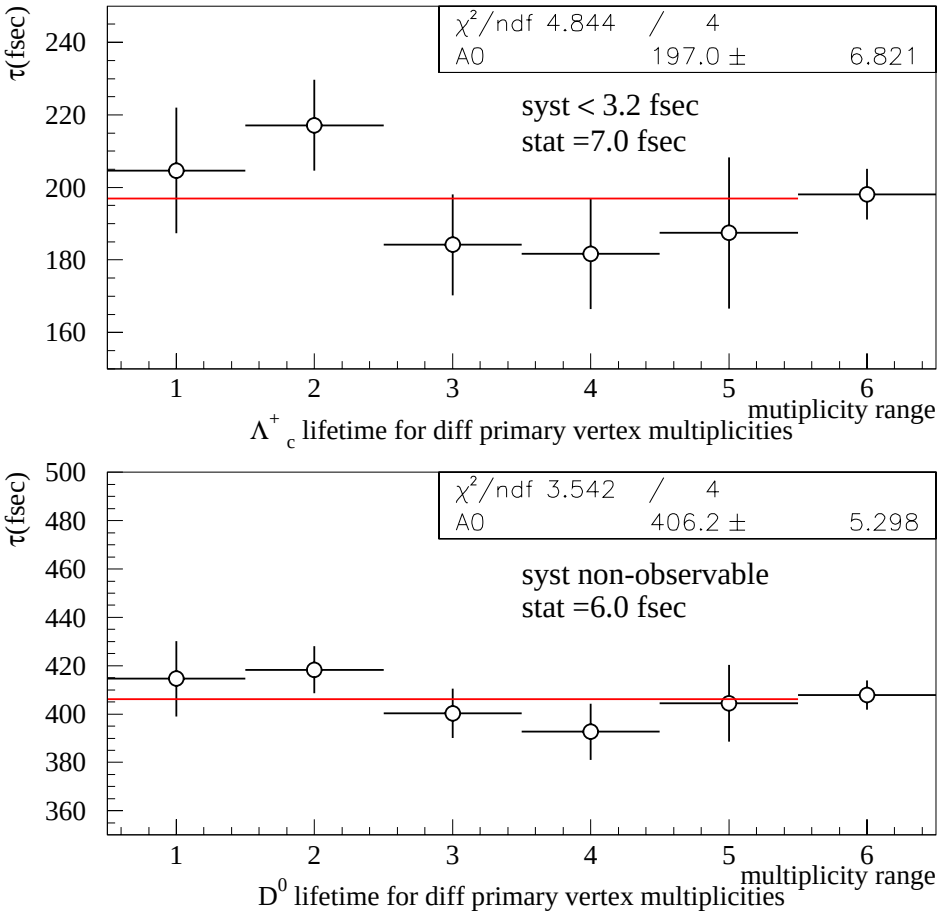

Figure 4.13: Lifetime for different primary vertex track multiplicity ranges. Definitions of track multiplicity ranges are given in Table 4.10. First 5 points correspond to 5 independent measurements. 6-th point is the lifetime for the whole sample and is shown for the reference. Small systematics was found for Λ_c^+ sample.

	Λ_c^+	D^0
χ^2/ndf	4.8 / 4	3.5 / 4
stat error σ_{stat}	7.0 fs	6.0 fs
syst error σ_{syst}	3.2 fs	0 fs

Table 4.11: Systematics extracted from lifetimes for different primary vertex track multiplicities study. Actual fits are shown in Fig.4.13

4.6.7 Lifetime for different L/σ cuts

In this study we verified that the lifetime did not change with the change of L/σ cut. There are 2 reasons why the lifetime could depend on L/σ cut and hence indicate possible systematic error. First, events with small L/σ values are events that are close to the primary vertex. Generally, reconstruction efficiency in the fixed target environment decreases when the distance L between the secondary and primary vertices gets smaller. At some point the reconstruction program can not resolve a secondary vertex when it is too close to the primary vertex. Secondly, events with small L/σ values have a higher background contamination. If the properties of the background for those events are not well understood, it could affect the proper time distribution for small L/σ events.

Results of this study are shown in Figure 4.14. For Λ_c^+ all the points were within allowed corridor and no systematics was assigned. For D^0 two points jump out of allowed corridor. Systematic errors were calculated for both points and the largest value of 1.3 fs was assigned as a systematic error.

4.6.8 Lifetime for different minimum distances to the closest target

Reconstruction efficiency near targets drops because we cut out any secondary vertices that are close to the targets. More importantly suppression of secondary interactions in the targets (Section 3.3.3) decreases efficiency near the targets. To check efficiency simulation near the targets we studied lifetime for different Δz_{tgt} cuts. This way we cut out "uncertain" region around the targets, and tested if the result remained the same. Events with the minimum distance $\Delta z_{tgt} > 0.05$ cm were selected in the final sample.

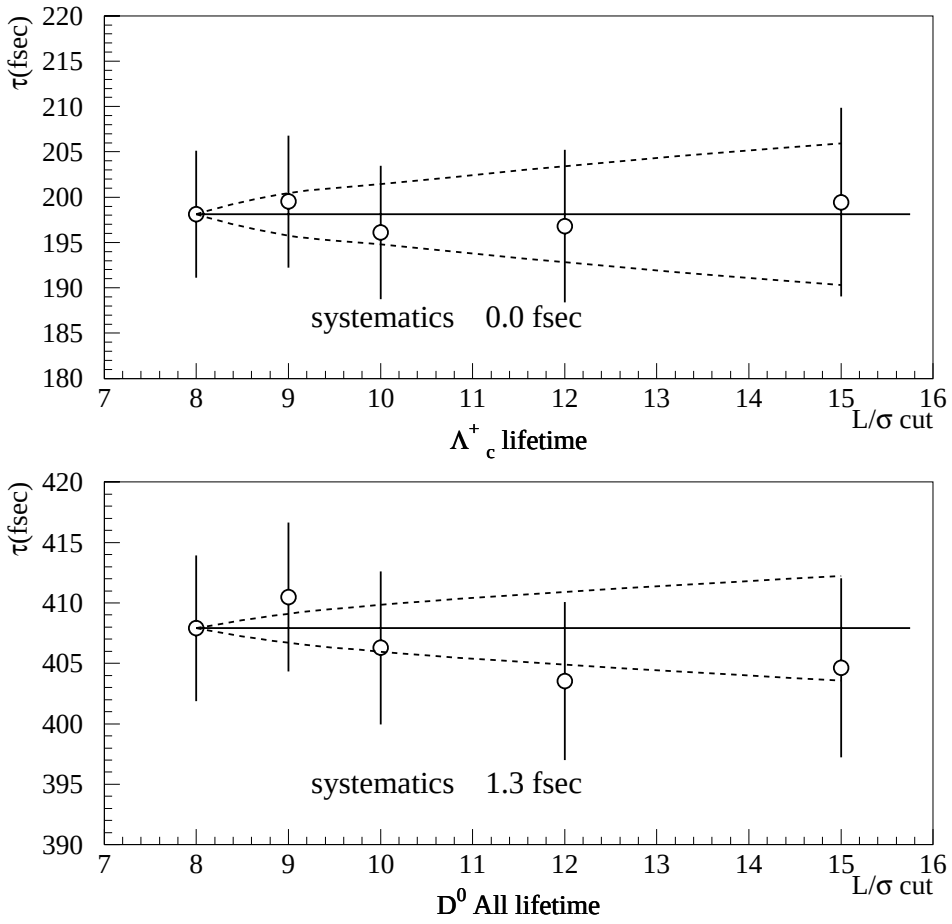

Figure 4.14: Efficiency systematics: lifetime for different L/σ cuts. Curved lines show allowed fluctuations corridors calculated using Eq. 4.10. All Λ_c^+ lifetime measurements are within the allowed corridor. Hence there is no evidence for the systematics in the Λ_c^+ sample. One D^0 measurement jumps out of the allowed corridor and 1.3 fs systematics was assigned to this jump using Eq. 4.11.

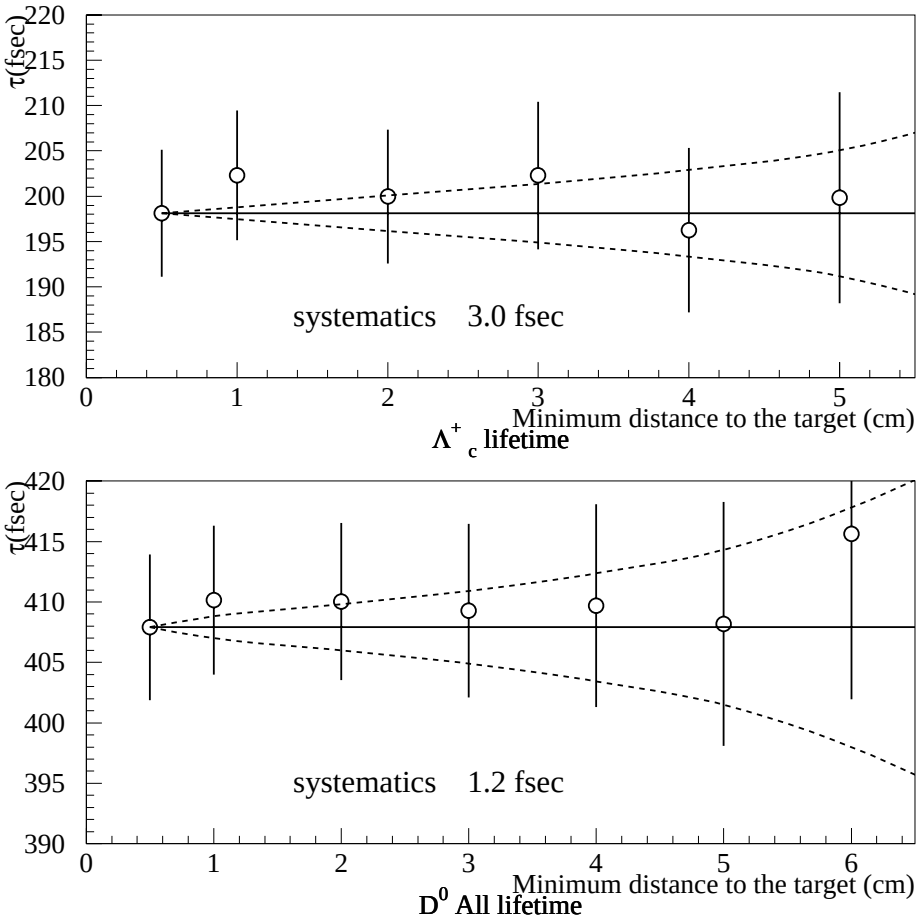

Figure 4.15: Efficiency systematics: lifetime for different target cuts. Curved lines show allowed fluctuations corridors calculated using Eq. 4.10. For both Λ_c^+ and D^0 points jump out of the allowed corridor. For each point that jumped out systematic error was calculated. The largest value among them was assigned as a systematic error. Small systematic errors of 3.0 fs and 1.2 fs were assigned in this study to Λ_c^+ and D^0.

For both Λ_c^+ and D^0 small systematic errors were observed. Lifetimes deviated from the allowed range and systematic errors of 3.0 fs and 1.2 fs were assigned to Λ_c^+ and D^0 (Figure 4.15).

4.6.9 Lifetime for different L_{max} cut

In this study we decided to check the stability of the lifetime for different L_{max} cuts. Only events with $L < L_{max}$ were accepted. 4 values of L_{max} cut were used in this study. The first subsample has events that could cross only 1 target, second have events that could only cross 2 targets and so on. So this study addresses the simulation when the particle traverses one or more downstream targets. We tested that events with large L were simulated correctly.

In the whole sample L_{max} was implicitly defined by $z_{sec} < 2.3$ cm (Section 3.3.1). It was equal to $z_{sec_{max}} - z_1 \simeq 8.4$ cm, where z_1 is the position of the first target. For both Λ_c^+ and D^0 small systematic effects were observed. Lifetimes deviated from the allowed range and systematic errors of 1.2 fs and 0.9 fs were assigned to Λ_c^+ and D^0 (Figure 4.16).

4.6.10 Lifetime for different minimum π energy

In this study we verified that the lifetime did not depend on cut on minimum π momentum. Simulation of reconstruction of low energy pions is complicated by large multiple scattering of those pions. The efficiency of track reconstruction and hence the reconstruction of charm drops. In this study we wanted to verify that it did not affect lifetime measurement. Events with π momentum greater than 8 GeV/c were selected in the final sample.

For Λ_c^+ lifetime small systematics was observed. Lifetimes deviated from the allowed range of lifetimes and systematic error of 2.3 fs was assigned.

4.6.11 Online filter systematics

Online filter selected events which had evidence for the secondary vertex (Section 2.3.1). Online filter rejected events which had small proper time and affected acceptance of the apparatus. So online filter systematics contributes to the efficiency systematics, which is covered in this section. Anyway we specifically address online filter systematics:

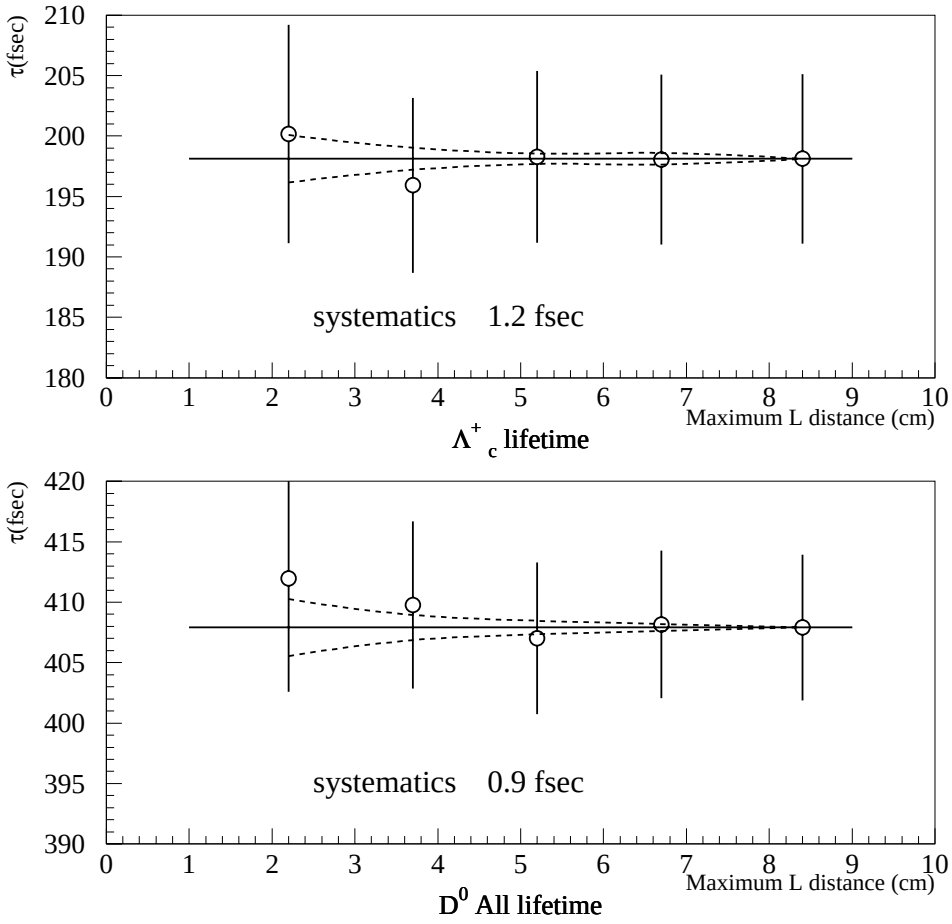

Figure 4.16: Efficiency systematics: lifetime for different L_{max} cuts. 4 first points correspond to 4 different cuts that were used in this study. Last point correspond to the whole sample. The implicit cut $L_{max} = 8.4$ cm was used in the whole sample (see text for details). Curved lines show allowed fluctuations corridors calculated using Eq. 4.10. For both Λ_c^+ and D^0 points jump out of the allowed corridor. For each point that jumped out systematic error was calculated. The largest value among them equal to 2.3 fs was assigned as a systematic error.

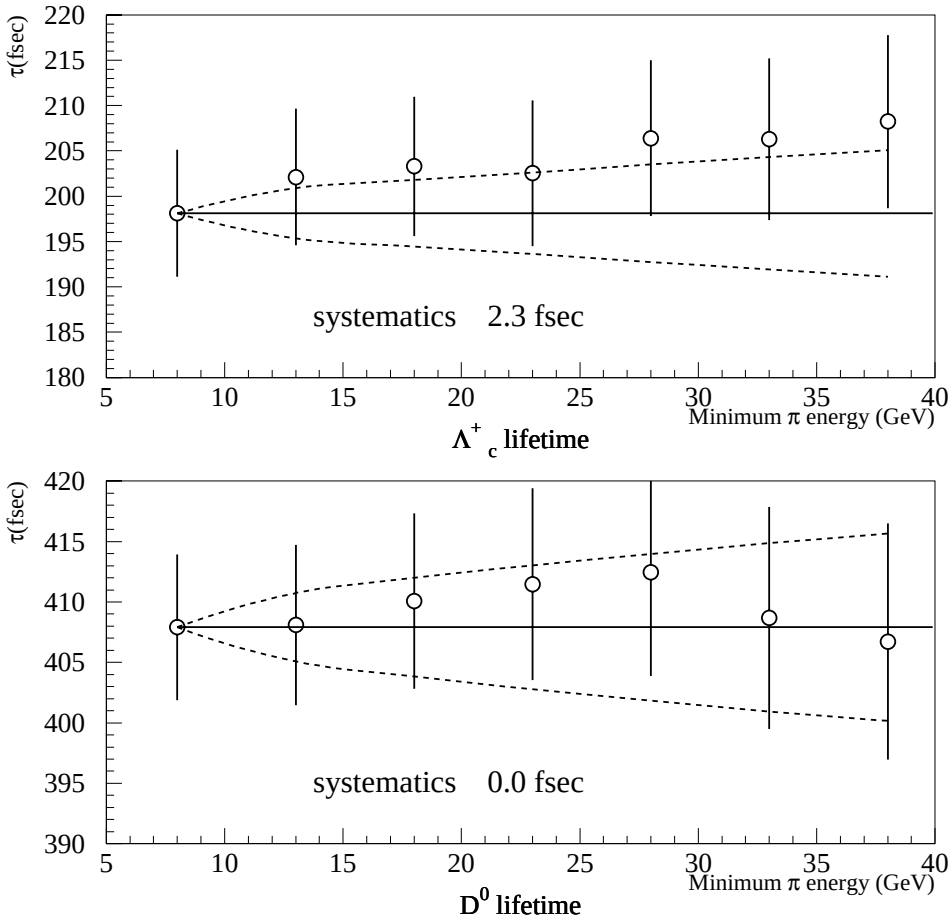

Figure 4.17: Efficiency systematics: lifetime for different minimum π energy. Curved lines show allowed fluctuations corridors calculated using Eq. 4.10. For D^0 all points are within allowed corridor and no systematics was assigned. For Λ_c^+ several points jump out of the allowed corridor. For each point that jumped out systematic error was calculated. The largest value among them was assigned as a systematic error for Λ_c^+.

1. Special "unfiltered" set of data was studied. These data was taken without online filter running. This study showed that online filter was effectively working as $L/\sigma > 3$ cut. We used $L/\sigma > 8$ cut in this analysis, which excluded region of possible acceptance uncertainty.

2. We studied lifetime as a function of L/σ cut. If short lived charm particles were biased because of the online filter, then the lifetime would not be the same for different L/σ cuts. No significant systematics was observed (Section 4.6.7).

3. A large sample of $K_s \to \pi^+\pi^-$ decays was studied (Section 4.8.2). We studied events with L close to L_{min}. There was a good agreement between predicted and observed number of K_s and no significant systematics from online filter was observed.

4.6.12 Summary of efficiency systematics

Different efficiency systematics study are summarized in Table 4.12 The total systematic error is the sum of individual systematic errors in quadrature.

Systematics	Λ_c^+	D^0
targets	-	-
2 prong vs 4-prong		3.3
high-multiplicity events	3.4	2.0
charm x_F	-	-
L/σ_L	-	1.3
sim of target losses (Δz_{tgt})	3.0	1.2
sim of large L events (L_{max})	1.2	0.9
min π energy	2.3	-
Total	**5.2**	**4.3**

Table 4.12: Summary of efficiency systematic studies. The total efficiency systematic error is the sum of individual systematic errors in quadrature.

4.6.13 Miscellaneous systematics

In previous sections we covered all important systematic errors. There were other studies which contributed very small systematic effects.

- Wrong smearing simulation $\Delta\tau < 0.2$ fs. Vertices and tracks were smeared according to the error matrices. These errors do not take into account non-gaussian effects, so the predicted smearing error and observed smearing could be different. This difference is known to be of order 5-30% (Section 3.3.3). No significant difference in the lifetime was observed when predicted errors were doubled. This effect is discussed in Section 3.1.3.

- Background fit effects $\Delta\tau < 0.3$ fs. We checked whether using a fitted background shape in a simultaneous loglikelihood fit might influence the lifetime. We fitted the background separately, then fixed the background parameters and fitted sum of signal and background. No significant difference in the lifetime was observed.

- Smoothing of efficiency: $\Delta\tau < 0.3$ fs. The efficiency function was calculated for each bin of the reduced proper time distribution. There are small fluctuations from bin to bin (Section 3.5.2). To estimate their effect we smoothed the efficiency function and calculated the lifetime. No significant difference in the lifetime was observed.

- Systematics due to definition of $t_{min} < 1.0$ fs. Finding t_{min} was a relatively complicated procedure, which involved the numerical solution of nonlinear equations (Section 3.4.4). To check for possible systematics we tried another much simpler procedure. The ensemble of rethrown events had many different proper times t. The smallest proper time t of any event in the rethrown sample that still passed the cuts was assigned to t_{min}. The lifetime for this methods of finding t_{min} were compared to the standard result. No significant difference in the lifetime was observed.

- Different fitting technique $\Delta\tau < 0.1$ fs. We tried different packages (MINFIT, PAW) to fit the lifetime (Section 3.4.6). We also compared a 6-free-parameter fit with 5-free-parameter fit plus constraint on the number of events in the sample. (Section 3.4.6). No significant difference in the lifetime was observed.

- CLEO observed [29] that the lifetime was correlated with the reconstructed mass. The correlation was due to multiple scattering effects, which are quite large at low energies. We looked for a similar effect in

our data. The signal region was split in 2 mass bins. The lifetime for each bin was measured. There was no inconsistency detected between them for either D^0 or Λ_c^+

- Other studies included lifetime variations for different run periods, fitting lifetime in different reduced proper time intervals, using proper time instead of reduced proper time, using only left or right background regions instead of two for backgound subtraction, changing the width of the signal region. In all these studies no significant systematics was observed.

We put an estimate of 1.5 fs for the total effect of miscellaneous systematic errors.

4.7 Systematics summary

Systematic studies described in this chapter are summarized in Table 4.13. The total systematic error is the sum of individual systematic errors in quadrature. Systematics is dominated by efficiency calculations.

Systematics	Λ_c^+	D^0
Mass reflections	1.3	-
Background subtraction	-	1.0
Primary vertex shift	1.1	1.0
Miscellaneous	1.5	1.5
Efficiency	5.2	4.3
Total	**5.7**	**4.7**

Table 4.13: Summary of systematics studies. The total systematics is the sum of individual systematics in quadrature.

4.8 Independent checks of the efficiency calculations

In this analysis the systematic error is dominated by efficiency calculations. We decided to do several independent checks to verify them.

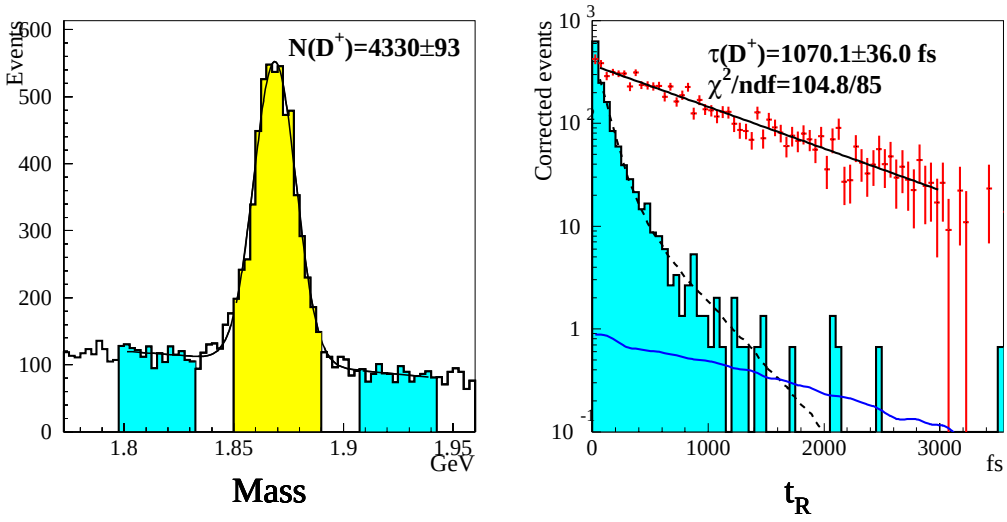

Figure 4.18: Signal and lifetime fits for D^+. On the mass plots the signal and sideband regions are shaded. The mass histogram is booked in 2.5 MeV/c^2 bins. On the lifetime plot signal events are corrected by efficiency. Dashed lines represent the lifetime fit. The background is normalized to the width of the signal region. The solid line is the efficiency as a function of the reduced time t_R. The reduced proper time histogram is booked in in 50 fs bins.

4.8.1 Measurement of the D^+ lifetime.

As an independent cross-check we decided to measure the D^+ lifetime using the same analysis technique. We used the same cuts as in Λ_c^+ and D^0 lifetime measurements. After applying those cuts we had a sample of about 4330 decays $D^+ \to K^-\pi^+\pi^+$ + charge conjugate. The measured lifetime $\tau[D^+] = 1070 \pm 36$ fs agrees with the current PDG value $\tau[D^+] = 1051 \pm 13$ fs [4] (Figure 4.18).

This was a very important cross check: first of all we measured the lifetime of another charm particle. Secondly, the measurement of the D^+ lifetime is particularly complicated in our apparatus. On average a D^+ crosses 3 targets. On the other hand, a D^0 on average crosses just one target, and a Λ_c^+ most of the time does not cross any targets at all. Targets introduce many problems in the efficiency calculations. Without target-related cuts the efficiency would have been a much simpler function. The fact that we can measure the lifetime right for the most complicated case of D^+ gives us

confidence in our efficiency calculation procedure.

4.8.2 Prediction of z-distribution for K_s.

The SELEX experiment detected large samples of strange particle decays K_s, Λ_0, $\Sigma^{\pm}$, Ξ^-, Ω^-, $\phi \cdots$. The two-million-event sample of $K_s \to \pi^+\pi^-$ that decayed in the first few centimeters after the targets was particularly valuable for the lifetime study, because these decays take place in the same region where charm particles decay. As the K_s properties are well-established, these decays provided an important reference to verify efficiency calculations.

In the lifetime analysis we calculated the efficiency as a function of reduced proper time to find the lifetime. We can use the same technique to find the efficiency as a function of the coordinate z. We calculated $\epsilon(z)$ for a large sample of $K_s \to \pi^+\pi^-$ decays, for which the lifetime is well-known. We used this result to predict the z-distribution of K_s decays and compared it with the observed distribution. The same cuts were applied to select K_s decays as in the charm analysis.

As seen in Figure 4.19 the K_s sample maps out an efficiency function. There are many similarities to the individual event efficiency for charm(Figure 3.3). Our initial plan was to use the $K_s \to \pi^+\pi^-$ sample to study the efficiency $\epsilon(z)$ and to use it in the charm lifetime analysis. In this way our efficiency would be based on data and there would be no need to use a Monte-Carlo simulation.

The problem with this approach is that K_s decays are similar to, but not exactly the same as charm decays. They have different average momenta, different opening angle. K_s are 2-prong decays, while charm decays include 2, 3 and 4-prong decays. To use the K_s efficiency for charm decays, one would have to determine how to transform a given K_s efficiency to the charm efficiency. The assumption that $\epsilon_{K_s}(z) = \epsilon_{charm}(z)$ turned out not to be precise enough. Large discrepancies were observed when the K_s data was compared with 3 or 4-prong charm decays, especially for events with large track multiplicities. One reason is that suppression of secondary interactions in the targets (Section 3.3.3) does not affect 2-prong decays, but does affect 3 and 4-prong decay. We put a lot of effort into trying to use the K_s to predict the efficiency for charm, but at the end decided to abandon this technique and develop methods based on Monte-Carlo simulation.

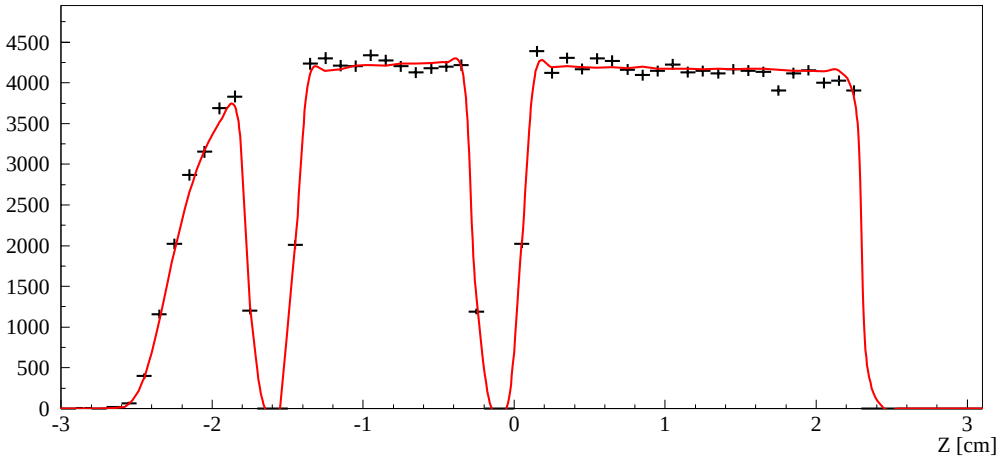

Figure 4.19: Using efficiency calculations to predict the z distribution of K_s decays produced in target 3. Crosses shows actual number of K_s decays observed. Smooth line is the prediction based on efficiency calculations. There is a good agreement between data and prediction. Once can see two downstream targets at -1.6 cm and -0.1 cm and cut $z_{sec} < 2.3$ cm on the plot. Similar studies were done for all five targets.

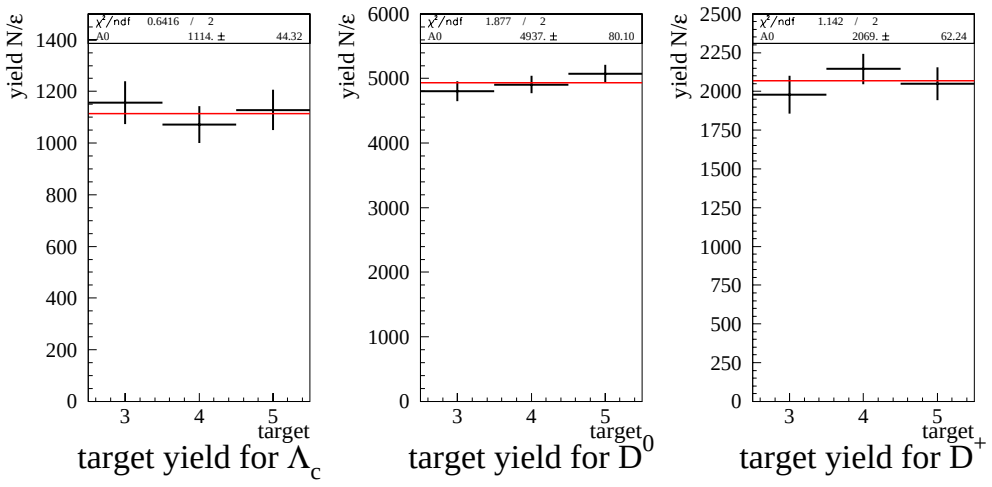

Figure 4.20: Charm yield for three carbon targets, corrected by efficiency. For each particles charm yields for different targets are consistent with each other. The corrected yields cannot be used to compare production cross-sections for Λ_c^+, D^0 and D^0, as downstream efficiency was factored out (Section 3.2.4).

4.8.3 Charm yields for identical targets.

Another study we did to test the efficiency calculations was to compare charm yields from different targets. 3 carbon target have identical parameters and one would expect the same number of charm particles to have been produced in each target. We calculated charm yields for each target, which was defined as the number of charm particles corrected by efficiency N_c/ϵ. As in the lifetime analysis we took into account only the efficiency of the vertex region, because downstream efficiency cancels out (Section 3.2.4).

The results of this study are shown in Figure 4.20. The global fit of charm yields gave $\chi^2/ndf < 1$ for Λ_c^+, D^0 and D^0. The corrected charm yields for the carbon targets were consistent with each other, and no systematics were detected.

Chapter 5

Lifetime results

Based upon 1630 Λ_c^+ and 10210 D^0 decays we observe lifetimes of $\tau[\Lambda_c^+] = 198.1 \pm 7.0 \pm 5.7$ fs and $\tau[D^0] = 407.9 \pm 6.0 \pm 4.7$ fs (Figure 5.1). These results are consistent with the present PDG averages [4]: $\tau[\Lambda_c^+] = 206 \pm 12$ fs (Figure 5.2) and $\tau[D^0] = 412.6 \pm 2.8$ fs (Figure 5.3).

In this analysis we constructed a new method to calculate the apparatus efficiency of $\epsilon(t)$. We did not need to assume a production distribution $n_0(\vec{p})$ of the events, but rather we calculated the efficiency $\epsilon(t)$ for the events $n(\vec{p})$ that we actually observed. The formalism combines lifetime measurements for different subsamples to find the efficiency correction for the overall sample. It was used to combine lifetime measurements for different decay modes or for charm particles produced in different targets.

We studied various systematics of these measurements and found them to be less than statistical errors. The systematic error in this study is dominated by efficiency calculations. As a final cross check we have applied our analysis to $D^\pm \to K^\mp \pi^\pm \pi^\pm$ where our acceptance corrections are much larger than in these analyses. Our result $\tau[D^+] = 1070 \pm 36$ fs (statistical error only) is consistent with the present PDG average [4] $\tau[D^+] = 1051 \pm 13$ fs (Figure 4.18). The precision of our $\tau[D^0]$ measurement is within a factor of 2 of the most precise measurements [85, 40, 29]. The agreement with these precise measurements demonstrates our control of systematic effects.

The overall picture of charm and beauty lifetimes shows that new precise lifetime measurements raised questions that had been previously undeveloped in theoretical calculations due to poor experimental measurements. A precision measurement of the D_s^+/D^0 lifetime ratio [28, 29] brought attention back to the issue of the strength of helicity suppression in WA/WS decays

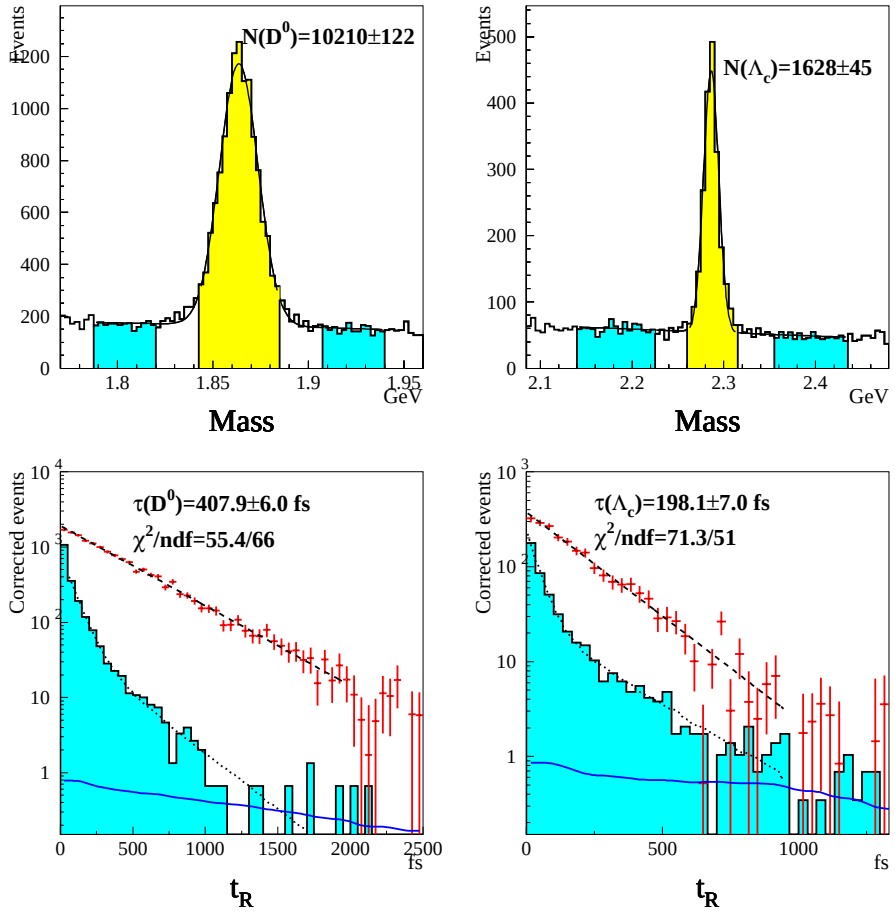

Figure 5.1: Signal and lifetime fits for Λ_c^+ and D^0. On the mass plots the signal and sideband regions are shaded. Mass histogram for Λ_c^+ is booked in 5 MeV/c^2 bins and for D^0 sample in 2.5 MeV/c^2 bins. On the lifetime plot signal events are corrected by efficiency. Dashed lines represent the lifetime fit. The background is normalized to the width of the signal region. The solid line is the efficiency as a function of reduced time t_R. Reduced proper time histogram for Λ_c^+ is booked in 33 fs bins and for D^0 in 50 fs bins.

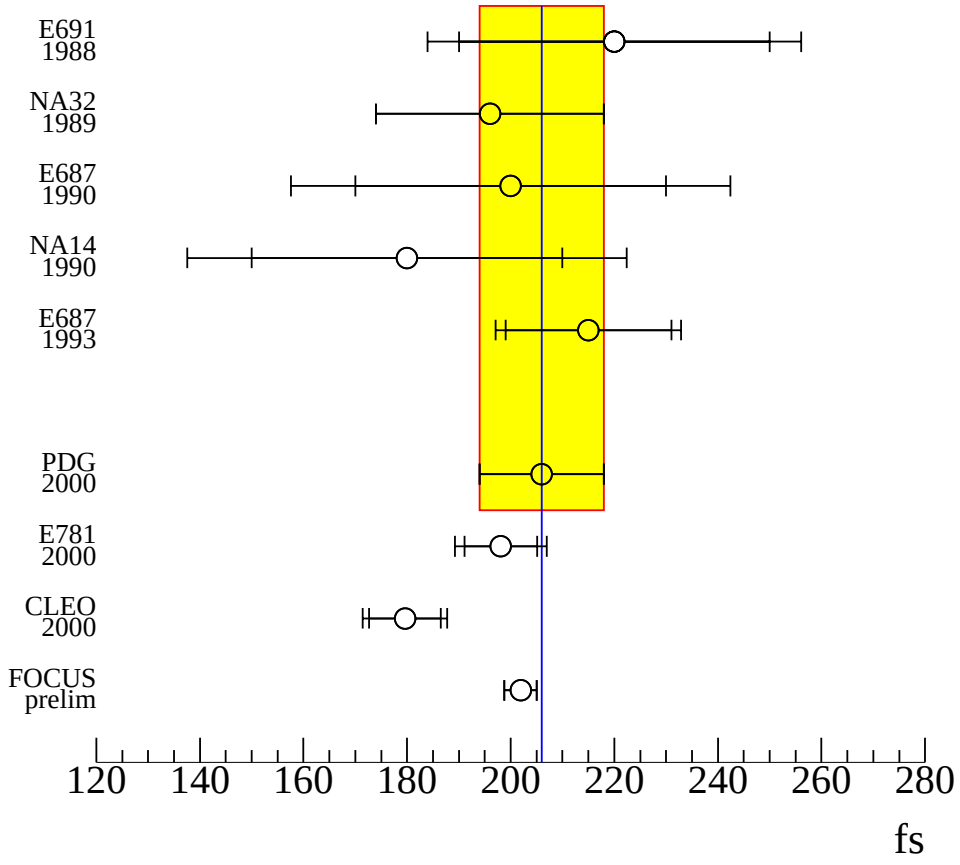

Figure 5.2: Comparison of Λ_c^+ lifetime measurements done by different experiments: E691 [78], NA32 [79], E687 [80, 38], NA14 [81]. Particle Data Group value [4] combines results of these measurements. CLEO [43] recently submitted its measurement. FOCUS result [30] is preliminary and has statistical error only. Smaller error bars show statistical error. Larger error bars show statistical and systematic errors added in quadrature. Vertical line and shaded region correspond to the PDG mean value and error.

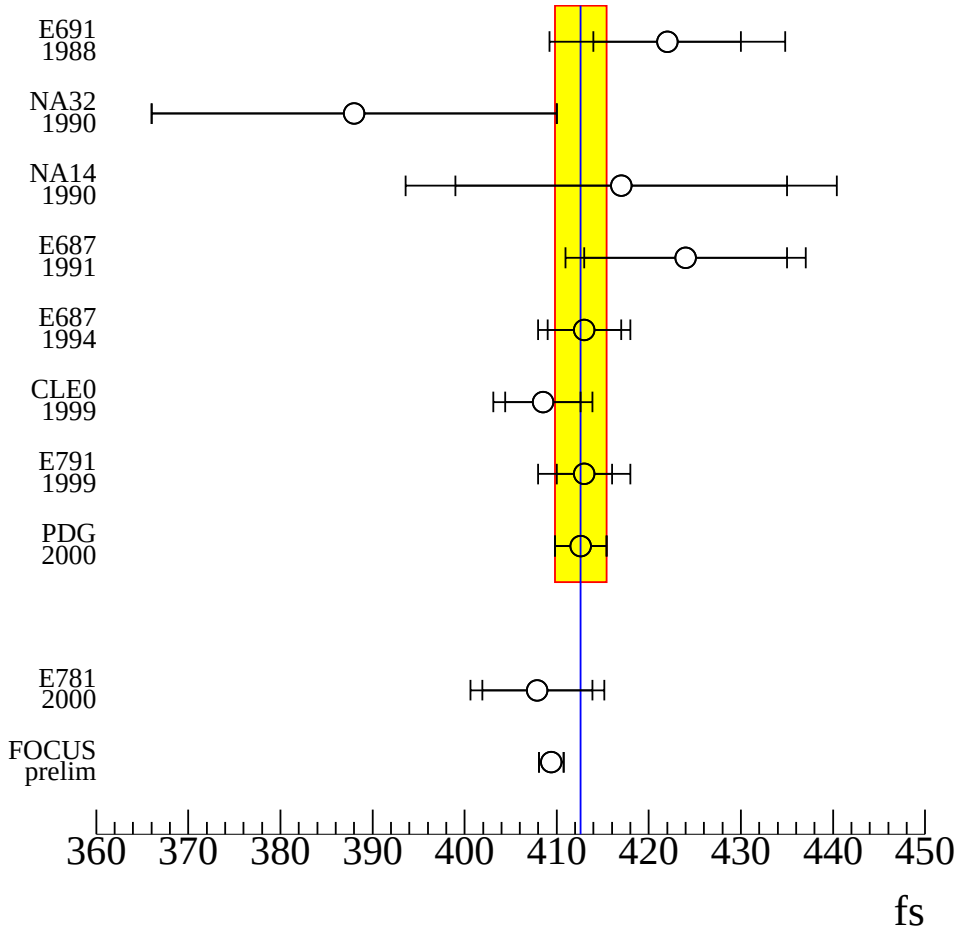

Figure 5.3: Comparison of D^0 lifetime measurements done by different experiments: E691 [82], NA32 [83], NA14 [81], E687 [84, 85], CLEO [29], E791 [40]. Particle Data Group value [4] combines results of these measurements. FOCUS result [41] is preliminary and has statistical error only. Smaller error bars show statistical error. Larger error bars show statistical and systematic errors added in quadrature. Vertical line and shaded region correspond to the PDG mean value and error.

of D-mesons. Also effects of "quark-hadron" duality are under active discussion again, which are driven by precision lifetime measurements in the beauty sector [16], as well as in the charm sector [37].

Insufficient development of the theory of charm baryon decays has been excused by poor experimental data. In this work we decrease the Λ_c^+ lifetime measurement error by a factor of 2 compared to previous best measurement [38], which is an important experimental contribution to HQE study. The last 2 years produced important new experimental results on charm lifetimes [28, 29, 40, 41, 42, 43], and more new results are expected soon [30, 31, 39]. We look forward to measurements with similar precision of the lifetimes of the other 3 stable charmed baryons, by us and others, in the near future. These precise measurements are very valuable to test and guide HQE calculations [16]. This recent experimental progress revitalized theoretical calculations and is an important step in understanding heavy quark physics.

Appendix A

The online track reconstruction in M2 spectrometer

One of the first steps in the online filter is the reconstruction of track segments in M2 PWC chambers. Track segments are pieces of tracks in M2 PWC chambers, which are outside of magnetic field and thus form straight lines. A special code was written to accomplish this task. Major requirements were speed and efficiency. One event has to be processed in about 10 ms. Efficiency requirements were about 80−90% for track segment reconstruction.

A track segment in M2 spectrometer is described by 4 parameters x_0, y_0, tx and ty - two intercepts and two slopes. Coordinates (x, y) of the track in M2 local coordinate system are given by:

$$\begin{aligned} x &= x_0 + tx \cdot z \\ y &= y_0 + ty \cdot z, \end{aligned} \tag{A.1}$$

where z is the distance from the origin of M2 spectrometer coordinate system, which is located in the middle of M2 magnet.

There is a qualitative difference between online and offline efficiency requirements. Consider a 200 GeV $\Lambda_c^+ \to pK^-\pi^+$ decay. With high probability all three secondary tracks will have momenta greater 15 GeV and will reach the M2 PWC chambers. Let's consider the effect of an 80% efficiency track reconstruction. To reconstruct a Λ_c^+ all three secondary tracks must be reconstructed. This has probability about $0.8^3 \simeq 0.51$. On the other hand to trigger the event usually only one of three tracks have to be reconstructed. That probability is approximately $1 - (0.2)^3 \simeq 0.99$. So one can trade effi-

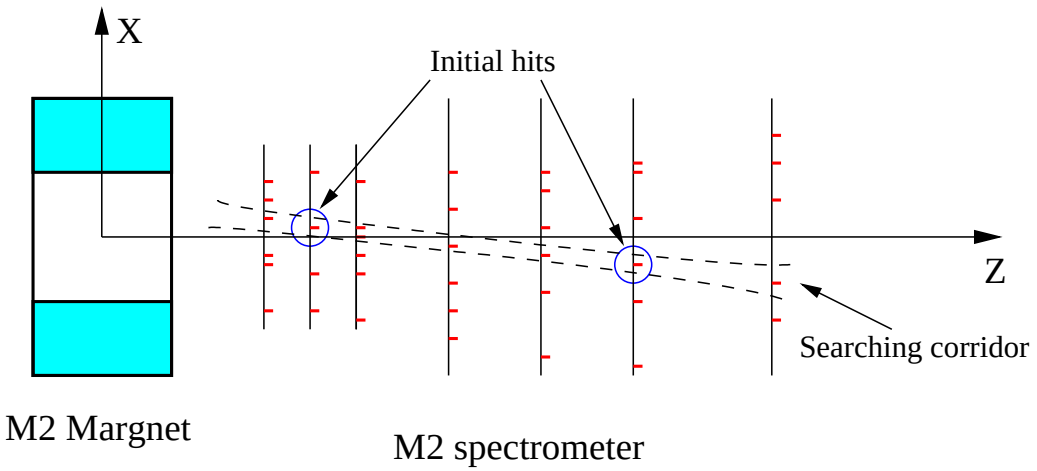

Figure A.1: Illustration of track finding algorithm

ciency for speed in the online filter to trigger interesting events. In offline code the situation is reversed: usually slower, but more efficient code is used.

To find track segments in the M2 spectrometer the following strategy was used. Four initial hits were selected in 4 different planes. They uniquely define a track segment which passes through all 4 initial hits. After that a searching corridor was built around this predicted track segment. If there were enough hits along the corridor then we formed a track segment. There were also other requirements imposed on the track segment discussed later. Hits that formed the track segment were marked as associated with this track segment.

To reconstruct a track segment every plane in the starting set of four must have a hit. M2 PWC chambers have about 95% hit efficiency (Section 2.2.7), so the probability of having all 4 hits in the initial planes is $0.95^4 \simeq 0.81$. To increase the efficiency of the code different sets of initial planes were tried, and the search algorithm was run several times. Each choice of initial planes was defined as a search combination. Each combination had different choices of initial planes and different sets of cuts. We usually started with combination with tight cuts, to find high quality track segments with a large number of hits and small χ^2. After that combinations with looser and looser cuts were tried.

The size of the search corridor was calculated based on the error matrix given by 4 initial hits. The minimum size of the window was fixed at twice

the wire spacing. All hits on the 4 starting planes were tried as initial hits. If a plane had hits in adjacent wires, then neither of those hits was used as an initial hit, because of the large position uncertainty. This uncertainty usually was resolved when we used different initial planes and the algorithm selected one of the two adjacent hits to lie on the track.

A.1 Improvements of the speed of the code

To illustrate speed issues let's consider the following simplified example. Imagine that there are 10 tracks in the M2 spectrometer. Then each plane would have 10 hits. There are 14 M2 PWC planes, so there are 140 hits in total. After 4 initial planes are selected there are 10^4 possible initial hits combinations. There are 10^4 searching corridors constructed, and all hits in non-initial planes should be tried if they are inside the searching corridor. Then the number of times the distance between the track and a hit is calculated is about 10^5. So carrying all the combinations to the end is proportional to n_{hit}^5, where n_{hit} is the number of hits in the planes.

Out of these 10^4 initial tries, only 10 will correspond to real tracks, and the rest 9990 will be just random combinations of hits. From this example it is quite clear that code has to quickly reject wrong choices of initial hits, because carrying complete calculations for all 10^4 initial tries is very expensive in time.

A.1.1 Evaluation of the searching corridor

Now let us discuss how we speed up the code by quickly accepting or rejecting searching corridors.

There were 8 cuts (x_l, x_h, tx_l, tx_h, y_l, y_h, ty_l, ty_h) that specified limits on reconstructed track segment parameters:

$$\begin{aligned} x_l < x_0 < x_h \\ tx_l < tx < tx_h \\ y_l < y_0 < y_h \\ ty_l < ty < ty_h \end{aligned} \tag{A.2}$$

Parameters of the track segment were calculated based on 4 initial hits. If slopes or intercepts were outside the bounds we did not use this search corridor. Values of cuts were defined by the size of the magnet aperture and maximum angle that track could reach if it passes through the magnet.

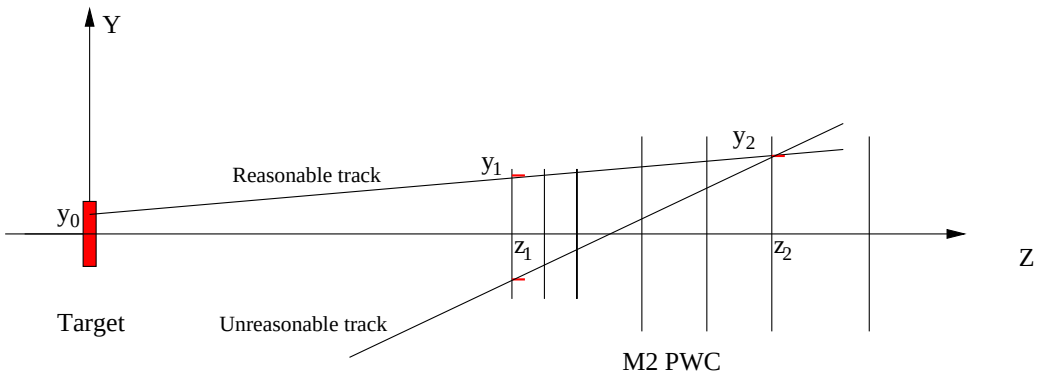

Figure A.2: Illustration of evaluating of the initial hits in y-view. Track has to point back to the targets

Most of the tracks come from the charm targets, and only few from hyperon decays do not point back to charm targets. Secondary tracks from charm decay also originate very close to the targets.

The cut y_{tgt} was used to select the tracks that come from the charm targets in y-view. In this view tracks are not bent by the magnets and they point back to the charm targets (Figure A.2). Two initial hits were chosen in two initial y-planes. Using these coordinates the track slope and intercept were calculated in y view:

$$\begin{aligned} ty &= \frac{y_2 - y_1}{z_2 - z_1} \\ y_0 &= y_2 - ty \cdot z_2 \end{aligned} \tag{A.3}$$

If $|y_0| < y_{tgt}$ the pair of two initial hits was accepted. Otherwise it was rejected and next pair was tried. So decision about track segment corridor in y view was done using information only from 2 planes. These quick calculations greatly reduced the number of track corridors that were tried.

Cuts p_x^{max} and p^{min} were used to select tracks that come from the charm target in the x-view. Unlike the y-view, where tracks point back to the target, in the x-view tracks are bent. Two initial hits were chosen in two initial x-planes. The primary vertex was found by extrapolating the beam track in the target, where interaction had happen. This 3 points were used to calculate track momenta p and its p_x with respect to beam track (Figure A.3).

There were two magnets before the M2 spectrometer. In the small angle approximation two magnets are equivalent to one effective magnet with p_t-

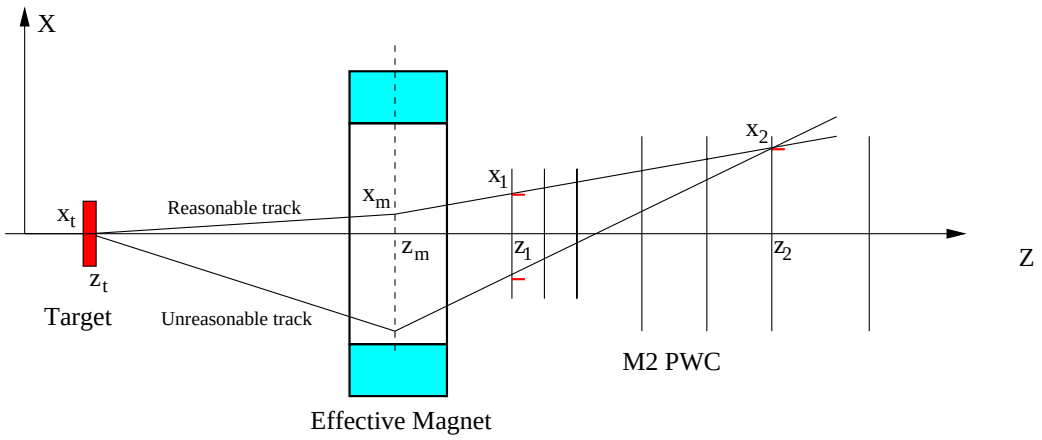

Figure A.3: Illustration of evaluating of the initial hits in x-view. Track has to have a large momentum and small p_x.

kick and position given by:

$$\begin{aligned} p_t &= p_{t1} + p_{t2} \\ z_m &= \frac{p_{t1} \cdot z_1 + p_{t2} \cdot z_2}{z_1 + z_2}, \end{aligned} \tag{A.4}$$

where p_{t1}, p_{t2} are the p_t-kicks of the two magnets, and z_1, z_2 their positions.

Then using 3 points along the track and position of the effective magnet we can evaluate track momentum p and transverse momentum p_x:

$$\begin{aligned} tx_2 &= \frac{x_2 - x_1}{z_2 - z_1} \\ x_m &= x_2 - tx_2 \\ tx_1 &= \frac{x_m - x_t}{z_m - z_t} \\ p &= \frac{p_t}{tx_2 - tx_1} \\ p_x &= p \cdot tx_1 \end{aligned} \tag{A.5}$$

If the momentum of the track was big enough ($|p| > p^{min}$) and transverse momentum was small enough ($|p_x| < p_x^{max}$) we proceeded with that set of initial hits. If not this combination of initial hits was rejected. Again, rather quick calculations based on the choice of only 2 initial hits in x-view were

done to reject or accept a searching corridor. Using these cuts in the x-view gave a factor of 4 of in speed and allowed us to solve the problem of high-multiplicity events (Section 2.4.1).

A.1.2 Other speed improvements

Once a track segment was reconstructed the hits associated with it were marked. For the sake of speed marked hits were taken out of the list of all hits in M2 chambers. When next segment was searched marked hits were not used. This increases the speed of the code significantly, and also eliminates the problem of finding the same track segment more than one time. On the other hand it introduces inefficiency in the code, because one hit can be associated with two tracks. This problem is particularly important in y-view, where tracks are not bent by the magnetic field, and hits are about 3 times closer than they are in x-view.

To speed up the code we counted the total number of hits in the M2 PWC chambers. If the number was greater than n_{hit}, combination did not start, because it would take to much time to complete it.

A.2 Track quality evaluation

After a track segment was found the reduced χ^2_r and number of planes where the hits were detected n_{pl} were used to evaluate its quality. The reduced χ^2_r was calculated using:

$$\chi^2_r = \frac{1}{n_{pl} - 4} \sum_i^{n_{pl}} \frac{(x_i - \overline{x})^2}{\sigma_i^2}, \tag{A.6}$$

where n_{pl} is the number of planes where hits where detected, x_i is the measured hit coordinate in i-th plane, $\overline{x}$ is the predicted coordinate, σ_i is the error of the measurement. Only tracks with momenta greater than 15 GeV could reach the M2 planes. We ignored effects of multiple scattering in M2 chambers. They were small compared to distance between wires d. Measurement errors were calculated using $\sigma = d/\sqrt{12}$. The efficiency of chambers was greater than 95 %, so we set n_{pl} close to 14 (total number of planes).

Fake tracks can be created if the x-projection of one track is combined with the y-projection of another track. This ambiguity can be resolved using

u and v planes. We required track segments to have several u, v hits to be accepted.

A.3 Online searching combinations

We used several search combinations to find track segments. They had different sets of cuts. Generally we started with tight cuts to find high quality tracks. After some tracks had been found and hits marked out, the hit list was shorten. That simplified the problem. In next combinations we loosened cuts and even dropped some cuts to increase efficiency.

No.	tx [a] [mrad]	ty [a] [mrad]	y_{tgt} [cm]	χ^2_r	n_{pl}	n_{hit}	p^{min} [GeV]	p_x^{max} [GeV]
1-2 [b]	90	23	1.0	2.3	13	-	30.	1.0
3-5 [c]	90	23	1.0	2.3	11	210	-	-
6	-	-	-	2.3	11	150	-	-
7	-	-	-	3.0	11	150	-	-
8	-	-	-	3.0	8	150	-	-
9	-	30	1.0	2.5	7	150	-	-

Table A.1: Online searching combinations. When the cut was not used we indicated it with sign "-" in the table.
[a] Values of cuts were $tx_l = -tx$ and $tx_h = +tx$.
[b] We run this combination two times with different initial planes.
[c] We run this combination three times with different initial planes.

Bibliography

[1] N. Cabibbo and L. Maiani, "The lifetime of charmed particles," *Phys. Lett.* **B79** (1978) 109.

[2] W. J. Marciano and A. Sirlin, "Electroweak radiative corrections to τ decay," *Phys. Rev. Lett.* **61** (1988) 1815–1818.

[3] N. Cabibbo and L. Maiani, "Two body decays of charmed mesons," *Phys. Lett.* **B73** (1978) 418.

[4] D. E. Groom *et al.*, "Review of particle physics," *Eur. Phys. J.* **C15** (2000) 1.

[5] L. B. Okun, *Leptons and Quarks*. Amsterdam, Netherlands: North-holland 361p, 1982.

[6] B. Guberina, S. Nussinov, R. D. Peccei, and R. Ruckl, "D-meson lifetimes and decays," *Phys. Lett.* **B89** (1979) 111.

[7] G. Bellini, I. Bigi, and P. J. Dornan, "Lifetimes of charm and beauty hadrons," *Phys. Rept.* **289** (1997) 1.

[8] I. Bigi, M. Shifman, and N. Uraltsev, "Aspects of heavy quark theory," *Ann. Rev. Nucl. Part. Sci.* **47** (1997) 591–661, `hep-ph/9703290`.

[9] N. Uraltsev, "Heavy-quark expansion in beauty and its decays," `hep-ph/9804275`.

[10] B. Blok and M. Shifman, "Lifetimes of charmed hadrons revisited. Facts and fancy," `hep-ph/9311331`. Talk given at 3rd Workshop on the Tau-Charm Factory, Marbella, Spain, 1-6 Jun 1993.

[11] I. I. Bigi, M. A. Shifman, N. G. Uraltsev, and A. I. Vainshtein, "On the motion of heavy quarks inside hadrons: Universal distributions and inclusive decays," *Int. J. Mod. Phys.* **A9** (1994) 2467–2504, hep-ph/9312359.

[12] I. Bigi, M. Shifman, N. G. Uraltsev, and A. Vainshtein, "Sum rules for heavy flavor transitions in the SV limit," *Phys. Rev.* **D52** (1995) 196–235, hep-ph/9405410.

[13] I. I. Bigi, N. G. Uraltsev, and A. I. Vainshtein, "Nonperturbative corrections to inclusive beauty and charm decays: QCD versus phenomenological models," *Phys. Lett.* **B293** (1992) 430–436, hep-ph/9207214.

[14] M. E. Luke, "Effects of subleading operators in the heavy quark effective theory," *Phys. Lett.* **B252** (1990) 447–455.

[15] J. Chay, H. Georgi, and B. Grinstein, "Lepton energy distributions in heavy meson decays from QCD," *Phys. Lett.* **B247** (1990) 399–405.

[16] I. I. Bigi, "The lifetimes of heavy flavour hadrons: A case study in quark hadron duality,".

[17] M. Shifman, "Quark-hadron duality," hep-ph/0009131.

[18] E. C. Poggio, H. R. Quinn, and S. Weinberg, "Smearing the quark model," *Phys. Rev.* **D13** (1976) 1958.

[19] G. Altarelli, G. Martinelli, S. Petrarca, and F. Rapuano, "Failure of local duality in inclusive non-leptonic heavy flavour decays," *Phys. Lett.* **B382** (1996) 409–414, hep-ph/9604202.

[20] B. Grinstein and R. F. Lebed, "Explicit quark-hadron duality in heavy-light meson weak decays in the 't Hooft model," *Phys. Rev.* **D57** (1998) 1366, hep-ph/9708396.

[21] I. Bigi and N. Uraltsev, "Pauli interference in the 't Hooft model: Heavy quark expansion and quark-hadron duality," *Phys. Lett.* **B457** (1999) 163, hep-ph/9903258.

[22] I. I. Bigi and N. G. Uraltsev, "Gluonic enhancements in non-spectator beauty decays: An Inclusive mirage though an exclusive possibility," *Phys. Lett.* **B280** (1992) 271–280.

[23] H.-Y. Cheng and K.-C. Yang, "Phenomenological analysis of D-meson lifetimes," *Phys. Rev.* **D61** (2000) 014008, `hep-ph/9905313`.

[24] **CLEO** Collaboration, M. Chadha *et al.*, "Improved measurement of the pseudoscalar decay constant f_{D_s}," *Phys. Rev.* **D58** (1998) 032002, `hep-ex/9712014`.

[25] I. I. Bigi and N. G. Uraltsev, "D_s Lifetime, m_b, m_c and $|V_{cb}|$ in the Heavy Quark Expansion," *Z. Phys.* **C62** (1994) 623–632, `hep-ph/9311243`.

[26] I. I. Bigi and N. G. Uraltsev, "Weak annihilation and the endpoint spectrum in semileptonic B decays," *Nucl. Phys.* **B423** (1994) 33–55, `hep-ph/9310285`.

[27] C. Caso *et al.*, "Review of particle physics," *Eur. Phys. J.* **C3** (1998) 1–794.

[28] **E791** Collaboration, E. M. Aitala *et al.*, "Measurement of the D_s lifetime," *Phys. Lett.* **B445** (1999) 449–454, `hep-ex/9811016`.

[29] **CLEO** Collaboration, G. Bonvicini *et al.*, "Measurement of charm meson lifetimes," *Phys. Rev. Lett.* **82** (1999) 4586–4590, `hep-ex/9902011`.

[30] H. W. K. Cheung, "Review of charm lifetimes," `hep-ex/9912021`.

[31] **SELEX** Collaboration, J. Russ *et al.*, "Recent results from SELEX," `hep-ex/0010011`. Talk given at 30th International Conference on High-Energy Physics (ICHEP 2000), Osaka, Japan, 27 Jul - 2 Aug 2000.

[32] B. Guberina, R. Ruckl, and J. Trampetic, "Charmed baryon lifetime differences," *Z. Phys.* **C33** (1986) 297.

[33] I. Bigi, B. Blok, M. Shifman, N. Uraltsev, and A. Vainshtein, "Nonleptonic decays of beauty hadrons: From phenomenology to

theory," hep-ph/9401298. Ed. S. Stone: 'B decays', revised 2nd edition.

[34] N. G. Uraltsev, "On the problem of boosting nonleptonic b baryon decays," *Phys. Lett.* **B376** (1996) 303–308, hep-ph/9602324.

[35] P. Colangelo, C. A. Dominguez, and G. Nardulli, "Violations of local duality in the heavy quark sector," *Phys. Lett.* **B409** (1997) 417–424, hep-ph/9705390.

[36] M. B. Voloshin, "Relations between inclusive decay rates of heavy baryons," *Phys. Rept.* **320** (1999) 275, hep-ph/9901445.

[37] I. I. Bigi and N. G. Uraltsev, "$D^0 - \overline{D^0}$ oscillations as a probe of quark-hadron duality," hep-ph/0005089.

[38] **E687** Collaboration, P. L. Frabetti *et al.*, "A Measurement of the Λ_c^+ lifetime," *Phys. Rev. Lett.* **70** (1993) 1755–1758.

[39] E. Ramires *et al.*, "A high statistics measurement of Ξ_c lifetimes,". Talk given at the meeting of the Division of Particles and Fields of the American Physical Society (DPF 2000), Columbus, Ohio, USA, August 9-12, 2000.

[40] **E791** Collaboration, E. M. Aitala *et al.*, "Measurements of lifetimes and a limit on the lifetime difference in the neutral D-meson system," *Phys. Rev. Lett.* **83** (1999) 32, hep-ex/9903012.

[41] **FOCUS** Collaboration, J. M. Link *et al.*, "A measurement of lifetime differences in the neutral D-meson system," *Phys. Lett.* **B485** (2000) 62–70, hep-ex/0004034.

[42] **SELEX** Collaboration, A. Kushnirenko *et al.*, "Precision measurements of the Λ_c^+ and D^0 lifetimes," hep-ex/0010014.

[43] **CLEO** Collaboration, A. H. Mahmood *et al.*, "Measurement of the Λ_c^+ lifetime," hep-ex/0011049.

[44] F. Garcia, *Hadroproducao do Barion Charmoso Λ_c no Experimento SELEX-E781*. PhD thesis, University of Sao Paulo, Sao Paulo, Brazil, 2000.

[45] **E791** Collaboration, E. M. Aitala *et al.*, "Multidimensional resonance analysis of $\Lambda_c^+ \to pK^-\pi^+$," *Phys. Lett.* **B471** (2000) 449–459, hep-ex/9912003.

[46] **SELEX** Collaboration, S. Y. Jun *et al.*, "Observation of the Cabibbo suppressed decay $\Xi_c^+ \to pK^-\pi^+$," *Phys. Rev. Lett.* **84** (2000) 1857–1861, hep-ex/9907062.

[47] **FOCUS** Collaboration, J. M. Link *et al.*, "Measurements of the Σ_c^0 and Σ_c^{++} mass splittings," *Phys. Lett.* **B488** (2000) 218–224, hep-ex/0005011.

[48] **FOCUS** Collaboration, F. Fabri, "Results on charmed meson spectroscopy from FOCUS,". Talk given at 30th International Conference on High-Energy Physics (ICHEP 2000), Osaka, Japan, 27 Jul - 2 Aug 2000.

[49] **CLEO** Collaboration, C. P. Jessop *et al.*, "Observation of two narrow states decaying into $\Xi_c^+\gamma$ and $\Xi_c^0\gamma$," *Phys. Rev. Lett.* **82** (1999) 492–496, hep-ex/9810036.

[50] **SELEX** Collaboration, U. Dersch *et al.*, "Total cross section measurements with π^-, Σ^- and protons on nuclei and nucleons around 600 GeV/c," *Nucl. Phys.* **B579** (2000) 277, hep-ex/9910052.

[51] S. F. Biagi *et al.*, "Measurements of the total cross-sections of Σ^- and Ξ^- on protons and deuterons between 74 Gev/c and 137 Gev/c," *Nucl. Phys.* **B186** (1981) 1.

[52] I. Eschrich, *Measurement of the Σ^- charge radius at the Fermilab hyperon beam.* PhD thesis, Max-Planck-Institut fur Kernphysik, 1998.

[53] K. Vorwalter, *Determination of the Pion Charge Radius with a Silicon Microstrip Detector System.* PhD thesis, Max-Planck-Institut fur Kernphysik, 1998.

[54] H. Krueger, *Untersuchung der elastischen Hadron-Elektron-Streuung bei* 540 GeV/c *zur Messung des elektromagnetischen Ladungsradius des Protons.* PhD thesis, Max-Planck-Institut fur Kernphysik, 1999.

[55] G. Bunce *et al.*, "Λ^0 hyperon polarization in inclusive production by 300 GeV protons on beryllium," *Phys. Rev. Lett.* **36** (1976) 1113–1116.

[56] J. Soffer, "Is the riddle of the hyperon polarizations solved?," `hep-ph/9911373`. Invited talk at Hyperon 99: Hyperon Physics Symposium, Batavia, Illinois, 27-29 Sep 1999.

[57] P. Pogodin, *Polarization of* Σ^+ *hyperons produced by* 800 GeV/c *protons on copper and beryllium*. PhD thesis, University of Iowa, 1999.

[58] K. Nelson, *Polarization of* Λ^0 *inclusively produced by a* 610 GeV/c Σ^- *beam*. PhD thesis, University of Iowa, 1999.

[59] J. L. Langland, *Hyperon and anti-hyperon production in p-Cu interactions*. PhD thesis, University of Iowa, 1996. UMI-96-03058.

[60] J. Langland, "Hyperon beam flux parameterization for E781 based on E497 data," H-Note 693, SELEX Internal Report, 1994.

[61] P. Mathew, *Construction and evaluation of a high resolution silicon microstrip tracking detector and utilization to determine interaction vertices*. PhD thesis, Dept. of Physics, Carnegie Mellon University, 1997.

[62] N. Bondar *et al.*, "E781 beam transition radiation detector," H-Note 746, SELEX Internal Report, 1995.

[63] **SELEX** Collaboration, A. Atamantchuk *et al.*, "Design and performance of the Fermilab E781 (SELEX) hardware scattering trigger," *Nucl. Instrum. Meth.* **A425** (1999) 529–535.

[64] P. Pogodin *et al.*, "Drift chambers of the M1 spectrometer: the detector, electronics and software," H-Note 788, SELEX Internal Report, 1997.

[65] U. Dersch *et al.*, "Mechanical design of the large angle silicon detectors," H-Note 804, SELEX Internal Report, 1998.

[66] M. K. A. Antonov, G. Dsyubenko, "Geometry of the assembled E781 Photon 1, 2 detectors," H-Note 748, SELEX Internal Report, 1995.

[67] V. V. G. Davidenko, M. Kubantsev, "Photon database for E781," H-Note 767, SELEX Internal Report, 1996.

[68] V.Maleev *et al.*, "Description and test results for DPWC and TRD in E781," H-Note 747, SELEX Internal Report, 1995.

[69] **SELEX** Collaboration, J. Engelfried *et al.*, "The E781 (SELEX) RICH detector," *Nucl. Instrum. Meth.* **A409** (1998) 439.

[70] L. E. T. Lungov, "Vector drift chambers database," H-Note 779, SELEX Internal Report, 1997.

[71] **E687** Collaboration, P. L. Frabetti *et al.*, "Description and performance of the Fermilab E687 spectrometer," *Nucl. Instrum. Meth.* **A320** (1992) 519–547.

[72] **E791** Collaboration, E. M. Aitala *et al.*, "Correlations between D and $\overline{D}$ mesons produced in 500 GeV/c π^--nucleon interactions," *Eur. Phys. J. direct* **C4** (1999) 1–67, `hep-ex/9809029`.

[73] A. Kulyatsev *et al.*, "E781 hardware trigger preliminary design," H-Note 676, SELEX Internal Report, 1994.

[74] D. M. J. Engelfried, P. Cooper, "The E781 trigger and DAQ System," H-Note 643, SELEX Internal Report, 1995.

[75] **SELEX** Collaboration, J. Russ *et al.*, "Radiative width of the a2 meson," `hep-ex/9901014`. Presented at 29th International Conference on High-Energy Physics (ICHEP 98), Vancouver, Canada, 23-29 Jul 1998.

[76] U. Dersch, *Messung totaler Wirkungsquerschnitte mit* Σ^-, p, π^- *und* π^+ *bei* 600 GeV/c *Laborimplus*. PhD thesis, Max-Planck-Institut fur Kernphysik, 1998.

[77] F. James and M. Roos, "'MINUIT' a system for function minimization and analysis of the parameter errors and correlations," *Comput. Phys. Commun.* **10** (1975) 343.

[78] **E691** Collaboration, J. C. Anjos *et al.*, "Measurement of the Λ_c^+ lifetime," *Phys. Rev. Lett.* **60** (1988) 1379.

[79] **ACCMOR** Collaboration, S. Barlag *et al.*, "Precise determination of the lifetime of the charmed baryon Λ_c," *Phys. Lett.* **B218** (1989) 374.

[80] P. L. Frabetti *et al.*, "Measurement of the Λ_c^+ and D_s^+ lifetimes," *Phys. Lett.* **B251** (1990) 639–644.

[81] **NA14/2** Collaboration, M. P. Alvarez *et al.*, "Lifetime measurements of the D^+, D^0, D_s^+ and Λ_c^+ charmed particles," *Z. Phys.* **C47** (1990) 539–546.

[82] **E691** Collaboration, J. R. Raab *et al.*, "Measurement of the D^0, D^+ and D_s^+ lifetimes," *Phys. Rev.* **D37** (1988) 2391.

[83] **ACCMOR** Collaboration, S. Barlag *et al.*, "Measurement of the masses and lifetimes of the charmed mesons D^0, D^+ and D_s^+," *Z. Phys.* **C46** (1990) 563–568.

[84] **E687** Collaboration, P. L. Frabetti *et al.*, "A Measurement of the D^0 and D^+ lifetimes," *Phys. Lett.* **B263** (1991) 584–590.

[85] **E687** Collaboration, P. L. Frabetti *et al.*, "Precise measurements of the D^0 and D^+ meson lifetimes," *Phys. Lett.* **B323** (1994) 459–466.